Interface Aspects in All-Solid-State Li-Based Batteries Reviewed

Chunguang Chen,* Ming Jiang, Tao Zhou, Luc Raijmakers, Egor Vezhlev, Baolin Wu, Tobias U. Schülli, Dmitri L. Danilov, Yujie Wei,* Rüdiger-A. Eichel, and Peter H. L. Notten*

Extensive efforts have been made to improve the Li-ionic conductivity of solid electrolytes (SE) for developing promising all-solid-state Li-based batteries (ASSB). Recent studies suggest that minimizing the existing interface problems is even more important than maximizing the conductivity of SE. Interfaces are essential in ASSB, and their properties significantly influence the battery performance. Interface problems, arising from both physical and (electro)chemical material properties, can significantly inhibit the transport of electrons and Li-ions in ASSB. Consequently, interface problems may result in interlayer formation, high impedances, immobilization of moveable Li-ions, loss of active host sites available to accommodate Li-ions, and Li-dendrite formation, all causing significant storage capacity losses and ultimately battery failures. The characteristic differences of interfaces between liquid- and solid-type Li-based batteries are presented here. Interface types, interlayer origin, physical and chemical structures, properties, time evolution, complex interrelations between various factors, and promising interfacial tailoring approaches are reviewed. Furthermore, recent advances in the interface-sensitive or depth-resolved analytical tools that can provide mechanistic insights into the interlayer formation and strategies to tailor the interlayer formation, composition, and properties are discussed.

1. Introduction

Li-based batteries (LBB), including lithium batteries and Li-ion batteries, are powering most of our modern portable electronic devices and (hybrid) electric vehicles ((H)EV). Almost all LBB are currently using liquid electrolytes (LE), which raises serious safety concerns due to the flammable organic liquids and the potential to leak out.[1–3] Due to these concerns, all-solid-state Li-based batteries (ASSB), containing nonflammable solid electrolytes (SE), are receiving increasing interest from science and industry.

Essentially, ASSB can be divided into two groups: bulk-type ASSB and thin-film ASSB, each having their own advantages and applications. Bulk-type ASSB use active material powders by compressing them into pellets and stacks or by fabricating slurries and tape casting them as films. Due to the high energy density, safety, and low fabrication cost, bulk-type ASSB are considered highly attractive for

Dr. C. Chen, M. Jiang, Dr. L. Raijmakers, B. Wu, Dr. D. L. Danilov,
Prof. R.-A. Eichel, Prof. P. H. L. Notten
Forschungszentrum Jülich (IEK-9)
D-52425, Jülich Germany
E-mail: c.chen@fz-juelich.de; p.h.l.notten@tue.nl
M. Jiang, Dr. D. L. Danilov, Prof. P. H. L. Notten
Eindhoven University of Technology
P.O. Box 513, Eindhoven 5600 MB, The Netherlands
Dr. T. Zhou
Nanoscience and Technology Division
Argonne National Laboratory
Lemont, IL 60439, USA
Dr. E. Vezhlev
Jülich Centre for Neutron Science (JCNS-4)
Forschungszentrum Jülich
85748, Garching Germany

B. Wu, Prof. R.-A. Eichel
Institute of Physical Chemistry
RWTH Aachen University
D-52074, Aachen Germany
Dr. T. U. Schülli
ID01 ESRF
CS 40220, Grenoble Cedex 9, Grenoble F-38043, France
Prof. Y. Wei
LNM
Institute of Mechanics
Chinese Academy of Sciences
Beijing 100190, China
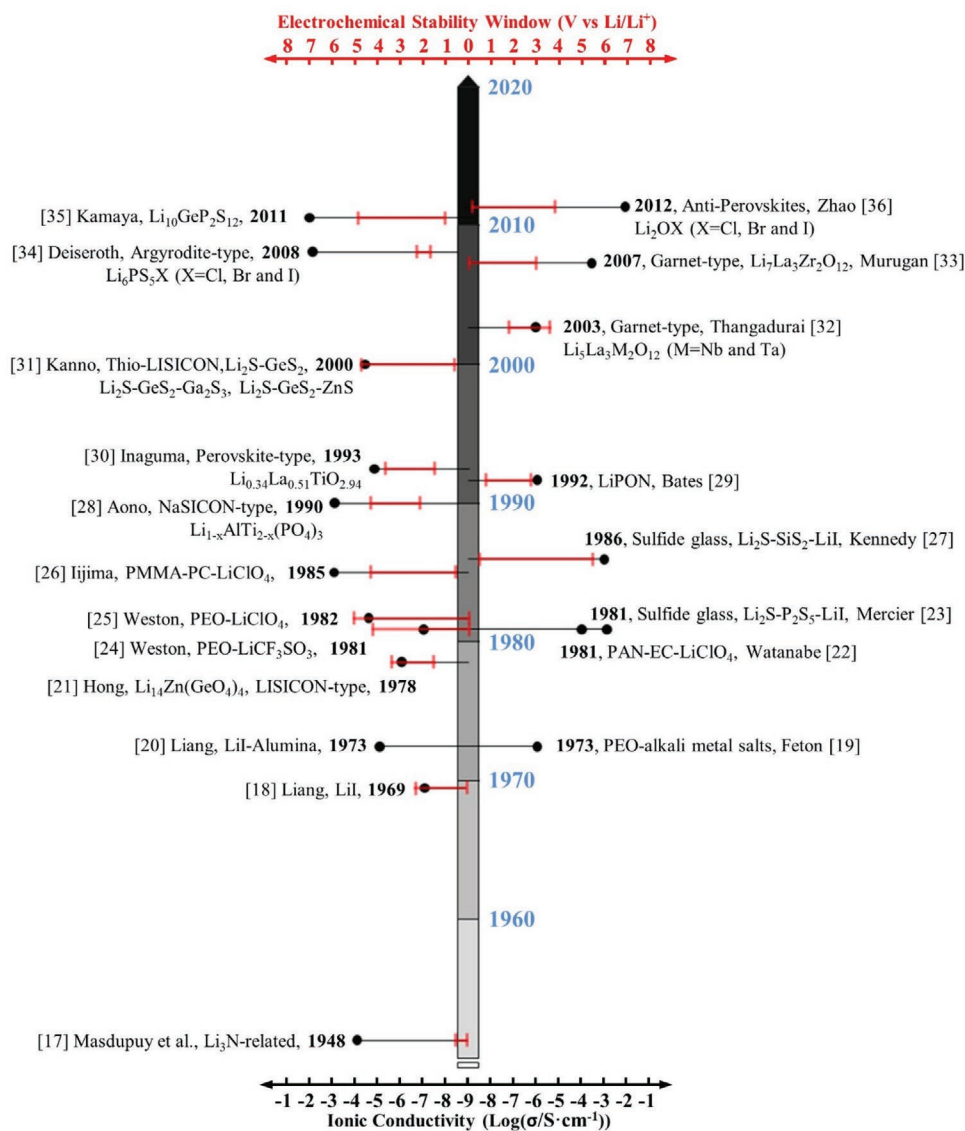E-mail: yujie_wei@lnm.imech.ac.cn
Prof. Y. Wei
School of Engineering Sciences
University of Chinese Academy of Sciences
Beijing 100049, China
Prof. P. H. L. Notten
Centre for Clean Energy Technology
University of Technology Sydney
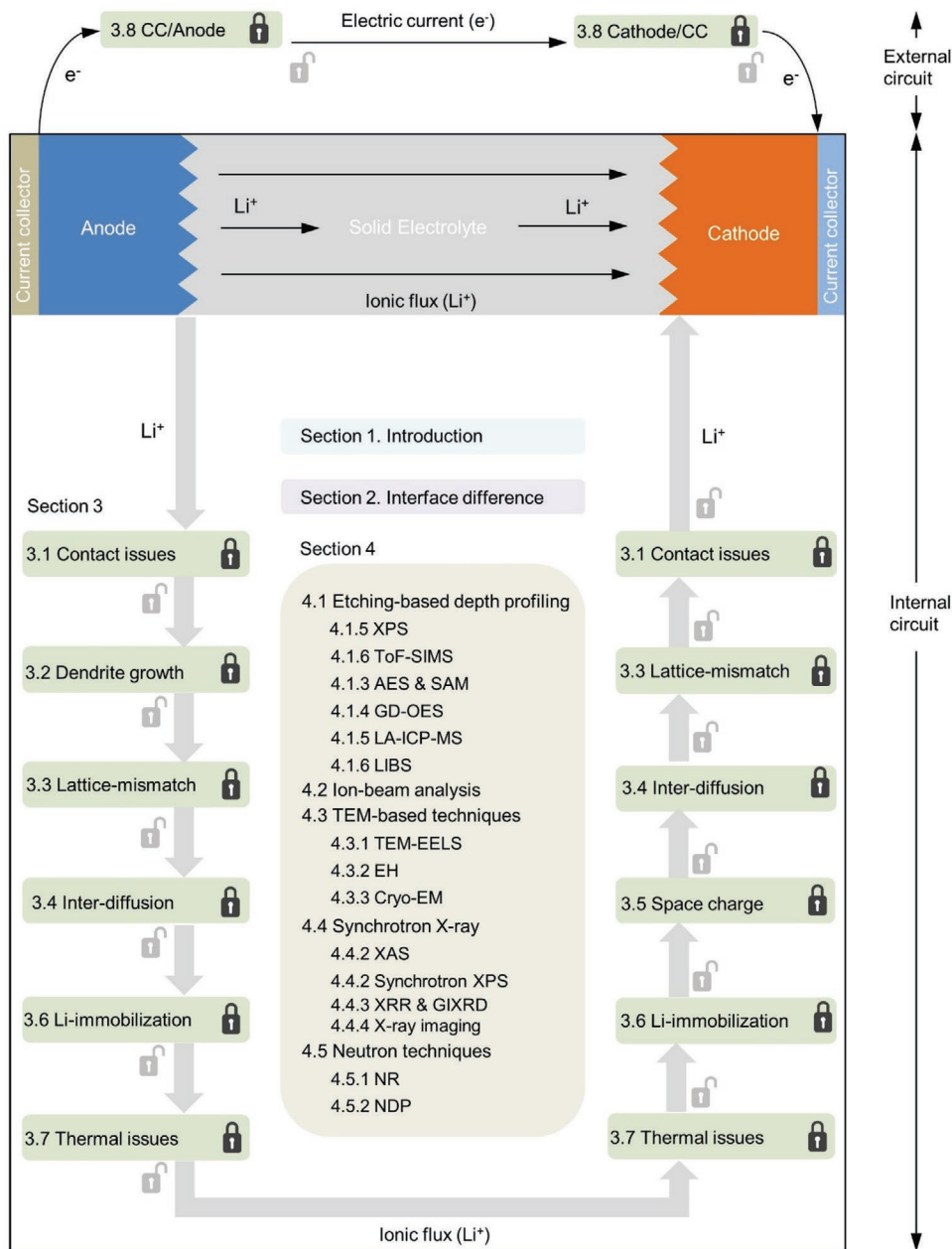Broadway, Sydney, NSW 2007, Australia

Figure 1. Chronological development of solid-state electrolytes. Black dots represent the Li-ion conductivity, and the horizontal red bars indicate the electrochemical stability windows. EC represents ethylene carbonate, PAN means poly(acrylonitrile), PEO is poly(ethylene oxide), PMMA is poly(methyl methacrylate), PC is propylene carbonate, LISICON is lithium superionic conductor, and NaSICON is sodium(Na) superionic conductor.

next-generation (H)EV. Thin-film-based ASSB, usually fabricated by deposition techniques, have layers of lithium-containing materials with a typical thickness of several microns. These thin-film batteries can be used as microbatteries, i.e., they can be integrated into miniaturized devices, such as medical implants, ambient sensors, radio-frequency identification markers, and serve as on-board power supplies.[4–6] New concepts have been developed to enhance the power and energy density of planar thin-film ASSB, such as the fabrication of 3D microbatteries.[5–7]

Intensive efforts have been made to develop high-performance ASSB in the last two decades. In the initial phase, much attention was paid to designing and synthesizing high ionic conductive SE. So far, various SE have been developed, of which polymer-,[8,9] garnet-,[10,11] NaSICON-,[12,13] and sulfide-based[14–16] are most popular due to their high ionic conductivity. **Figure 1** summarizes the development history of SE and illustrates the corresponding electrochemical stability windows and ionic

conductivities.[17–36] Recently, many high-ionic-conductive SE have been introduced, and an increasing number of studies concluded that interface properties are also essential for ASSB.[4,37–40] During the operation of ASSB, electrons and Li-ions have to pass through several interfaces. For example, when ASSB are discharged, Li-ions have to diffuse through the anode/solid–electrolyte and solid–electrolyte/cathode interface to transfer from the anode to the cathode via the solid-state electrolyte (**Figure 2**). To ensure electro-neutrality, the simultaneous transport of electrons in the external circuit must take place. Electrons leave the battery during discharging via the current-collector (CC)/anode interface and enter the battery at the opposite side via the cathode/current-collector interface. During charging, these processes are reversed. The primary energy source in ASSB are the oxidation and reduction reactions occurring at the electrode/SE interfaces. Unfortunately, imperfect interfaces may be present or formed during operation that hamper or even block the electronic and ionic fluxes.

ADVANCED
SCIENCE NEWS
www.advancedsciencenews.com

ADVANCED
ENERGY
MATERIALS
www.advenergymat.de

Figure 2. Outline of this review. An electron moves across the CC/electrode interfaces at the external circuit during discharging. Internally, Li-ions are transported between the two battery electrodes.

Regardless of applying fast ion-conducting SE, defect interfaces will limit the performance of ASSB. Understanding these interfacial characteristics in much detail and preserving well-performing interfaces are essential for optimal functioning of ASSB.

The present review highlights the relevance, pressing issues, smart designs, and analysis challenges of interfaces in ASSB. The outline of the current contribution is schematically outlined in Figure 2. We start by discussing the differences of interfaces between liquid-based and solid-state LBB in Section 2. Section 3 reviews the specific interface problems that are present in ASSB. This section focuses on the physical- and (electro)chemical-related interface problems and the potential approaches to solve these. Note that atomic-scale interface problems, like interstitials,

additives, and coatings, are not discussed herein. For more information about these subjects, the authors refer the reader to the recent review of Meng and co-workers.[41]

Interface-sensitive or depth-resolved measurement techniques, which turned out to be highly successful in investigating interfaces in ASSB, will be reviewed in Section 4. Although the tools for analyzing ASSB have been studied in some of the available scientific literature,[37,38,40–42] they mainly deal with conventional techniques, which usually give only an overall or average result. In these cases, it is not easy to obtain specific interfacial information. However, dedicated interface-resolved analytical tools can effectively determine important interface characteristics, such as the chemical–physical nature and

ADVANCED
SCIENCE NEWS
www.advancedsciencenews.com

ADVANCED
ENERGY
MATERIALS
www.advenergymat.de

location, which help to accelerate the problem-solving process and further develop high-performance ASSB. By summarizing the capabilities, limitations, and requirements of these interface- or depth-resolved techniques, we hope to offer a comprehensive guideline for interface characterizations in ASSB. Finally, a summary and outlook conclude this review in Section 5.

2. Interface Differences between Liquid and Solid LBB

Most of the current commercial LBB use nonaqueous LE, which are composed of one or multiple organic solvents and a Li-salt. These LE usually offer fast interface kinetics due to good wettability and high ionic conductivity. On the other hand, LE degrade quickly and impose safety risks because they can leak out of battery cells. Moreover, they are highly flammable and are prone to electrochemical side reactions. Driven by these safety concerns, SE have been introduced in LBB. Although safer, early-stage SE, such as Li_3N[17] and LiI,[18] are notorious due to their low ionic conductivities or narrow electrochemical stability window. However, the recent development of inorganic SE, such as $Li_{10}GeP_2S_{12}$ and Li_6PS_5Br, show high ionic conductivities, approaching those of LE.[43] A disadvantage of ASSB is that they suffer from various interfacial issues, such as physical contact and (electro)chemical instability, leading to low ionic transport across the electrode/electrolyte interfaces and capacity losses. Indeed, replacing LE with SE will change the properties and performance of LBB significantly. Therefore, in this section, we will briefly compare the interfacial differences between liquid- and solid-based LBB as a prelude for Section 3.

In LBB containing LE, the electrolyte can easily penetrate through the electrode pores, resulting in good wetting or contact of the active electrode material. Although this appears to be an uncomplicated process, it is more challenging than expected. The wetting process, followed by the battery activation or formation process, takes a relatively long time because the electrolyte needs to impregnate into the electrode pores fully. Therefore, it is a significant production cost driver.[44] If the wetting process is not performed correctly, nonuniform or incomplete wetting occurs, which might lead to inhomogeneous current distributions, unstable SEI formation, heterogeneous Li-plating, and, consequently, reduced battery performance.[45]
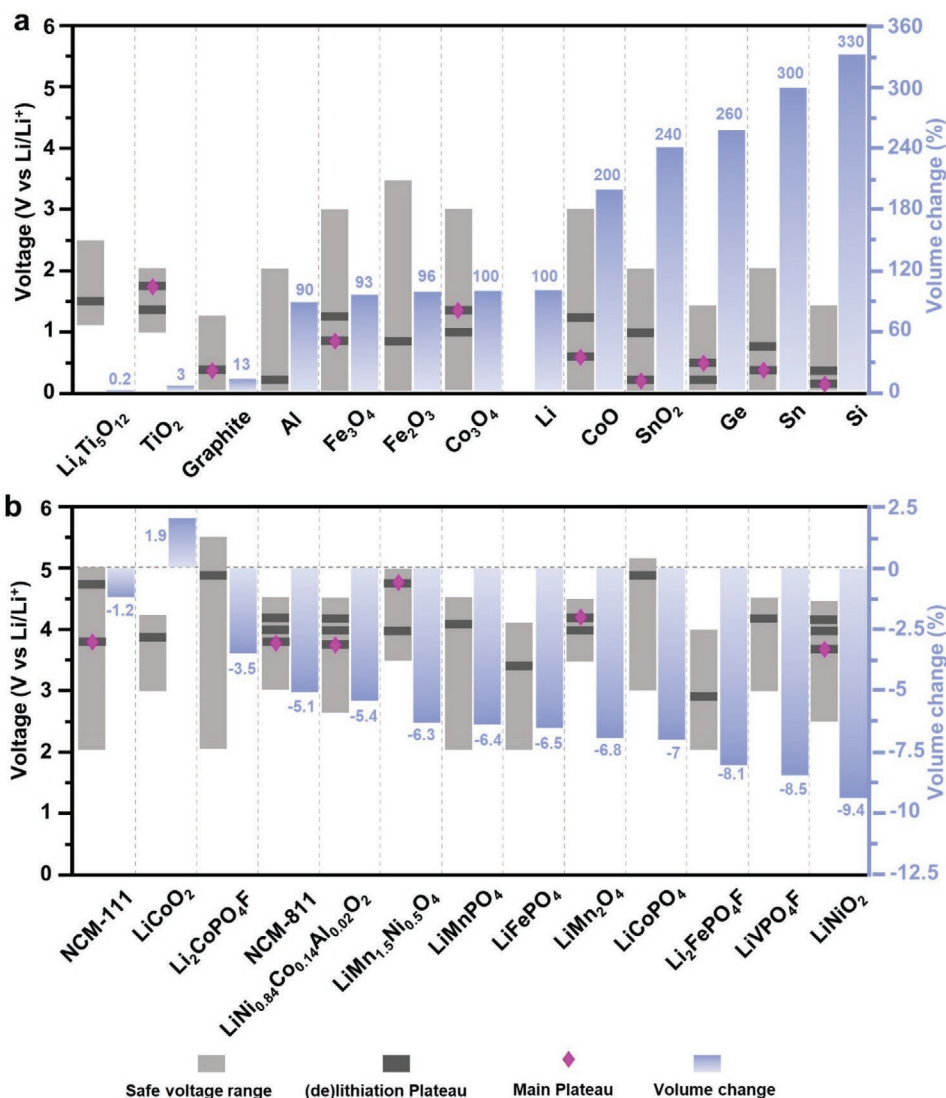
Although the above-described wetting process for liquid electrolyte-based batteries seems to be challenging, it is even harder to achieve full physical contact between electrodes and solid-state electrolytes in bulk-type ASSB. On the other hand, tight contact between different battery components can easily be obtained in thin-film ASSB because battery materials are dense and homogeneously deposited layer by layer during the fabrication process. For bulk-type ASSB, nano and microsized pores or voids are unfavorably present between the electrode particles and SE, leading to poor contacts at the solid/solid interface. Like in the liquid variant, poor contacts hinder effective transport of ions and generate a relatively high resistance, which has been reported to contribute more than 60% of the total battery resistance.[46]

Contact loss upon battery cycling between SE and electrode particles may raise additional concerns. Due to the nonflexible nature of many inorganic SE, they are practically unable

to accommodate volume changes of the electrodes during (de) lithiation. The relative volume changes of commonly used electrode materials are shown in **Figure 3**. It can be seen that the volumetric change of most anode materials is much more pronounced than that of cathode materials. Moreover, the volumetric change among the various anode materials varies a lot (Figure 3a). For example, graphite, a Li-intercalation electrode, reveals a total volume expansion of about 13% when fully lithiated to LiC_6. In contrast, Si has a volume expansion as high as 330% when being fully alloyed with Li-ions to a composition of $Li_{15}Si_4$. Considering that Si stores about 9 times more Li-ions than graphite, its 25 times higher volume change must be related to its lithiation-mechanism difference. It can be expected that for alloying electrodes, such as Si, Sn, and Ge, the volume expansions and, therefore, material detachment at interfaces are more pronounced. Sulfide and thiophosphate glasses could mitigate this effect due to their mechanically more soft nature.[47,15] However, the flexible effectiveness of these latter components needs to be further investigated. Various methods have been proposed to improve physical contacts in ASSB, such as applying mechanical pressure to the battery stacks, using hybrid or polymer electrolytes, and mixing active electrode materials with SE, creating so-called composite electrodes.

Obviously, LE can readily compensate for the volume changes of the electrodes. However, these volume changes may induce electrode cracking or even material peel-off, generating a fresh electrode surface area. In the LE case, new interphases will be formed, further consuming the available Li-ion inventory and decreasing the cell capacity.[48,49] That introduces another type of contact, referred to as (electro) chemical contact. Indeed, in comparison to physical contacts, (electro)chemical stability issues are much more complex to address. In batteries with LE, solid–electrolyte interphase (SEI) layers are generally formed at the electrode surface due to (electro)chemical reactions between the electrode and electrolyte.[48–54] The SEI formation originates from the decomposition of electrolyte solvents and/or Li-salts, which produces a multilayer structured film at the electrode surface. On some electrode materials, SEI instantly forms when being brought into contact with LE, such as Li-metal.[55,56] On other materials, such as SiO_2 and CoO, an SEI-layer forms when the electric potential drops below the decomposition potential of the LE. The SEI layer, formed at the anode, is composed of a thin dense inner layer and thicker porous outer layer[48,50] and plays a dual role in modern LBB. It prevents further decomposition of LE solvents and protects the anode from solvent co-intercalation. On the other hand, the SEI layer continuously grows and leads to irreversible capacity losses and poor rate performance.[57] The properties of these SEI layers have a substantial impact on the lifetime and batter performance. They are highly dependent on the electrode voltage, surface morphology, and composition of the electrolyte.[48] Therefore, SEI layers have already been extensively investigated and are still a relevant and timely topic in the LBB field for improving their cycling performance.[50–57]

Apart from the SEI formation in liquid-based LBB, soluble components can diffuse from one electrode through the electrolyte and deposit on the other electrode surface. This so-called chemical "crosstalk" occurs, for example, with

ADVANCED
SCIENCE NEWS
www.advancedsciencenews.com

ADVANCED
ENERGY
MATERIALS
www.advenergymat.de

Figure 3. Voltage and relative volume-change windows of various commonly used anode materials upon lithiation a) and cathode materials during delithiation b).

polysulfide components in Li–S batteries[47,58] but also with dissolved Fe in LiFePO$_4$ batteries and Mn dissolution from NMC-based cathodes.[57,59,60] Batteries with SE essentially prevent chemical "crosstalk" between the two electrodes because SE also act as a functional separator, which generally only allows Li-ions to cross.

SEI may still be formed in ASSB using polymer-based or hybrid SE due to the presence of polymeric solvents.[61] When using inorganic SE, ASSB can be free from SEI formation because of the absence of any liquid solvent. However, most inorganic SE are thermodynamically unstable against Li metal, a commonly used anode material in ASSB. Once in contact with metallic Li, most of the inorganic SE react and form an interlayer, resulting in a high interfacial resistance between the SE and electrode. That also holds for most of the SE at the high-voltage side of the electrochemical stability window. For instance, the sulfide-based SE are reported to have a relatively low oxidation potential.[16,47,15] Compared to the extensively

investigated SEI in liquid-LBB, the interlayer formation in ASSB is somewhat less known, which requires new and better understanding and investigations.

Even though Li-metal is considered as one of the most promising anode materials for high-energy-density LBB, tackling the Li-metal/electrolyte interface issues is still challenging in both liquid- and solid–electrolyte configurations. Apart from the chemical instability with most electrolytes, dendrite formation at the Li-metal/electrolyte interface significantly challenges a safe Li-metal battery operation. Dendrite issues are present in both liquid- and solid-based LBB systems, resulting from inhomogeneous Li-plating/stripping. However, the dendrite formation mechanism differs from each other. In LBB containing LE, inhomogeneous or mosaic SEI is usually formed on the surface of Li-metal anodes.[48] The inhomogeneity makes the SEI exhibit heterogeneous Li-ion conductivity, which would result in inhomogeneous Li-plating and stripping at the Li-metal surface.[62,63] Once the Li-nucleation occurs inhomogeneously,

ADVANCED
SCIENCE NEWS
www.advancedsciencenews.com

ADVANCED
ENERGY
MATERIALS
www.advenergymat.de

Li-dendrites will grow in a self-enhanced manner due to the electric field enhancement at the dendrite tip.[64] In ASSB, the inhomogeneous physical contacts at electrode/solid–electrolyte interface and heterogeneous conductivity of SE facilitate dendrite nucleation. Another apparent difference between the two systems lies in the dendrite growth mechanism. In the LE layout, dendrites can quickly grow because LE can hardly mechanically block their growth pathways. It was initially assumed that inorganic SE could inhibit the growth of Li-dendrites due to the high shear modulus. Monroe and Newman suggested a critical shear modulus of 6.8 GPa, twice that of Li-metal, for a solid–electrolyte to block Li-dendrite growth. Almost all inorganic SE satisfy this criterion.[65] However, dendrite formation and penetration are still observed along the grain boundaries of inorganic SE, such as the Garnet-type $Li_7La_3Zr_2O_{12}$[66] and Argyrodite-type Li_6PS_5Cl,[67] regardless of their high mechanical strength.

At the interface between electrode and electrolyte of batteries that contain an LE with mobile ions, a so-called electrochemical double layer (EDL) is formed. Although electroneutrality usually prevails in the bulk region of the electrolyte, the EDL region may considerably deviate from electroneutrality.[68] This might cause an additional resistance.[69,70] A similar effect occurs at the electrode/SE interface of ASSB. When two solid materials with different chemical potential contact each other, and the atoms and electrons cannot establish local charge neutrality, a charge will be build up at the interface, called the space-charge layer. Whether space-charge layers are beneficial or detrimental for the battery performance is not yet clear. In addition, the thickness of space charge layer is also disputable.

A major disadvantage of LBB containing LE is that they are prone to thermal runaway, especially during abuse conditions, such as electrical abuse (e.g., over (dis)charge), mechanical abuse (e.g., nail penetration), and thermal abuse (e.g., overheating). Thermal runaway occurs after a chain of exothermic reactions in a short time, leading to a massive temperature increase, which can further develop to smoke release, fire, and/or explosion. Various methods have been investigated to prevent thermal runaway events, which can be taken at multiple levels, such as the electrode/electrolyte-material level, the cell level, the system level, and the (battery) management level.[71–74] One of the key changes on the material level for mitigating thermal runaway is the replacement of LE into SE. It is evident that SE improve the thermal stability of LBB, but that does not mean that thermal runaway cannot occur in LBB containing SE. Indeed, thermal runaway also can occur in ASSB.[75,76] However, the temperature at which thermal runaway occurs is, generally, far higher than that of LE-based systems. Therefore, ASSB can be considered as safer systems in comparison to the liquid counterparts.

From the above-described differences between LE-based and SE-based batteries, it can be concluded that the interfacial features for both systems are analogous. SE-based batteries clearly have a safety advantage compared to their liquid-based counterparts. Still, the existing major interfacial problems make them less mature. At the same time, the development history of SE-based batteries is considerably shorter than that of the LE-based batteries, which makes it unfair to compare both systems in that respect. On the other hand, research on SE-based batteries has already made great progress, such as the significant increase in ionic conductivity of SE.[43] However, interfacial issues remain a topic of concern. In Sections 3 and 4, the current interfacial challenges, tailoring-, and interface-resolved measurement techniques are comprehensively reviewed. With the detailed insights of these two sections, we propose our important perspectives that will enable future advancements of ASSB.
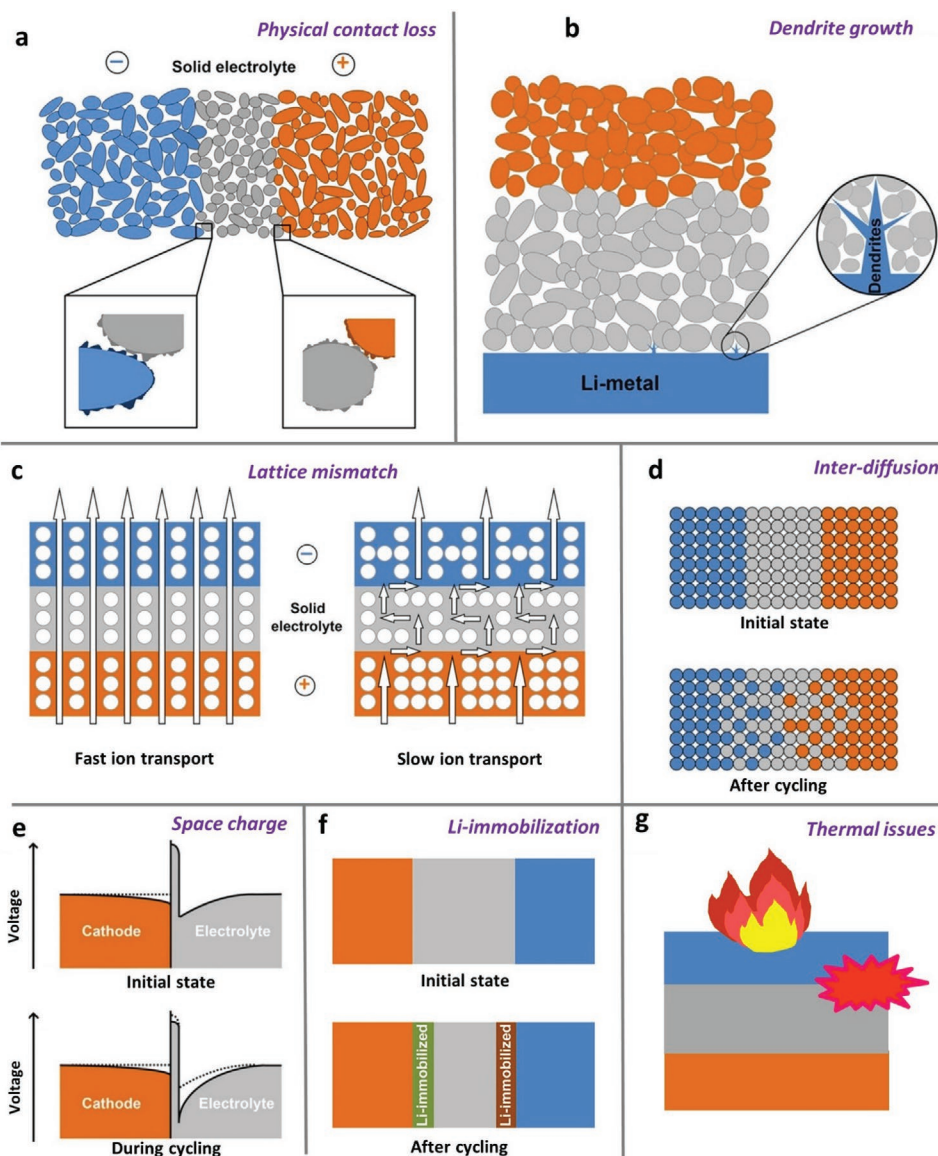
3. Interface Challenges and Tailoring Strategies

Interfaces have a significant influence on the electronic and ionic transport between different components in LBB. The solid-state nature of ASSB makes transport across interfaces even more complicated than in liquid-based battery systems. Perfect interfaces in ASSB should be mechanically and (electro) chemically stable, have minimal interfacial impedance, and provide conformal contact on an atomic scale between the individual battery layers.[77–79] In practice, however, such perfection is difficult to achieve, and interfacial issues, such as contact issues,[80,81] dendrite growth,[37,82] lattice mismatch,[83] interdiffusive layer formation,[84–86] space-charge layer formation,[87,88] Li-immobilization,[4] and thermal issues[75,76] are often found in ASSB. The various interface problems occurring in ASSB are illustrated in **Figure 4**a–g and will be further explained below.

3.1. Contact Issues

Imperfect contacts pose a grand challenge to ASSB and may arise from physical and chemical aspects. Contact losses already occur during the battery fabrication process and may deteriorate further during cycling. Physical contact problems mostly occur in bulk-type ASSB, as schematically shown in Figure 4a. Atomic-scale and conformal contacts are highly preferred for obtaining the best performance. However, these perfect contacts are difficult to achieve in practice due to the particle–particle contact and pore presence.

A standard method to improve the mechanical contact is by applying high pressure during cell production and cycling, which helps to achieve better interface contact and decrease the interfacial resistance.[89] However, for Li-metal-based ASSB, the stack pressure should be optimized and controlled within an appropriate range. Applying too high pressure, especially during battery operation, could cause detrimental shorts. Too low pressures, on the other hand, may lead to poor-performing batteries. Doux et al. suggested that for fabricating a $Li/Li_6PS_5Cl/Li$ symmetric cell, an intermediate stack pressure (≤25 MPa) enhances the anode/solid–electrolyte contact and therefore reduces the interfacial resistance.[90] After fabricating the battery stacks at a pressure of 25 MPa, the batteries were cycled by Li plating and stripping at various stack pressures. The graph of **Figure 5**a schematically shows the effect of pressure on the mechanical integrity of SE as a function of cycling. At low-pressure cycling (5 MPa), no shorts are observed up to 1000 h. This observation suggests that an applied stack pressure of 5 MPa is sufficient to enable proper contact between Li-metal and the solid–electrolyte. Li-metal creeping through the

**ADVANCED
SCIENCE NEWS**
www.advancedsciencenews.com
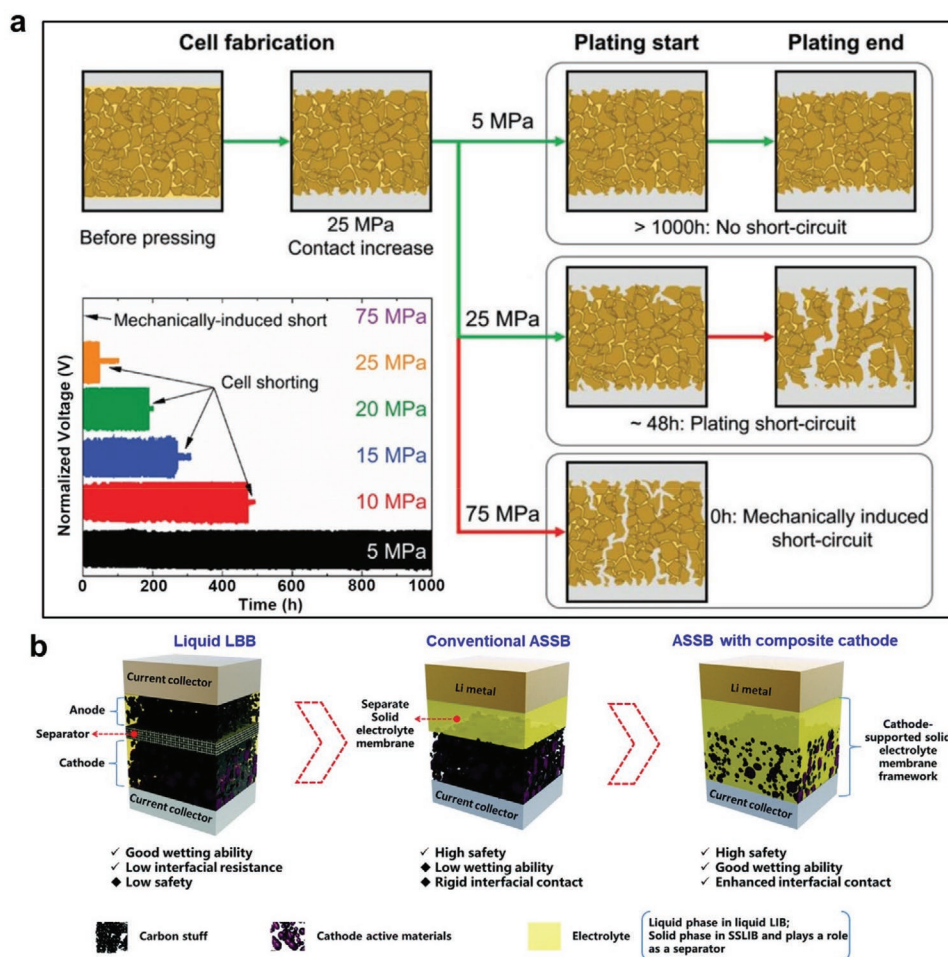
**ADVANCED
ENERGY
MATERIALS**
www.advenergymat.de

Figure 4. Schematic illustration of physical contact loss in bulk-type ASSB a), dendrite growth in Li-metal ASSB b), lattice-(mis)match c), interdiffusion of chemical elements between battery layers d), space-charge layers build-up due to lithium concentration differences at the interface between the electrodes and SE e), Li-immobilization layer formation in ASSB f), and thermal issues g).

electrolyte, leading to shorting, is absent. When the stack pressure was increased to 10, 15, 20, and 25 MPa during cycling, the batteries were shorted after 474, 272, 190, and 48 h of cycling, respectively. It was argued that Li-metal creeps into the solid–electrolyte pores, in which Li-dendrites can form, propagate, and eventually short the battery stack during Li plating and stripping at higher pressures. When the stack pressure is further increased to 75 MPa for cycling, mechanically induced shorts immediately occur, even before applying a current. These shorts occur because the high stack pressure leads to a severe creep of soft metallic Li through the solid–electrolyte.

Bulk-type ASSB electrodes containing pure active material generally show slow ionic diffusion due to the presence of pores between powders. To resolve this problem, SE powders/slurries can be mixed/tape-cast with active electrode materials

to increase the interfacial contact and ameliorate ionic diffusion properties. Figure 5b illustrates three different battery-concept examples: 1) a liquid LBB; 2) a conventional ASSB with a pure cathode; and 3) an ASSB with a solid–electrolyte mixed composite cathode.[91] ASSB produced with composite cathodes show improved kinetics in comparison with batteries containing pure active electrode materials. Although composite electrodes reveal fast ionic transport, blending techniques unfavorably decrease the electrode loading, leading to lower effective storage capacities.

For ASSB containing Li-metal anodes, further improvements in wetting or better contact with the SE can be achieved by melting and then depositing Li-metal on SE instead of pressing. The molten Li-metal with relatively high fluidity will fill the rough solid–electrolyte surface gaps and therefore increase the

**ADVANCED
SCIENCE NEWS**
www.advancedsciencenews.com

**ADVANCED
ENERGY
MATERIALS**
www.advenergymat.de

Figure 5. Schematic representation of the stack pressure on the shorting behavior of Li-metal ASSB a). The inset of (a) shows the indicative voltage of Li-symmetric batteries as a function of time during plating and stripping at different stack pressures. At 75 MPa, the cell already mechanically shorts before cycling begins. At 5 MPa, no shorts were observed for over 1000 h. b) shows schematic development of technology starting from liquid-based LBB (left), towards ASSB with the pure cathode (middle), and finally to ASSB with the solid–electrolyte mixed composite cathode (right). a) Reproduced with permission.[90] Copyright 2019, Wiley-VCH. b) Reproduced with permission.[91] Copyright 2019, The Royal Society of Chemistry.
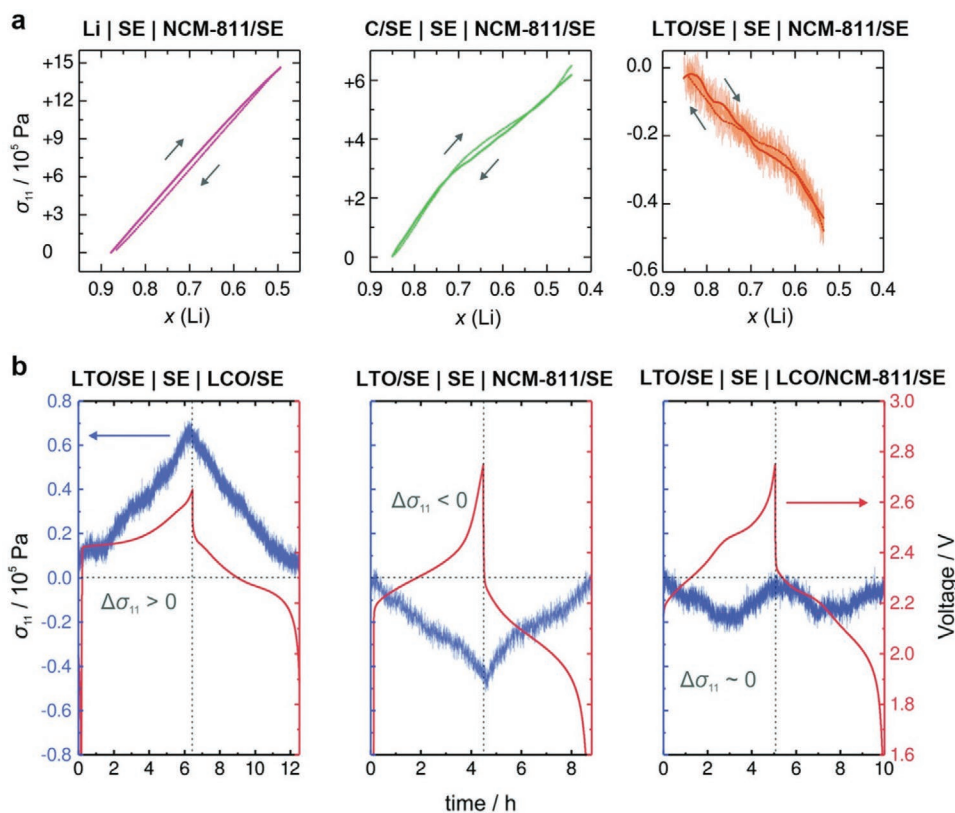
contact area. However, some materials, such as garnet-type SE, cannot be optimally wetted by molten lithium due to their lithiophobic properties. Therefore, the wetting process of molten Li metal can be improved by (surface) modification, such as by using buffer layers, modified surface topography, and higher deposition temperature.[92] Another potential approach is to use hybrid SE, which contain flexible polymers. However, safety concerns should then be reconsidered.[93]

Physical contact problems can also result from electrode-volume changes upon (de)lithiation. As summarized in Figure 3, almost all electrode materials show volumetric variations during lithium insertion and extraction, which induces a volume-breathing effect for full battery stacks. Undesirable deformation may lead to dead space and high internal charge-transfer resistance due to the formation of cracks and voids. That will result in electrochemical isolation of active material particles. Among the anode candidates, spinel $Li_4Ti_5O_{12}$ only has a 0.2% volume change, even upon intercalation of 3 Li^+ per formula unit. Therefore, $Li_4Ti_5O_{12}$ is considered a "zero-strain" electrode material, which is highly favorable for ASSB.

Figure 6a shows operando stress measurements of ASSB containing various anode materials.[94] It can be seen that the batteries with Li-metal (left) and graphite/SE (middle) anode show large stress variations. The high stress level in the battery with Li-metal anodes is attributed to the strong volumetric changes of metallic Li during plating/stripping. Both plating and stripping will cause considerable changes at the interface. When $Li_4Ti_5O_{12}$/SE replaces Li-metal and graphite/SE, the stress decreases by at least one order of magnitude (right-hand side of Figure 6a).

Maintaining the mechanical integrity of cathode materials is also essential for high-stability ASSB. Apart from $LiCoO_2$, most cathode materials suitable for ASSB shrink during delithiation (Figure 3b). Moreover, the volume changes among the listed cathode materials are within 10%. Though a bit lower than for anode materials, unfavorable volume changes at the cathode side can still result in detrimental stress in complete battery stacks. Inspired by the performance of $Li_4Ti_5O_{12}$, Koerver et al. designed a similar "zero-strain" cathode material to mitigate the internal stress of ASSB. Figure 6b shows

**ADVANCED
SCIENCE NEWS**
www.advancedsciencenews.com

**ADVANCED
ENERGY
MATERIALS**
www.advenergymat.de

Figure 6. Galvanostatically induced changes of the uniaxial stress for ASSB with different anode configurations a). Comparison of the stress response of $Li_4Ti_5O_{12}$–SE/SE/cathode–SE using $LiCoO_2$, NCM-811 and a blend of 55:45 wt% NCM-811:$LiCoO_2$ cathode composite, in which blue and red lines represent stress and voltage evolution, respectively b). a,b) Reproduced with permission.[94] Copyright 2018, The Royal Society of Chemistry.

the stress response of $Li_4Ti_5O_{12}$–SE/SE/cathode–SE using $LiCoO_2$ (left) and $LiNi_{0.8}Co_{0.1}Mn_{0.1}O_2$ (NCM-811) as cathode material (middle).[94] The battery using $LiCoO_2$ reveals positive stress during battery operation, and the battery containing NCM-811 shows a negative stress response. Mixing these two materials with an optimized ratio could potentially result in a "zero-strain" cathode material. The authors, therefore, blended $LiCoO_2$ with NCM-811 (55:45 wt%) into a composite cathode. As a result, the battery ($Li_4Ti_5O_{12}$–SE/SE/$LiCoO_2$–NCM–SE) using a composite cathode of $LiCoO_2$ and NCM-811 showed a lower nominal stress level and nearly "zero-strain," as shown in the right-hand plot of Figure 6b.

Another type of contact problem may arise from an (electro) chemical point of view. An optimal chemical contact forms no interlayer when two battery components contact each other and is also stable during electrochemical cycling. Compatible interfaces require matching the electrochemical stability window of both SE (Figure 1) and electrode materials (Figure 3). For example, binary Li-salts, like Li_3N, LiF, and LiI, are chemically stable in contact with metallic Li. As schematically shown in **Figure 7**a (interface type 1), no interlayer is formed with such stable materials. They are also stable upon electrochemical cycling. In some chemically stable interface configurations, the used SE reveal low ionic conductivity, leading to lower power performance. SE with high ionic conductivity, such as the sulfide-based types, are always preferred in practical applications.[15] However, interlayers are frequently formed at the

interfaces of these highly conductive SE. Interlayers can immediately be created when two materials contact due to chemical reactions (interface type 2 in Figure 7b). It is also possible that an interface is initially stable when two materials make contact, but this may change during electrochemical cycling due to electrochemical reactions, as Figure 7c shows (interface type 3).

The properties of an initially formed interlayer (interface type 2 and 3, Figure 7b,c) can, in turn, affect the ongoing electrochemical behavior. Depending on the electronic and Li-ionic conductivity, the formed interlayers can be divided into four groups,[95] shown in Figure 7d–g. Interlayer type 1 (Figure 7d) is an interlayer with high electronic and ionic conductivity, which continuously grows during cycling due to (electro)chemical reactions. If the interlayer has a low ionic conductivity and high electronic conductivity, then the electrochemical redox reactions will continually cause solid–electrolyte degradation and interlayer thickness growth (Figure 7e). An interlayer with low ionic and low electronic conductivity (interlayer type 3 in Figure 7f) cannot grow during cycling but leads to a sizeable interfacial resistance and, therefore, poor-performing batteries. The preferred interlayer should reveal high ionic and low electronic conductivity. This type of interlayer, shown by Interlayer type 4 in Figure 7g, will initially grow due to electrochemical side reactions. When the interlayer grows to a certain thickness, further formation is suppressed.[95] Consequently, the formed interlayer could enlarge the electrochemical stability window of SE without increasing the interfacial resistance. It is worth noting that electrodes may be involved in chemical or
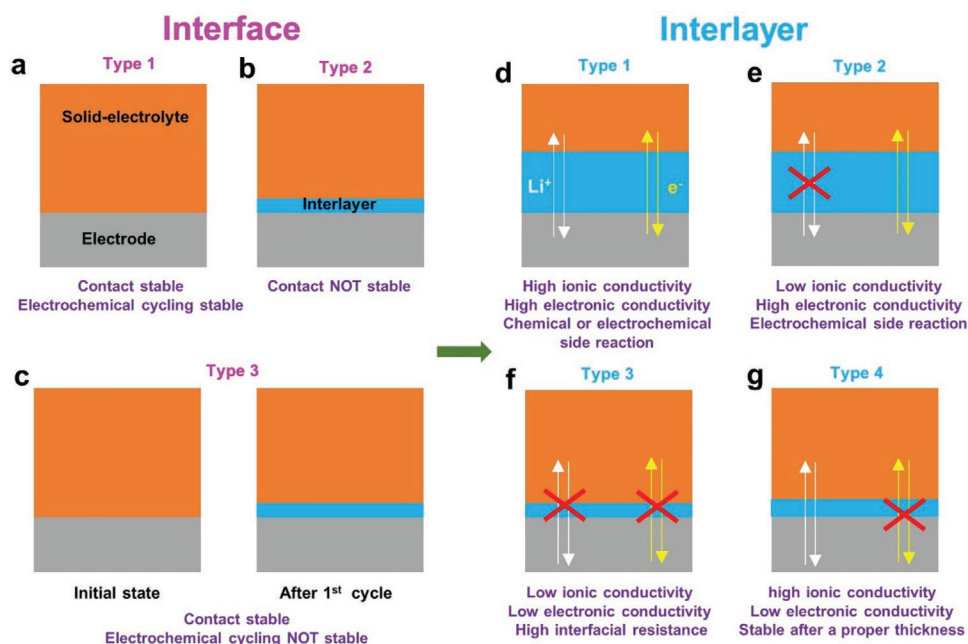
Figure 7. Schematic representation of various types of interfaces and interlayers formed in ASSB. Interface type 1 remains stable upon material contact and during electrochemical cycling a). Interface type 2 is unstable upon contact and during electrochemical cycling b). Interface type 3 is stable upon contact but will change during electrochemical cycling c). Interlayers formed at unstable interfaces have different behavior during cycling according to its electronic and ionic properties: Interlayer type 1 with high ionic and electronic conductivities will continuously grow due to chemical or electrochemical side reactions d). Interlayer type 2 with low ionic and high electronic conductivities will continue to grow due to electrochemical reactions e). Interlayer type 3 with low ionic and low electronic conductivities will not grow but lead to high interfacial resistances f). Interlayer type 4 with high ionic and low electronic conductivities will grow to a certain thickness and then stabilize g).

electrochemical redox reactions of SE. That will bring additional complications into the interlayer chemistry and add difficulties in understanding of the operation of interfaces. Moreover, the interlayers mentioned above are considered to operate under simplified "theoretical" conditions. In reality, multiple interlayers may be present at one interface, such as space charge, interdiffusive region, and Li-immobilization layer. In summary, contact issues in ASSB are determined by the microstructure, processing conditions, and homogeneity of the materials. They are unique for selected SE and electrode combinations. Therefore, interface contacts in ASSB should be considered case by case.
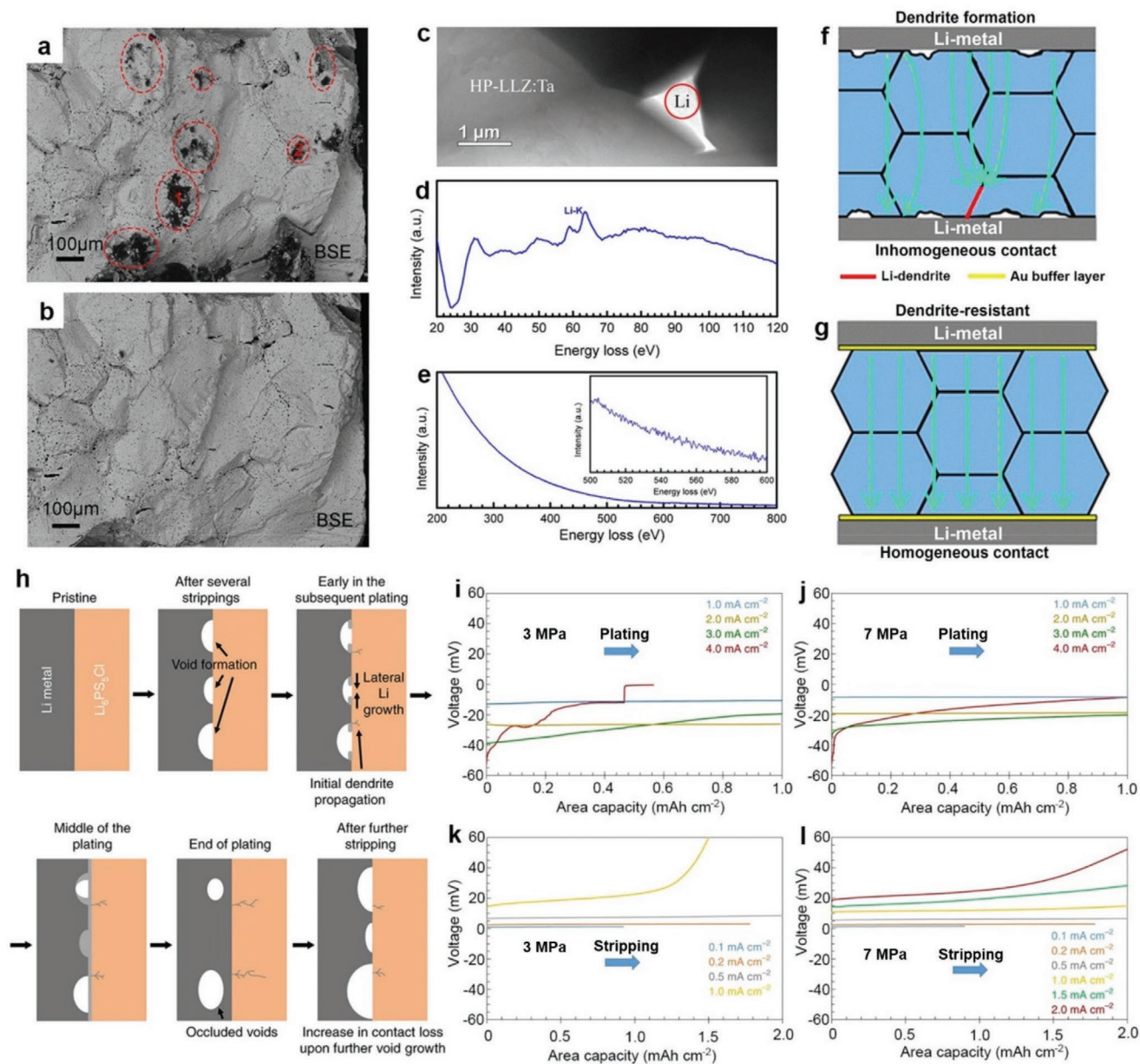
3.2. Dendrite Growth

Li-metal is an ideal anode material for lithium-based batteries due to its extremely high capacity and low density. However, dendrite formation, as schematically depicted in Figure 4b, can be fatal for the proper operation of Li-metal cells.[96] It has been widely demonstrated that dendrite penetration along grain boundaries is the dominant mechanism causing battery failure. Ren et al. investigated $Li/Li_{6.75}La_3Zr_{1.75}Ta_{0.25}O_{12}/Li$ symmetric batteries on shorts caused by dendrites. They concluded that the cycling time before batteries short shows a positive correlation with an increasing SE pellet density.[97] **Figure 8**a shows SEM cross-sectional observations in the backscattered electron (BSE) mode of a $Li_{6.75}La_3Zr_{1.75}Ta_{0.25}O_{12}$ pellet from a battery that shorted. On the solid–electrolyte pellet one can see black dots, which are mainly located in the grain boundary regions. From

these dark-colored areas and the high reactivity with ethanol (Figure 8b), the authors concluded that these dots are Li-dendrites. That is, however, indirect proof of dendrite propagation along solid–electrolyte grain boundaries. Tsai et al. identified Li-dendrites in $Li_7La_3Zr_2O_{12}$ grain boundaries with transmission electron microscopy (TEM)–electron energy loss spectroscopy (EELS) measurements after shorting $Li/Li_7La_3Zr_2O_{12}$ symmetric batteries.[66] The results from these TEM–EELS measurements are shown in Figure 8c–e. These results confirmed the Li-dendrite growth along the grain-boundary pathways.

Dendrite formation can be linked to inhomogeneous contacts between the SE and Li-metal anodes. A schematic representation is shown in Figure 8f.[66] The voids at $Li/Li_7La_3Zr_2O_{12}$ interface are the hot-spots for dendrite nucleation and growth due to the higher surface activity and thus lower nucleation activation energy. When the solid–electrolyte pellet surface is polished and subsequently flattened by the deposition of a thin gold buffer layer, no dendrites were formed under the same current-loading and pressure conditions (Figure 8g). However, Li-dendrites still might be formed at higher current densities in batteries with a gold buffer layer deposited at the solid–electrolyte surface. That can be attributed to the different ionic conductivities between the solid–electrolyte bulk and grain boundaries, causing inhomogeneous Li-plating, dendrite growth, and, finally, short circuits. From these results, it can be concluded that a more uniform conductivity between the bulk and grain boundaries in SE results in dendrite-free and, therefore, long-life ASSB.

Generally, save Li-plating should be performed below the so-called critical current density (CCD), which nowadays lies in the

**ADVANCED
SCIENCE NEWS**
www.advancedsciencenews.com

**ADVANCED
ENERGY
MATERIALS**
www.advenergymat.de

Figure 8. Cross-sectional SEM images of a short-circuited $Li_{6.75}La_3Zr_{1.75}Ta_{0.25}O_{12}$ pellet before a) and after ethanol rinsing b). TEM image c) and EELS d,e) of a $Li_7La_3Zr_2O_{12}$ pellet from a shorted battery. Schematic illustration of the current flow pathways at a rough f) and smooth interface g). Evolution scheme of a Li/Li_6PS_5Cl interface when cycled at an applied current density above the critical current density h). Voltage–charge plots for three-electrode Li/Li_6PS_5Cl batteries at different indicated pressures and current densities i–l). a,b) Reproduced with permission.[97] Copyright 2015, Elsevier. c–g) Reproduced with permission.[66] Copyright 2016, American Chemical Society. h–l) Reproduced with permission.[67] Copyright 2019, Springer-Nature.

range of about 0.5 to 1.0 mA cm^{-2}. Exceeding the CCD results in dendrite formation and gradual penetration through the SE.[66,97] Recently, however, it was demonstrated that a CCD also exists for Li-stripping, the reverse process of plating. Kasemchainan et al. performed three-electrode measurements using reference electrodes in $Li/Li_6PS_5Cl/Li$ batteries to investigate the plating and stripping effects.[67] The authors found that when the current density for stripping exceeds the rate at which mechanical deformation can replenish lithium, voids will start to form at the lithium surface. This behavior is schematically shown in Figure 8h. Upon the subsequent plating, the created voids are only partially filled

with Li-metal and become isolated from the electrode/solid–electrolyte interface at the end of plating. The following stripping cycle increases the void-volume again, which reduces the interface contact area, causing polarization and increasing local current densities at the Li-metal surface. As a result, the local current density rises above the CCD, even when the average applied current density is much lower than the dendrite formation threshold during plating. For a fresh and void-free cell at a stack pressure of 3 MPa, a CCD of 2.0 and 0.2 mA cm^{-2} was found for plating (Figure 8i) and stripping (Figure 8k), accordingly. The same authors also showed that the CCD was dependent on the stack pressure. For

**ADVANCED
SCIENCE NEWS**

www.advancedsciencenews.com

**ADVANCED
ENERGY
MATERIALS**

www.advenergymat.de

example, when the stack pressure increased to 7 MPa, the CCD for stripping can be increased up to 1.0 mA cm^{-2} (Figure 8l). The authors argued that a higher stack pressure causes lithium to creep to replenish voids, resulting in a conformal Li/solid–electrolyte contact, thereby increasing the dendrite formation threshold. These findings are consistent with the observations of Wang et al., who showed that the primary factor limiting Li-ion transport at low stack pressures is insufficient lithium creep rather than Li-ion diffusion.[98] It should be emphasized again that the stack pressure should be well-tuned for increasing the performance and lifetime of Li-metal ASSB. For example, a too high stack pressure leads to additional production costs by pressure-applying components. It may also cause mechanical shorts in the worst case, as indicated in Figure 5a. On the other hand, a too low stack pressure might lead to poor battery performance, as discussed in Section 3.1.

Obviously, there is still a long way to go for the development process of high-power and dendrite-free Li-metal ASSB. For instance, the reported CCD of 0.2 to 1.0 mA cm^{-2} is still much lower than the current automotive applications requirements (≈10 mA cm^{-2}).[77] Intensive efforts have already been devoted to increasing the CCD for high-power Li-metal ASSB. It can be concluded that dendrite problems mainly originate from local,

inhomogeneous plating, resulting from physical and electrochemical related aspects. Physically, imperfect physical contact or wetting problems between Li-metal and SE, such as voids and other contact losses, are prominent hotspots for initializing the dendrite formation process. Heterogeneous Li-plating, an electrochemical process, may rise from ionic conductivity differences across interfaces and grain boundaries of SE. Any strategies that ameliorate these physical and electrochemical properties to accomplish homogeneous Li-plating will further facilitate the development of dendrite-free ASSB.

Physically related issues can be addressed by modifying Li-metal anode or SE to establish firm contacts or good wetting. To improve the wettability of Li-metal, Duan et al. synthesized a Li-graphite composite electrode by incorporating graphite powder into molten Li-metal.[99] During thermal mixing at 250 °C, graphite was chemically lithiated and homogeneously dispersed in the Li-metal matrix. Compared to a pure Li-metal anode, the prepared composite-anode shows excellent wetting with garnet-type SE, resulting in a firm electrode/SE interface. A schematic example of this process shown in **Figure 9**a. Figure 9b confirms that the composite-anode/solid–electrolyte interface could endure a CCD up to 0.8 mA cm^{-2} without suffering from dendrite formation.
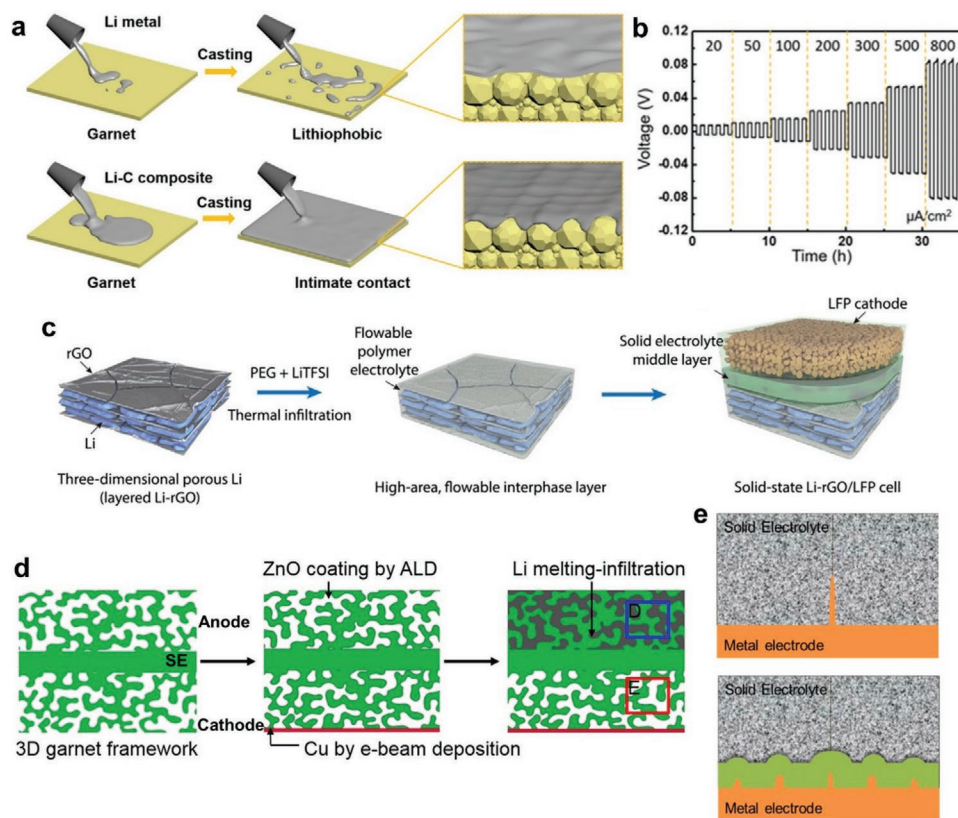
Figure 9. Schematic representation of the synthesis procedure for casting pure Li-metal and Li–C composite on garnet-type SE a), rate performance of Li–C/SE/Li–C symmetric cells at different current densities at room temperature b), scheme of a synthesis procedure for fabricating a 3D Li–rGO anode and full battery c), schematic representation of the preparation procedures of a 3D ionic-conductive framework containing Li$_7$La$_{2.75}$Ca$_{0.25}$Zr$_{1.75}$Nb$_{0.25}$O$_{12}$ for constructing 3D Li-metal ASSB d), and e) shows the schemes of Li-dendrite growth with a chemically stable interface (top) and with an unstable interface (bottom). a,b) Reproduced with permission.[99] Copyright 2019, Wiley-VCH. c) Reproduced with permission.[122] Copyright 2017, American Association for the Advancement of Science. d) Reproduced with permission.[123] Copyright 2018, National Academy of Sciences of the United States of America. e) Reproduced with permission.[95] Copyright 2017, American Chemical Society.

Indeed, Li-metal is a very reactive material, which seriously challenges its modification process. Generally, optimizing the wettability of SE is much easier than that of Li-metal. The most widely adopted approach for improving the wettability of SE is to synthesize hybrid SE-containing polymers and inorganic components. Hybrid composite SE combine the advantages of the high flexibility of polymers, enabling optimal contact at the interface, with the rigidness of inorganic SE, which ideally prevents dendrite penetration. For example, Peng et al. prepared a composite solid–electrolyte containing $Li_{1.5}Al_{0.5}Ge_{1.5}(PO_4)_3$ as an inorganic conductor, PEO as a polymeric conductor, and succinonitrile as a solid plasticizer to make the composite flexible. The synthesized composite-SE showed a high ionic conductivity of 1.26×10^{-4} S cm^{-1} and a strong capability of impeding dendrite formation.[100] $Li_{1.5}Al_{0.5}Ge_{1.5}(PO_4)_3$ particles were also incorporated into polymer–polycaprolactone (PCL) to obtain a composite electrolyte that could prevent dendrite growth at current densities up to 4 mA cm^{-2} during lithium plating.[101] Various synthesized composite-SE to obtain dendrite-free Li-metal ASSB are summarized in **Table 1**.[100–111]

Apart from optimizing Li-metal and SE, interposing an artificial buffer layer can improve the interfacial physical contact and prevent dendrite formation. The proposed buffer materials should comply with several criteria, such as being chemically stable against Li-metal and used SE, ionically conductive, and having a high shear modulus.[112] Ahmad et al. applied a machine-learning method to computationally screen 12 950 inorganic solids and over 15 000 interfaces for preventing dendrite formation.[113] Using this machine-learning method, the authors found six suitable SE-types capable of inhibiting dendrite formation and penetration, which can be used in more than 20 interface combinations.

Various experimental studies have been performed in which artificial buffer layers were investigated for improving the dendrite-blocking performance. Han et al. deposited an ultrathin (5–6 nm) Al_2O_3 film between a garnet-type solid–electrolyte ($Li_7La_{2.75}Ca_{0.25}Zr_{1.75}Nb_{0.25}O_{12}$) and Li-metal anode.[114] The deposited Al_2O_3 enables a conformal and chemically stable contact between Li-metal with solid–electrolyte as well as a significantly reduced interfacial resistance, which decreased from 1710 to 1 Ω cm^2. Moreover, thermal heating lithiated the Al_2O_3 buffer-layer. The ultrathin and conformal lithiated Al_2O_3 will offer fast pathways for lithium-ion transport and can, therefore, successfully be used for suppressing dendrite formation. Other materials, such as Au,[66] Mg,[115] Al,[116,117] Si,[118] Bi,[119] ZnO,[120] and LiPON,[121] also have been reported as successful buffer-layer candidates for good interfacial wetting, preventing Li-dendrites.

The modification of Li-metal and SE can also alleviate electrochemically induced nonuniform Li-plating, but from different perspectives than discussed above. For example, at the Li-metal anode side, 3D-structured electrode designs help prevent dendrite formation because the 3D surface geometry reduces the current density below the defined CCD. Liu et al. fabricated a 3D porous Li-anode by incorporating lithium into a layered reduced-grapheme-oxide (rGO) host. The synthesis procedure for producing this 3D anode and a full battery is shown in Figure 9c.[122] A significant C-rate and cycling capability improvement were achieved when assembling 3D Li-rGO anodes into solid-state full batteries compared to conventional pure Li-metal foil as an anode. Yang et al. synthesized a 3D ion-conductive framework as a host for a Li-metal anode made of a garnet-type SE ($Li_7La_{2.75}Ca_{0.25}Zr_{1.75}Nb_{0.25}O_{12}$).[123] Figure 9d shows a schematic representation of the preparation procedure. The porous structures in the conductive framework allowed smooth Li-metal deposition without

Table 1. Various synthesized composite-SE for dendrite prevention.

Inorganic part	Organic part	Other Li-salts or additives	Ionic conductivity [mS cm^{-1}]	Highest current density reached [mA cm^{-2}]	Ref.
$Li_{1.5}Al_{0.5}Ge_{1.5}(PO_4)_3$	PEO	Succinonitrile, lithium bis(trifluoromethanesulfony)imide (LiTFSI)	0.14 at 30 °C	0.2 at 40 °C	[100]
	PCL	Succinonitrile, LiTFSI	0.6 at room temperature	4 at 30 °C	[101]
$Li_{1.3}Al_{0.3}Ti_{1.7}(PO_4)_3$	Crosslinked poly(ethylene glycol) methyl ether acrylate	LiTFSI	0.1 at 65 °C	0.5 at 65 °C	[102]
$Li_{1.4}Al_{0.4}Ti_{1.6}(PO_4)_3$	Polyacrylonitrile (PAN) and PEO	LiTFSI	0.65 at 60 °C	0.3 at 60 °C	[103]
$Li_7La_3Zr_2O_{12}$	γ-Methyl-propylene trimethoxysilane, vinylene carbonate	Lithium difluoro(oxalate) borate (LiDFOB)	0.34 at room temperature	2 at room temperature	[104]
$Li_{1.4}Al_{0.4}Ge_{1.6}(PO4)_3$	Epoxy polymer		0.16 at room temperature	1.4 at room temperature	[105]
Lithium montmorillonite	Poly(ethylene carbonate)	LiTFSI	0.35 at room temperature	0.5 at room temperature	[106]
$Li_{6.4}La_3Zr_{1.4}Ta_{0.6}O_{12}$	PEO	LiDFOB	0.11 at 60 °C	0.1 at room temperature	[107]
$Li_{6.5}La_{2.5}Ba_{0.5}NbZrO_{12}$	PEO	LiClO$_4$	0.1 at room temperature	0.1 at room temperature	[108]
	Polyethylene glycol, diphenylmethane diisocyanate	Lithium 2,2-dimethylolpropionic, LiTFSI	0.1 at room temperature	1 at room temperature	[109]
$Li_{10}GeP_2S_{12}$	Poly(vinylidene fluoride-co-hexafluoropropylene), perfluoropolyether	LiTFSI	0.18 at room temperature	0.2 at room temperature	[109]
$Li_{6.28}La_3Al_{0.24}Zr_2O_{12}$	Poly(ethylene glycol) diacrylate	LiTFSI	0.39 at room temperature	0.5 at room temperature	[111]

**ADVANCED
SCIENCE NEWS**

www.advancedsciencenews.com

**ADVANCED
ENERGY
MATERIALS**

www.advenergymat.de

forming Li-dendrites (Figure 9d). Strikingly, the prepared 3D structure showed stable plating and stripping at 0.5 mA cm^{-2} for a duration of 300 h.

Concerning SE, impurities in powder-based pellets, such as grain boundaries and voids, cause heterogeneous Li-plating and offer pathways allowing Li-dendrite penetration. Minimizing the impurity ratio, fabricating single-crystal or amorphous microstructured solid–electrolyte materials may effectively prevent dendrite formation and penetration. Kataoka et al. developed a solid-state battery system based on a garnet-type single-crystal solid–electrolyte ($Li_{6.5}La_3Zr_{1.5}Nb_{0.5}O_{12}$), $LiCoO_2$ cathode, and Li-metal anode.[124] The prepared batteries could be effectively recharged at a current density of 8.8 μA cm^{-2} at voltages between 3.1 and 4.0 V. In the CCD test, the prepared $Li/Li_{6.5}La_3Zr_{1.5}Nb_{0.5}O_{12}/Li$ symmetrical cells could withstand current densities up to 0.5 mA cm^{-2} without dendrite shorting. However, the authors did not test these batteries at higher current densities. Swamy et al. also investigated lithium-plating behavior on single-crystal garnet-based solid electrolytes ($Li_6La_3ZrTaO_{12}$).[125] Relatively high current densities (5 and 10 mA cm^{-2}) were applied, and the authors found clear dendrite formation during lithium plating. More research is therefore required for understanding Li-dendrite formation at these high currents in ASSB.

Thin-film based ASSB would be an alternative route to prevent dendrite formation. Thin films, fabricated by deposition techniques, are very homogeneous. In some cases, the prepared solid–electrolyte layers are amorphous in microstructure, enabling a homogeneous Li-ion flux due to the absence of grains and grain boundaries. Moreover, after the fabrication process, thin-film ASSB can operate without applying a stack pressure. It has been reported that thin-film Li-metal ASSB can be recharged up to thousands of cycles without severe capacity decay, partly because dendrite formation does not occur.[126] Obviously, there are new challenges in the thin-film ASSB field, such as reducing the production costs.

A common thought is that (electro)chemically stable inorganic-SE should be used for Li-metal ASSB. However, for stable Li/solid–electrolyte interfaces, it has recently been shown that small Li-dendrite tips can cause premature battery failure. Li-dendrite growth for an (electro)chemically stable interface is schematically shown in Figure 9e (top).[95] That leads to superior Li-plating at the dendrites' tips, where the electric field is higher than at the flat Li-metal surface. Due to the (electro)chemically stable interface, SE cannot consume Li-dendrites formed during battery operation. These properties can severely aggravate dendrite growth in SE, which eventually leads to battery short-circuiting.[95] In comparison to the chemically compatible concepts, unstable SE react with Li-metal to form an interlayer, which is schematically shown in Figure 9e (bottom). When Li-dendrites pierce through the formed interlayer and get exposed to the SE, they will be consumed. The reaction between Li-metal and SE can reduce the dendrite sharpness, suppressing the electrical field and allowing conformal Li-plating and Li-stripping. As a consequence, unstable SE can help to improve the cycle life and safety of ASSB. However, selecting appropriate SE to form a well-functioning interlayer remains a challenge, and further investigations are therefore necessary.

3.3. Lattice Mismatches

Lattice mismatches can be considered as physical contact problems from a microstructural point of view. Interfaces of this type frequently occur at the boundary between two solid materials with deviating lattice parameters. A lattice mismatch may occur at all electrode/electrolyte interfaces, causing strain and superlattice formation, leading to higher interfacial resistance. Figure 4c schematically depicts two interfaces: the left-hand side shows materials with the same crystal structure and similar lattice parameters, enabling fast Li-ion transport. The right-hand side shows materials with a large deviation in a lattice structure, resulting in more complex Li-ion pathways. Consequently, interfaces between materials with small lattice differences will display much lower interfacial resistances and higher ionic conductivities than in the case of highly deviating lattices. The latter is, unfortunately, the most-occurring scenario with materials currently used in ASSB. However, it should be noted that Li-ion transport through whole ASSB depends not only on the lattice structures at interface, but also on the interface impedance, bulk ionic conductivity and grain boundary diffusion properties of battery materials. In fact, slow Li-ion transport can also occur at the lattice-matched interfaces with poor bulk ionic conductivities.

Theoretical calculations assist in understanding the electronic and atomic distribution at the interfaces with lattice-mismatches. With density function theory (DFT) calculations, Jand and Kaghazchi modeled the interface structure between $LiCoO_2$ and cubic $Li_7La_3Zr_2O_{12}$ by considering different magnitudes of biaxial compressive and tensile strain.[127] Three energetically favorable interfaces were found from their simulations. Simulations for all three models revealed that lattice-mismatch results in the atomic rearrangement and high strain at the interface. Although ab initio molecular dynamics is not considered in this model, this modeling approach demonstrates that DFT methods can be successfully applied to simulate and predict the interfacial characteristics in ASSB. However, the prediction of the interfacial behavior in ASSB remains very complicated. Lattice-mismatch factors, low-symmetry features, thermodynamic metastable states, and elemental exchanges should also be taken into account.

Advanced computational methods with intelligent algorithms are required to search for energetically favorable interface structures. That gives a full picture of lattice-mismatch mechanisms. Gao et al. recently developed a prediction scheme to interpret the lattice-mismatch crystal structure of the interface by a so-called particle swarm optimization (CALYPSO) method in which lateral and vertical displacements were considered.[128] Combining the CALYPSO method with DFT calculations, six types of $LiCoO_2/Li_3PS_4$ interface structures were found, which are shown in **Figure 10**. Simulations revealed that the most energetically favorable interface involves the formation of cobalt sulfide and phosphorus oxide with both cation (Co and P) and anion (S and O) interdiffusion at the interface. These theoretical findings agree very well with the experimental results.[84]

One promising route to mitigate lattice differences is by utilizing high structural-similarity materials for both electrodes and SE. By using an all-phosphate electrode and electrolyte materials, Yu et al. fabricated a type of monolithic ASSB based
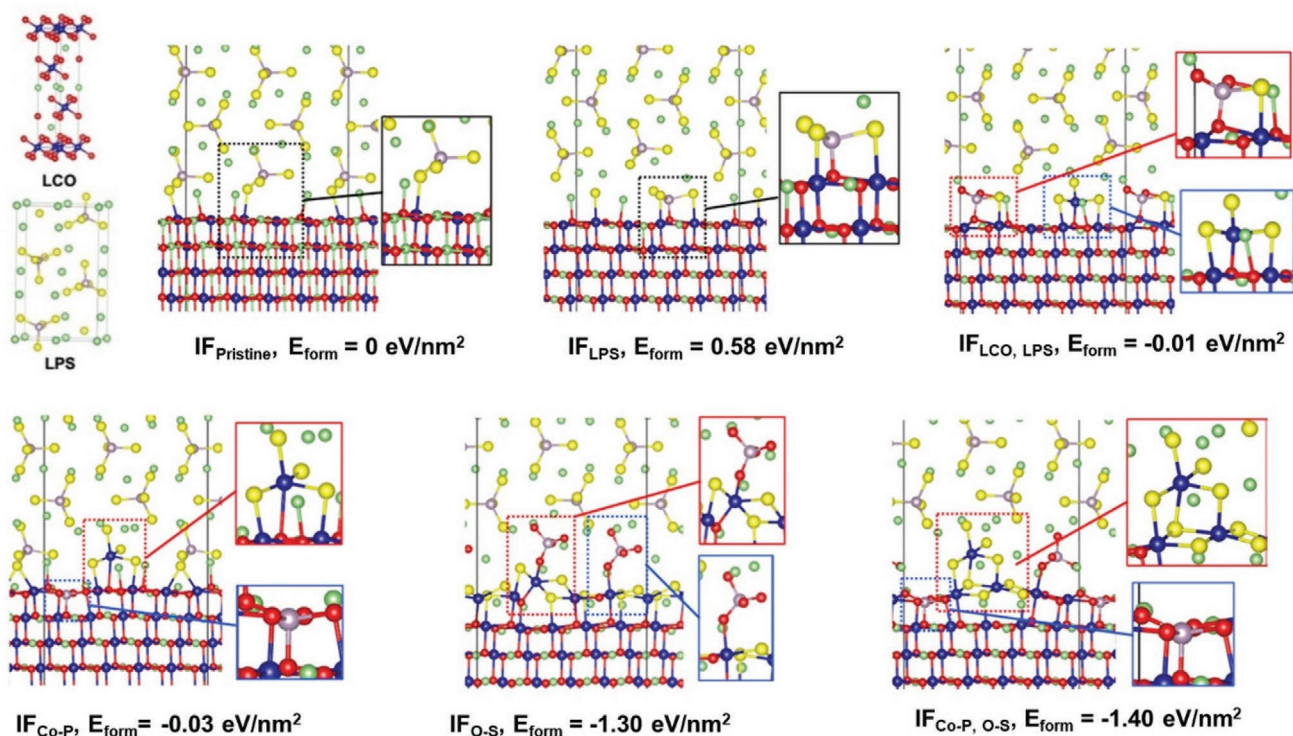
Figure 10. Predicted low-energy interface structures between LiCoO₂ and Li₃PS₄ for six different energy states. Reproduced with permission.[128] Copyright 2019, American Chemical Society.

on a $Li_3V_2(PO_4)_3$ cathode, a $Li_{1.3}Al_{0.3}Ti_{1.7}(PO_4)_3$ solid–electrolyte, and a $LiTi_2(PO_4)_3$ anode. The phosphate backbone with a similar lattice structure allows fast ionic transport between the different battery components.[129] Consequently, the prepared ASSB have a relatively low interfacial resistance and high electrode/electrolyte interface stability, delivering a capacity of 63.5 mAh g⁻¹ with 84% capacity retention after 500 cycles at 0.39C-rate. Li and colleagues developed a method to epitaxially embed electrode particles (0.54 Li_2TiO_3–0.46 $LiTiO_2$) into a $Li_{0.33}La_{0.56}TiO_3$ solid–electrolyte matrix as a composite electrode.[130] The authors firstly calcined the precursor materials at 500 °C to obtain solid–electrolyte powders. The amorphous solid–electrolyte powders were then mixed with 0.54 Li_2TiO_3–0.46 $LiTiO_2$ material, pressed into pellets, and sintered at 1250 °C. As a result, an epitaxial interface was formed between the electrode and solid–electrolyte, which has been demonstrated to mitigate the large lattice misfit.

3.4. Interdiffusion

Interdiffusion problems occur when material elements of two adjacent battery layers mutually diffuse into each other and generate an interlayer, as schematically shown in Figure 4d. The formation of such an interlayer often involves dissolution or decomposition of an electrode and solid–electrolyte materials, which may consequently lead to strong capacity decays and high interfacial resistances.

In the manufacturing process of ASSB, high-temperature synthesis (>600 °C) is often required to achieve well-crystallized structures, dense materials, and tight contact. However, it is frequently observed that high-temperature processing facilitates "cross-talk" between the electrode and solid–electrolyte, essentially leading to element exchange or interphase formation at the electrode/SE interface.[131,132] With combined thermal analysis strategies and first-principles calculations, Miara et al. studied the chemical compatibility between three high-voltage spinel cathode materials ($Li_2NiMn_3O_8$, $Li_2FeMn_3O_8$, and $LiCoMnO_4$) and two solid–electrolyte materials ($Li_{1.5}Al_{0.5}Ti_{1.5}(PO_4)_3$ and $Li_{6.6}La_3Zr_{1.6}Ta_{0.4}O_{12}$) materials during co-sintering.[133] The results indicated that the tested spinel cathodes are not compatible with $Li_{1.5}Al_{0.5}Ti_{1.5}(PO_4)_3$ and $Li_{6.6}La_3Zr_{1.6}Ta_{0.4}O_{12}$ when co-sintering temperatures are higher than 600 °C. At temperatures of 600 °C and higher, ionically insulating interphases start to form at the interface, leading to high interfacial impedances. Xu et al. studied the $LiMn_2O_4/Li_{0.33}La_{0.57}TiO_3$ interface. After co-sintering $LiMn_2O_4$–$Li_{0.33}La_{0.57}TiO_3$ pellets at 900 °C, a clear visible (Mn, La, and Ti) interdiffusive region of about 300 μm thick was observed across the $LiMn_2O_4/Li_{0.33}La_{0.57}TiO_3$ interface.[134] The interdiffusive layer formation was found to be independent of the co-sintering techniques, as the interphase formation was observed in both samples prepared by spark plasma sintering and conventional co-sintering methods. The induced interdiffusion interlayer caused a substantial increase of interfacial resistance, which increased approximately a factor 40 compared to the bulk $Li_{0.33}La_{0.57}TiO_3$.

Interdiffusion can also occur during battery operation. This phenomenon has been frequently observed in thin-film ASSB, for which high-temperature co-sintering processes during production are not required. Brazier et al. investigated the

**ADVANCED
SCIENCE NEWS**
www.advancedsciencenews.com

**ADVANCED
ENERGY
MATERIALS**
www.advenergymat.de

interface properties of microbatteries with a $LiCoO_2$ cathode, a $LiO_2–V_2O_5–SiO_2$ solid–electrolyte, and a SnO anode prepared by thin-film deposition techniques.[135] The fresh batteries showed no apparent element migration between different battery layers. After cycling the batteries for ten cycles at room temperature, it was found that Si and V migrated from the solid–electrolyte into the $LiCoO_2$ cathode. Reversely, Co from the cathode was detected in the solid–electrolyte. Similarly, Sakuda et al. studied the interfacial behavior in a $LiCoO_2/Li_2S–P_2S_5$/In solid-state battery and observed mutual diffusion of Co, P, and S at the interface between the cathode and solid–electrolyte after the very first charging cycle, as shown in **Figure 11**a.[84] The interdiffusion at the interface could be clearly suppressed, using a Li_2SiO_3 coating at $LiCoO_2$, which is demonstrated by the TEM observation in Figure 11b.[84] Apart from the cathode/solid–electrolyte interface, interdiffusion also occurs at the anode/solid–electrolyte interface. Figure 11c shows the cross-sectional TEM and EDX analysis of an as-deposited thin-film $LiCoO_2/Li_3PO_4$/Si battery at the Li_3PO_4/Si interface.[4] No interdiffusion of elements was observed in the initial state because a sharp boundary between the Si anode and the Li_3PO_4 solid–electrolyte is present.

However, as shown in Figure 11d, after the first lithiation of the Si anode, Si was found to migrate into the solid–electrolyte. Consequently, the capability of hosting Li-ions at the anode deteriorated as a result of active material loss.

Many experimental investigations have been performed to decrease the process temperatures to avoid interlayer formation caused by interdiffusion in bulk-type ASSB. However, limited progress has been achieved so far. Various methods have been investigated for preventing interdiffusion, of which cathode particle coatings or thin artificial buffer layers were demonstrated to be very promising. Kwak and Park discovered an unfavorable interdiffusional reaction at a $LiNi_{0.8}Co_{0.15}Al_{0.05}O_2/75Li_2S–22P_2S_5–3Li_2SO_4$ interface.[136] S and P were diffused from the solid–electrolyte into the cathode, causing high interfacial resistance. It was demonstrated that a $LiInO_2$ and $LiInO_2–LiI$ coating on the cathode particles could successfully prevent interdiffusion and reduce the interfacial impedance.

Experimentally searching for optimal coating candidates is usually a time-consuming and low throughput process. In this regard, intelligent computational algorithms can be far more efficient. For example, Xiao et al. employed high-throughput
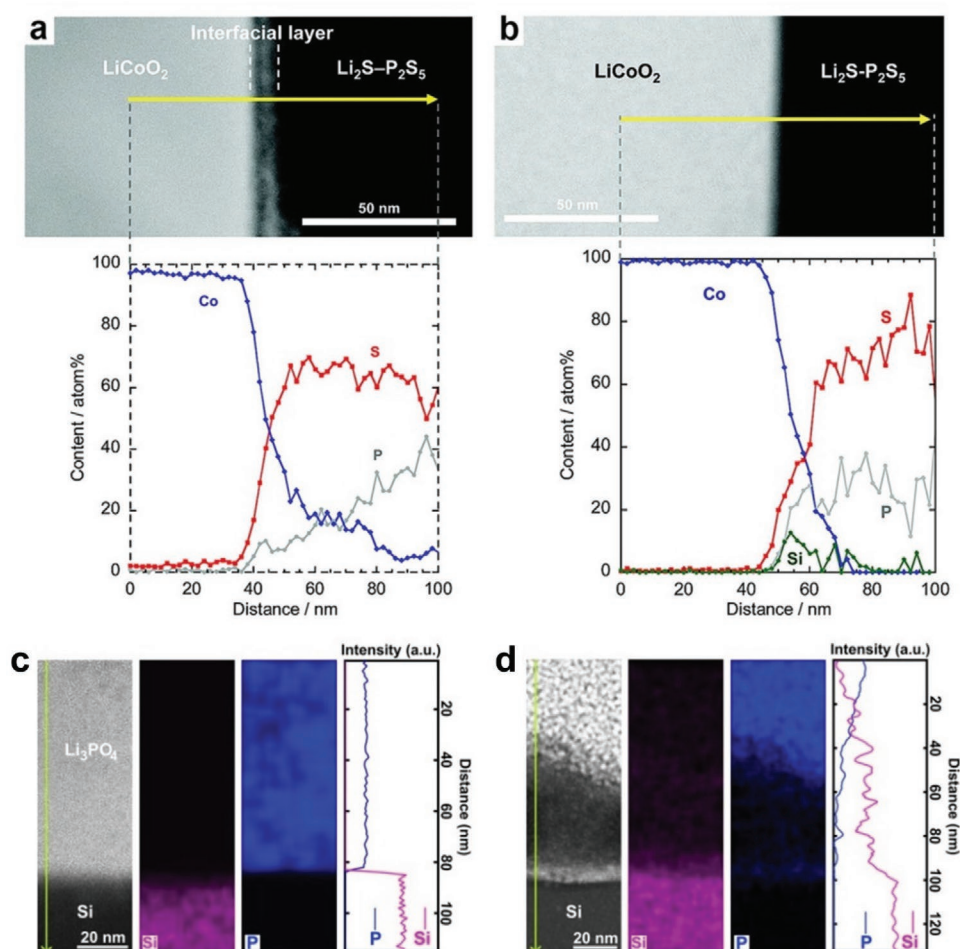
Figure 11. SEM (top) and XPS (bottom) measurement of interdiffusion layers formed at the $LiCoO_2/Li_2S–P_2S_5$ interface a) and Li_2SiO_3 protection effect suppressing interdiffusion b). Cross-sectional TEM and EDX analysis at the Si/Li_3PO_4 interface at a pristine state c) and first lithiation state d).[4] a,b) Reproduced with permission.[84] Copyright 2009, American Chemical Society. c,d) Reproduced with permission.[4] Copyright 2018, Wiley-VCH.

computation to search for excellent coating materials for cathodes in ASSB.[137] In the initial search iteration, 104 082 Li-containing inorganic materials were considered. With progressive screening criteria, such as excluding radioactive elements and electronically conductive materials, phase stability, electrochemical stability, chemical stability, down-selection to polyanionic oxides, and ionic–electronic considerations, three appealing cathode-coating candidates were found: LiH_2PO_4, $LiTi_2(PO_4)_3$, and $LiPO_3$. An experimental investigation is further necessary to demonstrate and prove this concept. Depositing thin artificial buffer layers is also widely reported, which are more often adopted for thin-film ASSB, using easily accessible deposition tools. Many materials have been developed as buffer candidates are summarized in **Table 2**.

3.5. Space-Charge Layers

Space-charge layers (Figure 4e) are formed when two materials with different (electro)chemical potentials are brought in contact. At the same time, only one charged species, either an ion or electron, can move. That will create an interfacial region where charge builds up, forming a so-called space-charge layer.[138] At present, the influence of space-charge layers on the battery performance is not well understood. In some cases, the space-charge layers are beneficial. Maier found that space-charge layers can enhance the ionic conductivity at interfaces, which was concluded from theoretical calculations of dispersed Al_2O_3 or silica in ionic conductors.[139] However, in most cases, the presence of space-charge layers is reported to be unfavorable. Haruyama et al. theoretically elucidated the space-charge effect at the $LiCoO_2/Li_3PS_4$ interface by density functional simulations. Their results suggested that Li-ion adsorption occurs at the interface, which leads to a deformed interface and higher interfacial resistance.[88] Takada et al. revealed that space-charge layers could increase the interfacial resistance between the $LiMn_2O_4$ cathode and a sulfide-based solid–electrolyte ($Li_{3.25}Ge_{0.25}P_{0.75}S_4$).[140] Recently, it has also been found that space-charge layer effect is negligible under some circumstances. de Klerk et al. theoretically calculated the thickness of the space-charge-layer to be about 1 nm. However, it was reported that the induced resistance for such thin space-charge layers is negligible, except for the case when the solid–electrolyte has become lithium-depleted.[138] Experimental investigations performed by Haruta et al. confirmed that the space-charge layer effect is negligible at the $LiCoO_2/LiPON$ interface in thin-film batteries.[141] The measured interfacial resistance was reported to be as low as 8.6 Ω cm^2, which is even smaller than in batteries using liquid electrolytes. However, the same authors noted that the sputtering parameters of LiPON have a significant influence on the interfacial resistance. The interfacial damage caused by sputtering was the primary source of the increasing interfacial resistance. When sputter-depositing LiPON on $LiCoO_2$, the second phase of $LiNO_2$ impurity may be formed at the interface.[142] Postannealing can help to remove this unfavorable impurity. Unfortunately, high-temperature-annealing conditions cause side reactions between $LiCoO_2$ and LiPON, creating Co_3O_4 and Li_3PO_4 at the interface, leading to space-charge layer formation.

Several strategies have been reported to mitigate the negative effect that resulted from the formation of space-charge layers. The most commonly used approach is using a buffer layer between the electrode and solid–electrolyte. Takada et al. deposited $LiTaO_3$, $LiNbO_3$, and $Li_4Ti_5O_{12}$ between $LiCoO_2$ and $Li_{3.25}Ge_{0.25}P_{0.75}S_4$. They found that $LiTaO_3$ and $LiNbO_3$ show a more pronounced effect in reducing the interfacial resistance than $Li_4Ti_5O_{12}$.[143] In another paper, the same group also reported that $LiNbO_3$ could be used as a buffer between $LiMn_2O_4$ and $Li_{3.25}Ge_{0.25}P_{0.75}S_4$, suppressing the space-charge layer formation.[140] Yada et al. developed a lithium–niobium–tantalum oxide material for the cathode/solid–electrolyte interface, which is well-suited for high-voltage (5 V) ASSB.[144] The authors claimed that this type of interlayer could avoid space-charge layer formation due to the high dielectric permittivity of the used buffer materials, leading to thinner space-charge layers.

From the above discussions (Sections 3.1 to 3.5), it can be seen that introducing an artificial buffer layer between the electrodes and electrolytes is a very versatile approach to mitigate interfacial problems in ASSB. At present, many materials have been adopted as buffer-layers in ASSB. A compilation of these materials is shown in Table 2.[66,84,114,115,116,118–121,140,145–164]

3.6. Li-Immobilization Interlayers

When (electro)chemical side reactions occur at interfaces, interlayers will be formed. As schematically shown in Figure 4f, in some cases, the interlayer formation immobilizes moveable Li-ions from the electrodes. That directly leads to storage capacity losses. Such a Li-immobilization interlayer has not been widely reported, possibly because only a few characterization techniques can detect the lithium concentration within thin battery layers with high-depth resolution. Chen et al. deposited and cycled thin-film $Si/Li_3PO_4/LiCoO_2$ batteries and found severe capacity decay in the initial cycles.[4] Using operando neutron depth profiling (NDP), the authors visualized the formation of a Li-immobilization interlayer at the Si/Li_3PO_4 interface. It was reported that Si migrates into Li_3PO_4 to form a Li–Si–P–O solid–electrolyte layer at the interface. Regrettably, the formation of such an interlayer involves immobilizing mobile lithium-ions, which are therefore no longer available for cycling. The growth of these interlayers was found to occur only during the lithiation process of the Si anode, i.e., during the charging of the battery. The same authors presented a detailed model to describe this interlayer formation process.[4] Strikingly, the Li-immobilization interlayer seems not to influence the Li-ion transportation kinetics. That is because the conduction of Li_3PO_4 is happening through Li-ion hopping mechanism.[165–167] When there are more Li-ion sites available in the solid–electrolyte, it can, in principle, improve the Li-ion conduction kinetics. It has been reported that the Si-doped Li_3PO_4 ($Li_2O–SiO_2–P_2O_5$) SE has a Li-ion conductivity of about 10^{-6} S cm^{-1}, which is about two orders of magnitude higher than pure Li_3PO_4.[159,168]

In the study of Chen et al.,[4] the $LiCoO_2/Li_3PO_4$ interface shows no degradation during battery cycling. In another study, Wang et al. used LiPON as a solid–electrolyte. They investigated

Table 2. Various buffer layer materials applied to ASSB.

Material	Deposition method	Thickness [nm]	Purpose	Buffered interface	Ref.
Mg	Magnetron sputtering	5, 10, and 100	Wetting issue Dendrite issue	$Li/Li_7La_3Zr_2O_{12}$	[115]
Al	EBE	20	Wetting issue Dendrite issue	$Li/Li_7La_{2.75}Ca_{0.25}Zr_{1.75}Nb_{0.25}O_{12}$	[116]
Si	PECVD	10	Wetting issue Dendrite issue	$Li/Li_{6.85}La_{2.9}Ca_{0.1}Zr_{1.75}Nb_{0.25}O_{12}$	[118]
Ge	EBE	20	Wetting issue Dendrite issue	$Li/Li_{6.85}La_{2.9}Ca_{0.1}Zr_{1.75}Nb_{0.25}O_{12}$	[145]
	Magnetron sputtering	60	Chemical stability	$Li/Li_{1.5}Al_{0.5}Ge_{0.5}P_3O_{12}$	[146]
Nb	Magnetron sputtering	10	Interdiffusion Space charge	$Li_7La_3Zr_2O_{12}/LiCoO_2$	[147]
Bi	Magnetron sputtering	20	Wetting issue Chemical stability	$Li/Li_{1.5}Al_{0.5}Ge_{0.5}P_3O_{12}$	[119]
Sn	Magnetron sputtering	10	Interdiffusion Wetting issue Dendrite issue	$Li/Li_{6.375}La_3Zr_{1.375}Nb_{0.625}O_{12}$	[148]
Au	Magnetron sputtering	20	Wetting issue Dendrite issue	$Li/Li_{6.6}La_3Zr_{1.6}Ta_{0.3}O_{12}$	[66]
	Magnetron sputtering	20	Wetting issue Dendrite issue	$Li/Li_{6.28}Al_{0.24}La_3Zr_2O_{12}$	[149]
Graphite	Thermal evaporation	150	Wetting issue Dendrite issue	$Li/Li_{6.28}Al_{0.24}La_3Zr_2O_{12}$	[150]
Diamond-like carbon	CVD	4.3	Chemical stability Interdiffusion	$Li_2S–P_2S_5/LiNi_{0.8}Co_{0.15}Al_{0.05}O_2$	[151]
Al_2O_3	ALD	20	Interdiffusion	$Li_{3.15}Ge_{0.15}P_{0.85}S_4/LiCoO_2$	[152]
	ALD	5–6	Wetting issue Dendrite issue	$Li/Li_7La_{2.75}Ca_{0.25}Zr_{1.75}Nb_{0.25}O_{12}$	[114]
	ALD	15	Interdiffusion Chemical stability	$Li/Li_{1.3}Al_{0.3}Ti_{1.7}(PO_4)_3$	[153]
ZnO	ALD	30–50	Wetting issue Dendrite issue	$Li/Li_{6.75}La_{2.75}Ca_{0.25}Zr_{1.75}Nb_{0.25}O_{12}$	[120]
ZrO_2	Sol–gel method	10	Contact issue	$Li_3PS_4/LiNi_{1/3}Co_{1/3}Mn_{1/3}O_2$	[154]
Li_3N	EBE	Not given	Wetting issue Dendrite issue	$Li/Li_{6.5}La_3Zr_{1.5}Ta_{0.5}O_{12}$	[155]
Li_3PO_4	PLD	100	Chemical stability	$Li_2S–P_2S_5/LiNi_{0.5}Mn_{1.5}O_4$	[144]
LiPON	Magnetron sputtering	500	Dendrite issue	$Li/Li_{1.5}Al_{0.5}Ge_{1.5}(PO_4)$	[109]
Li_2SiO_3	Sol–gel method	10	Interdifussion	$Li_2S–P_2S_5/LiCoO_2$	[84]
	So–gel method	500	Chemical stability	$Li_{6.28}La_3Zr_2Al_{0.24}O_{12}/$ $LiNi_{0.33}Mn_{0.33}Co_{0.33}O_2$	[157]
$Li_4SiO_4–Li_3PO_4$	PLD	1000	Contact issue	$Li_2S–P_2S_5/LiCoO_2$	[158]
$Li_{3.5}Si_{0.5}P_{0.5}O_4$	PLD	45	Contact issue	$Li_2S–P_2S_5/LiCoO_2$	[159]
$LiNbO_3$	PLD	2.4	Space charge	$LiPON/LiCoO_2$	[160]
	Spray coating	20	Space charge	$Li_{3.25}Ge_{0.25}P_{0.75}S_4/LiMn_2O_4$	[140]
	PLD	5	Space charge	$Li_2S–P_2S_5/LiCoO_2$	[143]
Li_3NbO_4	ALD	0.5	Chemical stability	$Li_{10}SnP_2S_{12}/LiCoO_2$	[161]
$LiTaO_3$	Sol–gel method	20	Interdiffusion	$Li_2S–P_2S_5/LiCoO_2$	[143]
$Li_4Ti_5O_{12}$	PLD	5	Space charge	$Li_2S–P_2S_5/LiCoO_2$	[143]
	Spray-coating	5	Space charge	$Li_{3.25}Ge_{0.25}P_{0.75}S_4/LiCoO_2$	[162]
	Spray-coating	5	Space charge	$Li_2S–P_2S_5/LiNi_{0.8}Co_{0.15}Al_{0.05}O_2$	[163]
$Li_{2.3}La_{2.1}Ta_{1.2}O_{15.3}$	Magnetron sputtering	100	Contact issue	$Li_5La_3Ta_2O_{12}/LiCoO_2$	[164]

**ADVANCED
SCIENCE NEWS**

www.advancedsciencenews.com

**ADVANCED
ENERGY
MATERIALS**

www.advenergymat.de

the interface performance of thin-film $Si/LiPON/LiCoO_2$ batteries via in situ EELS.[85] Interestingly, the authors found a disordered interlayer at the interface between $LiCoO_2$ and LiPON. The deposition of LiPON possibly causes the disordered interlayer in an N_2-assisted Ar atmosphere, which is more detrimental than the deposition of Li_3PO_4 on a predeposited $LiCoO_2$ surface under pure Ar. During cycling, lithium will be accumulated in the disordered interlayer, forming Li_2O and Li_2O_2. Because Li-the immobilization interlayer has a Li_2O-based chemistry, which is less conductive than LiPON, the rate performance of such a solid-state battery will degrade. From the above discussion, it can be concluded that the Li-immobilization interlayer formation is determined by (electro)chemical reaction at the interface, which can be influenced by the material chemistries and synthesis parameters. In Section 4, we will review the interface-sensitive or depth-resolved characterization tools applicable to interface studies in ASSB. Among them, some of the discussed techniques can detect Li-signal for the Li-immobilization interlayer investigations. We believe this information will offer new perspectives in investigating the Li-immobilization phenomena in ASSB in the future.

3.7. Thermal Issues

LBB containing LE are prone to thermal issues. A battery management system, including the thermal management system, is therefore necessary to accurately control battery temperature and other states.[74,169,170] To reduce thermal issues, LE can be replaced by SE. However, thermal runaway can still befall to ASSB, as schematically shown in Figure 4g. An interesting experimental comparison between the thermal stability of a half-cell with a liquid electrolyte and a half-cell with a solid polymer electrolyte (SPE) has been performed by Perea et al.,[171] showing that the thermal stability of a solid electrolyte is superior to that of a liquid electrolyte. At a state-of-charge (SoC) of 100% an onset temperature—the temperature at which exothermic reactions start—of 90 °C in comparison to 247 °C was found for the liquid versus the solid variant, respectively. Moreover, the self-heat rate for the liquid system was determined to be 3.2 °C min^{-1} in contrast to 0.11 °C min^{-1} for the solid polymer system.

Chung and Kang[172] indicated that the interlayer between $Li_{1.5}Al_{0.5}Ge_{1.5}(PO_4)_3$ and Li metal has a strong influence on the thermal stability. It has been found that the interphase decomposes at temperatures higher than 200 °C and subsequently delivers oxygen for reacting with Li metal. Chen et al.[75] investigated the thermal performance of four types of SE ($Li_{1.5}Al_{0.5}Ge_{1.5}(PO_4)_3$, $Li_{1.4}Al_{0.4}Ti_{1.6}(PO_4)_3$, $Li_{3x}La_{2/3-x}TiO_3$, and $Li_{6.4}La_3Zr_{1.4}Ta_{0.6}O_{12}$) with metallic Li. It was found that thermal runaway occurred in the $Li_{1.5}Al_{0.5}Ge_{1.5}(PO_4)_3$–, $Li_{1.4}Al_{0.4}Ti_{1.6}(PO_4)_3$–, and $Li_{3x}La_{2/3-x}TiO_3$-materials, while no obvious heat generation was found with $Li_{6.4}La_3Zr_{1.4}Ta_{0.6}O_{12}$ in contact with Li metal. In addition, the authors concluded that oxygen release from the SE trigger highly exothermic reactions with Li metal, leading to thermal runaway. It should be noted that the onset temperature for the samples going into thermal runaway was always measured to be larger than 250 °C.

Sintering of SE and co-sintering of composites is often necessary to achieve dense materials for increasing the conductivity. (Co)sintering methods can lead to the formation of interlayers with a high resistance. This has been shown by Gellert et al.,[173] who experimentally investigated the compatibility of $Li_{1.5}Al_{0.5}Ti_{1.5}(PO_4)_3$ with various typical cathode materials. It was found that oxide cathode materials all form electrochemically inactive and ionically blocking phases at temperatures as low as 500 °C, while $Li_{1.5}Al_{0.5}Ti_{1.5}(PO_4)_3$ was found to be much more stable with phosphate-based cathode materials. It can be concluded that phosphate-based cathode materials are thus more favorable in combination with $Li_{1.5}Al_{0.5}Ti_{1.5}(PO_4)_3$ than other cathode materials, from a thermal point of view, and therefore, also for a production point of view.

Essentially, these studies show that also ASSB are not intrinsically safe from a thermal point of view and therefore this topic deserves more attention. In various recent review papers,[174–176] the thermal performance of SE is discussed, indeed indicating that inorganic SE exhibit the highest safety level of which oxides-based SE show the best thermal stability. It also should be noted that, in general, the onset temperature of individual components lies higher in comparison to the mixed components, such as SE with electrode material.[174]

3.8. Current-Collector/Electrode Interfaces

While the electrode/solid–electrolyte interface properties affect the kinetics of internal Li-ion transport, only a little attention has been paid to the CC/electrode interface. The electronic conductivity of the external circuit also strongly influences the quality of the CC/electrode interface. Like the electrode/solid–electrolyte interface, the (electro)chemical stability of the CC/electrode interface should be well-considered before producing ASSB. The electrochemical stability windows of the CC should be compatible with the voltage range of the electrodes. Moreover, the physical contact between the electrode material and CC is another concern.

Nara and co-workers systemically investigated the interfacial resistance between the $LiCoO_2$ cathodes and the aluminum CC by altering the pressing pressure, with or without carbon undercoating layers.[177] The authors observed through asdenoted scanning spread resistance microscope that the high interfacial resistance between the $LiCoO_2$ cathode and bare aluminum CC under low pressing pressure is attributed to the poor contact at the interface. Applying a high pressure and a carbon coating between cathode and CC effectively decreases the contact resistance.

Varying the surface properties of CC will significantly change the cycling performance of batteries. Wu et al. employed three kinds of Al current collectors, including smooth unetched Al-foil (unetched-Al), anodization-etched Al foil either with carbon coating (etched-Al-C) and without carbon coating (etched-Al), for supporting LFP cathode material.[178] The batteries prepared with the etched-Al-foil current collector with carbon coating showed a lower resistance and better cycling capacity than those with the other current collectors. The authors attributed the improvement to the absence of an insulating surface layer on the Al-foil and the improved adhesion at the active layer/CC interface. In another contribution, Wu et al. investigated this concept further with a $Li_4Ti_5O_{12}$ anode.[179] Apart

from the unetched-Al, etched-Al, and etched-Al-C current collectors, Cu-foil (Cu) and Cu-foil with carbon coating (Cu-C) were added for performance comparison. It was revealed that the interfacial resistance between $Li_4Ti_5O_{12}$ and CC follows the order Cu-C<etched-Al-C-Cu<etched-Al<unetched-Al. Interestingly, the delivered capacity of $Li_4Ti_5O_{12}$ electrodes with these current collectors was also found to be in this order. Kim et al. suggested that the Cu-foil by growing a conformal graphene layer was more hydrophobic, facilitating the adhesion with the electrodes.[180]

3.9. Interfacial Issues of All-Solid-State Lithium–Sulfur Batteries

Because Li–S batteries are considered to be very promising energy storage systems, we have chosen to shed some light on these systems as well. Despite of advantages, such as the relatively high specific capacity of 1675 mAh g^{-1}, energy density of 2600 or 2800 Wh L^{-1}, natural abundance, cost effectiveness, and environmental friendliness of S,[181] conventional Li–S batteries with LE are also facing challenges. These challenges can be found in the insulating nature and large volume change of the S cathode, SEI formation, and Li-dendrite growth. However, without doubt, the most notorious issue is the dissolution and "shuttle effect" of polysulfides, which causes loss of active electrode materials, internal resistance increase, and low columbic efficiency.[182] Replacing LE with SE can simply address the polysulfide dissolution and shuttling since the polysulfide species cannot migrate/diffuse through SE. However, all-solid-state Li–S batteries suffer from other issues, of which the interfacial issues at the electrode/solid–electrolyte interfaces are most notorious.

Volume change up to 80% causes poor physical contact at the cathode/solid–electrolyte interface. This high volume change can lead to high mechanical stress, cracks, or even pulverization of the S particles, resulting in a large interfacial resistance. To reduce the interfacial resistance at the cathode/solid–electrolyte interface, various types of new cathode materials have been reported. For example, Zhang et al. deposited nanosized S on carbon nanotubes (CNT) by a liquid method to synthesize a novel CNT@S composite as the active material.[183] The CNT@S composite was further mixed with conducting $Li_{10}GeP_2S_{12}$ and acetylene black by ball milling to prepare a cathode composite. When employed in a solid-state battery with a Li-foil anode and a bilayer solid–electrolyte consisting of $Li_{10}GeP_2S_{12}$ and Li_2S–P_2S_5–P_2O_5, the CNT@S cathode was able to deliver reversible capacities of 1193, 959, 813, 569, and 395 mAh g^{-1} at 0.1, 0.5, 1, 2, and 5C-rate, respectively, at 60 °C. Tao et al. reported a facile synthesis of an S–$Li_7La_3Zr_2O_{12}$–C cathode material by sol–gel and thermal diffusion method.[184] The assembled ASSB with S–$Li_7La_3Zr_2O_{12}$–C cathode, $Li_7La_3Zr_2O_{12}$–PEO–$LiClO_4$ solid–electrolyte, and Li-metal anode, exhibited remarkable performance, delivering an attractive specific capacity of 900, 1210, and 1556 mAh g^{-1} at 37, 50, and 70 °C, receptively.

Li_2S is another promising cathode candidate for all-solid-state Li–S batteries. Li_2S has a theoretical specific capacity of 1166 mAh g^{-1}, which is also relatively high. Moreover, the Li_2S cathode can be coupled with Li-free anodes, free from the Li-dendrite formation. Yu et al. assessed the Li-ion transport between a Li_2S cathode and Li_6PS_5Cl solid–electrolyte, and found the interfacial conductivity is strongly dependent on the preparation method.[185] It was revealed that the solid-state Li–S batteries using ball-milled Li_2S(nanosized)–Li_6PS_5Cl cathode showed a much lower interfacial impedance than the batteries with unmilled Li_2S(microsized)–Li_6PS_5Cl and Li_2S(nanosized)–Li_6PS_5Cl cathode materials. Han and co-workers developed a method to confine nanosized Li_2S and Li_6PS_5Cl into a nanoscale carbon matrix as composite cathode.[186] The Li_2S–Li_6PS_5Cl–C composite was then put on the top of $80Li_2S$–$20P_2S_5$ solid–electrolyte powders and co-pressed. For preparing the full all-solid-state Li–S battery, an In-metal electrode was attached on the other side of the $80Li_2S$–$20P_2S_5$ layer. The assembled full Li–S battery could deliver a large reversible capacity of 830 mAh g^{-1} after 60 cycles at a current density of 50 mA g^{-1}. Apart from S and Li_2S, transition-metal sulfides, such as TiS_3,[187] FeS,[188] CoS_2,[189] NiS,[190] CuS,[191] and MoS_2,[192] were also reported as cathode materials for all-solid-state Li–S batteries. These materials showed better conductive properties, which facilitates to establish a low-resistance at the cathode/solid–electrolyte interface.[193]

Compared with the cathode/solid–electrolyte interface, it is essential to consider the dendrite formation and (electro)chemical stability issues at the Li/solid–electrolyte interface for all-solid-state Li–S batteries. With respect to the Li-dendrite formation and tackling strategies, all-solid-state Li–S batteries are very similar to other battery systems. The authors kindly refer the readers to Section 3.2 for that discussion. In order to reduce the reducibility of Li-metal in contacting solid–electrolyte, a variety of Li-alloys have been developed as novel anode materials, including Li–In,[194] Li–Sn,[195] Li–Al,[196] and Li–Mg.[197] For instance, Hayashi et al. successfully prepared an all-solid-state Li–S battery using CuS mixed S as a cathode, Li_2S–P_2S_5 as solid–electrolyte, and Li–In alloy as an anode. The synthesized all-solid-state battery could retain a large capacity over 650 mAh g^{-1} after 20 cycles at a current rate of 64 μA cm^{-2}. It is also possible to use a Li-free anode when constructing all-solid-state Li–S batteries with Li_2S cathodes. For example, Xu et al. reported an all-solid-state Li–S battery based on Li_2S–graphene cathode, $Li_7P_3S_{11}$-coated Si anode, and $Li_7P_3S_{11}$ solid–electrolyte.[198] In such a configuration the interfacial reaction between Li-metal and $Li_7P_3S_{11}$ and dendrite-induced safety concerns are avoided. As a result, the synthesized battery was able to deliver a reversible capacity of >200 mAh g^{-1} at a current rate of 50 mA g^{-1} at room temperature.

Recently, SPE are becoming very popular to be used as SE for all-solid-state Li–S batteries. SPE have much better process-ability and flexibility in comparison to the inorganic-SE, with which intimate contact can be easily constructed. Furthermore, SPE are much lighter than most inorganic-SE, which allows a high energy density to be readily achieved for the SPE-based Li–S batteries. However, it was found that the Li–S batteries using some common SPE such as PEO–LiTFSI, PEO–$LiCF_3SO_3$, and PEO–$LiClO_4$, showed limited capacity even in initial cycles, along with the presence of polysulfide shuttling effect.[199–201] This has been attributed to the inferior quality of the SEI layer formed on the Li-metal anode. A proper selection of Li-salts in SPE is of paramount importance to build a stable interface between SPE and Li-metal for all-solid-state Li–S batteries. For a decade now, some new Li-salts have been reported,

including lithium bis(fluorosulfonyl)imide (LiFSI),[199] lithium (fluorosulfonyl)(trifluoromethanesulfonyl)imide (LiFTFSI),[200] Li (difluoromethanesulfonyl)(trifluoromethanesulfonyl)imide (LiDFTFSI),[202] and Li tricyanomethanide (LiTCM).[203] In contrast to the widely used LiTFSI, these newly developed Li-salts have been demonstrated to be capable of improving the interfacial stability against Li-metal anode. For example, Judez et al. studied the cycling performance of the all-solid-state Li–S battery using PEO–LiFSI electrolyte, PEO–LiFSI–carbon mixed S cathode, and Li-metal anode.[199] The reversible capacity of the prepared LiFSI-based Li–S battery can maintain at 600 mAh g^{-1} after 50 cycles at 0.1C-rate with 40 wt% S content. Further study in finding appropriate Li-salts is still necessary.

4. Interface-Sensitive Techniques

Interfaces in ASSB, such as the electrode/solid–electrolyte or the CC/electrode interfaces, are buried under multiple layers, such as the current-collectors and packaging parts. For that reason, these interfaces are inaccessible by conventional analytical tools. In fact, the capacity decay during cycling is often associated with degradation at these interface(s). Therefore, probing the interface(s) and understanding their degradation mechanisms are essential in the characterizations of ASSB. This section is devoted to interface-sensitive and depth-resolved techniques applicable to ASSB.

At the beginning of this section, some recent works presenting etching-based depth profiling techniques to study the interfaces in ASSB will be reviewed. That includes sputter etched X-ray photoelectron spectroscopy (XPS), time of flight secondary ion mass spectroscopy (ToF-SIMS), auger electron spectroscopy (AES), scanning auger microscopy (SAM), glow discharge optical emission spectrometry (GD-OES), laser ablation inductively coupled plasma mass spectrometry (LA–ICP–MS), and laser-induced breakdown spectroscopy (LIBS). Most of these techniques are based on sputter etching with ions or pulsed laser to collect layer-by-layer information. They are therefore destructive to the samples and inapplicable to operando or in situ studies. This drawback is overcome in ion beam analysis (IBA) depth profiling techniques, such as Rutherford backscattering spectroscopy (RBS), elastic recoil detection analysis (ERDA), nuclear reaction analysis (NRA), particle-induced gamma emission (PIGE), and particle-induced X-ray emission (PIXE). It is followed by a subsection on the applications of TEM techniques, including EELS and electron holography (EH). TEM techniques typically require the sample to be no thicker than 100 nm, and for that reason, thin-film ASSB are the perfect candidates. For bulk type ASSB, the high penetration power of synchrotron X-ray offers an unobstructed view of the buried interface. We shall review various studies presenting X-ray absorption spectroscopy (XAS), synchrotron XPS, interface X-ray scattering, and X-ray imaging. The main limitation of synchrotron X-ray methods is their low sensitivity to light elements such as lithium. Neutron based methods overcome this as they are based on interaction with atomic nuclei rather than with electrons. The last subsection covers two interface-sensitive neutron techniques applicable to ASSB, namely neutron reflectometry (NR) and NDP.
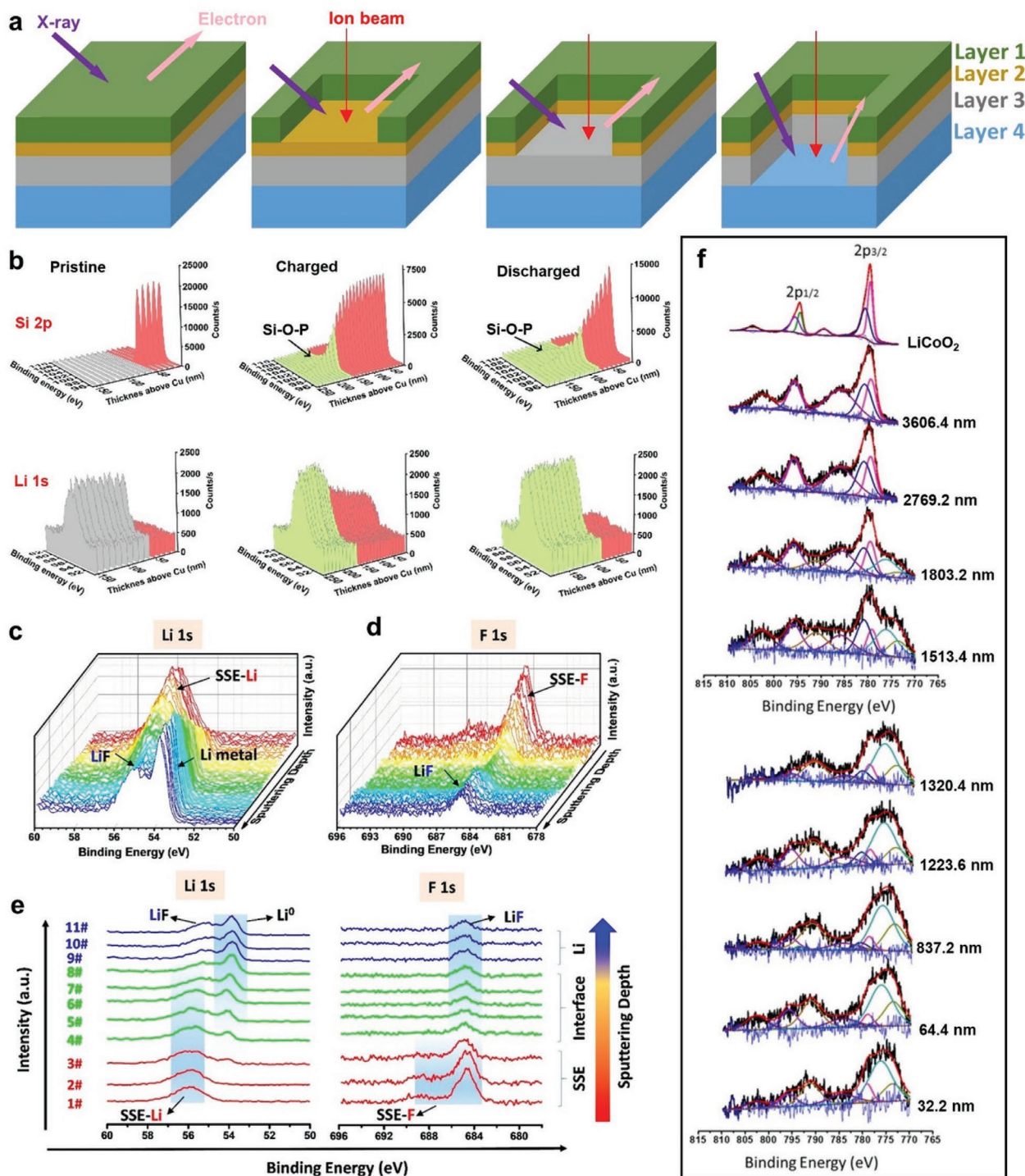
4.1. Etching-Based Depth Profiling Techniques

Techniques in this group are based on collecting spectroscopic signals during or after the etching of the sample. The etching beam can be ions (XPS, ToF-SIMS, AES, SAM, and GD-OES) or pulsed laser (LA–ICP–MS and LIBS). Because these etching beams are destructive to the samples, they are typically used for postmortem analysis. All these techniques can offer depth profiling of various elements, including lithium, which is essential for the interface characterization of ASSB.

4.1.1. X-Ray Photoelectron Spectroscopy

XPS is a surface-sensitive spectroscopic technique based on the photoelectric effect.[204] It involves irradiating the sample with a monochromatic X-ray and measuring the emitted electron population spectra. The detected binding energy of the electrons is characteristic of the elemental composition of the sample and the chemical state. The high energy resolution of the spectrometer, on the order of 0.1 eV, allows for accurate determination of the chemical shift in the electron binding energies. All elements except for hydrogen and helium are detectable by XPS. Depth profiling with XPS is achieved when this technique is coupled with an ion beam sputtering or etching source. As illustrated schematically in **Figure 12**a, an ion gun is used to etch the sample surface for a period of time. Each etching cycle exposes a new surface in the depth direction, then XPS spectrum is collected. A sequence of etching and XPS measuring processes are combined to compile the XPS depth profile.[205–207] XPS measurements can be performed both in laboratories and at synchrotron sources, each with its own (dis)advantages. This subsection covers ASSB researches using lab-based XPS. Those using synchrotron XPS will be discussed later.

The interfacial interaction between the electrode and the solid–electrolyte significantly affects the performance of an ASSB. Interdiffusion of the atoms at the electrode/solid–electrolyte interface has been frequently observed. Such phenomena have attracted much attention because an unstable interface destabilizes the whole ASSB and may lead to capacity deterioration. With XPS depth profiling, Chen et al. revealed the mechanism of Si migration at the Si/Li$_3$PO$_4$ interface.[4] Si 2p and Li 1s spectra were extracted from batteries under pristine, fully charged, and fully discharged conditions. As illustrated in Figure 12b, the sharp interface between Si and Li$_3$PO$_4$ in the pristine battery disappeared after the lithiation and delithiation processes. The additional peaks at the Si/Li$_3$PO$_4$ interface denoted Si–O–P, suggest the formation of an interlayer. The interlayer immobilizes moveable Li-ions, resulting in capacity decay in the battery. More importantly, the discovery of this detrimental interlayer calls for additional efforts on barrier layer construction at the electrode/solid–electrolyte interface.

Li-metal is considered as one of the most promising anode candidates for ASSB due to its high specific energy density. However, its application is hindered by the dendrite formation and their high reactivity with the SE. XPS depth profiling is a versatile tool for investigating the interfacial phenomena at the

2003939 (21 of 55)

**ADVANCED
SCIENCE NEWS**

www.advancedsciencenews.com

**ADVANCED
ENERGY
MATERIALS**

www.advenergymat.de

Figure 12. Schematic illustration of sputter-etched XPS measurement for layered samples a). Si, Li spectra at the Si/Li$_3$PO$_4$ interface for pristine, fully charged, and fully discharged Si/Li$_3$PO$_4$/LiCoO$_2$ ASSB. Signals from the Si and Li$_3$PO$_4$ layer are respectively shown in red and gray. The newly formed interlayer is shown in green b). Li and F spectra of the Li/Li$_6$PS$_5$Cl$_{0.3}$F$_{0.7}$ interface c–e). Co spectra of the Li$_7$La$_3$Zr$_2$O$_{12}$/LiCoO$_2$ interface f). b) Reproduced with permission.[4] Copyright 2018, Wiley-VCH. c–e) Reproduced with permission.[208] Copyright 2020, American Chemical Society. f) Reproduced with permission.[209] Copyright 2017, IOP publishing.

Li-metal/solid–electrolyte interface. Zhao et al. incorporated F into Argyrodite Li$_6$PS$_5$Cl to synthesize Li$_6$PS$_5$Cl$_{0.3}$F$_{0.7}$ and found that the fluorinated electrolyte showed better dendrite

resistance than pure Li$_6$PS$_5$Cl in the Li plating and stripping test.[208] XPS depth profiling spectra collected from the Li/Li$_6$PS$_5$Cl$_{0.3}$F$_{0.7}$ interface, shown in Figure 12c–e, suggested the

**ADVANCED
SCIENCE NEWS**
www.advancedsciencenews.com

**ADVANCED
ENERGY
MATERIALS**
www.advenergymat.de

formation of a LiF-containing interlayer. This new interlayer is stable, robust, and serves as a protective layer against the Li-dendrite formation.

The interfacial interaction between the cathodes and the SE are also frequently studied with XPS depth profiling methods. In particular, the interdiffusion induced by the high-temperature co-sintering process deserves special attention. For achieving a nonreactive interface, Zarabian et al. studied in detail the interface between the $LiCoO_2$ cathode and garnet $Li_7La_3Zr_2O_{12}$ solid–electrolyte.[209] The samples were prepared by spin coating $Li_7La_3Zr_2O_{12}$ (760 nm thickness) on a $LiCoO_2$ pellet and co-annealing at 400 °C. This annealing temperature is below the chemical reaction temperature for these two materials. Nonetheless, XPS depth profiling spectra in Figure 12f indicated that some Co from the $LiCoO_2$ diffused into the $Li_7La_3Zr_2O_{12}$. This observation suggested that the interlayer was still formed at the interface despite the sintering at relatively low temperatures. Therefore, the fabrication of a protective layer at the electrode/SE interface is critical for maintaining the expected performance of ASSB.

4.1.2. Time of Flight Secondary Ion Mass Spectroscopy

ToF-SIMS is a mass spectrometry-based analytical technique.[210] **Figure 13**a shows the working principle of ToF-SIMS.[211] During measurement, a primary ion beam is used to bombard the sample surface, which causes the emission of secondary ions. The emitted secondary ions are then accelerated into a "flight tube" at different velocities depending on their mass-to-charge ratio. By recording their exact arrival time at the detector, the mass of the secondary ions, both positively and negatively charged, can be determined by performing a simple time-to-mass conversion. All elements in the periodic table can be detected, including hydrogen.[211] In addition to the primary ion source, ToF-SIMS instruments are often equipped with an auxiliary ion beam used for sputter etching the sample. Depth profiles can be obtained by performing the experiment with a dual beam in pulsed mode. By raster scanning, the finely focused primary ion beam moves across the etched surface. In this way, a 2D mass-resolved secondary ion image, or chemical map, is recorded. Stacking the 2D chemical maps obtained at different etched depths allows for the 3D elemental
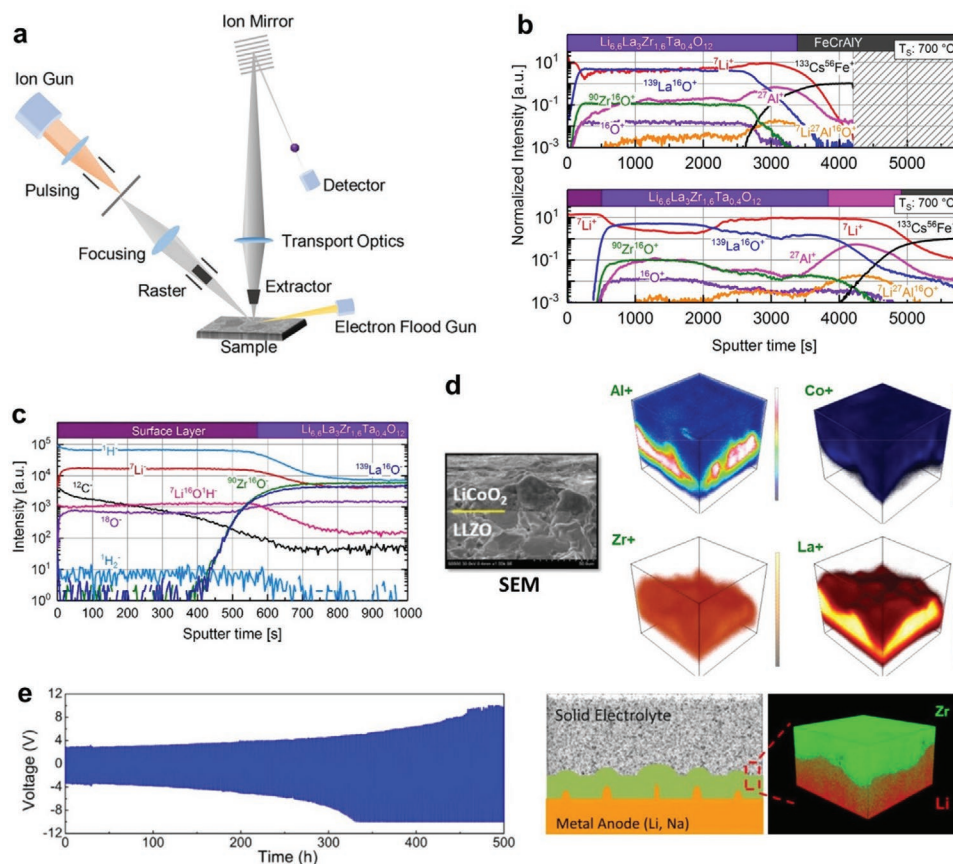
Figure 13. Schematic of the working principle of ToF-SIMS a). ToF-SIMS spectra obtained by analyzing positively charged ions of a $Li_{6.4}La_3Zr_{1.6}Ta_{0.4}O_{12}$ thin film at pristine state (upper image) and after 10-month storage (bottom image) b). ToF-SIMS analysis of negatively charged secondary ions of a $Li_{6.4}La_3Zr_{1.6}Ta_{0.4}O_{12}$ thin film after 10-month storage c). SEM image and corresponding 3D TOF-SIMS elemental maps of the $LiCoO_2/Li_7La_3Zr_2O_{12}$ interface d). e) shows cycling performance of a $Li/Li_{1.15}Y_{0.15}Zr_{1.85}(PO_4)_3/Li$ symmetric cell (left), schematic and 3D ToF-SIMS image of the distribution of Li and Zr at the $Li/Li_{1.15}Y_{0.15}Zr_{1.85}(PO_4)_3$ interface (right). a) Reproduced with permission.[211] Copyright 2020, Wiley-VCH. b,c) Reproduced with permission.[217] Copyright 2020, Elsevier. d) Reproduced with permission.[218] Copyright 2016, American Chemical Society. e) Reproduced with permission.[95] Copyright 2017, American Chemical Society.

**ADVANCED
SCIENCE NEWS**

www.advancedsciencenews.com

**ADVANCED
ENERGY
MATERIALS**

www.advenergymat.de

reconstruction of the sample.[212] ToF-SIMS is commonly used to study solid materials, including insulators, semiconductors, and conductors, with an achievable spatial resolution of 50 nm and depth resolution of a few angstroms.

Depth-resolved ToF-SIMS has been frequently applied in the surface and interface analysis of ASSB.[213–216] Figure 13b showed the ToF-SIMS depth profiles of positively charged secondary ions collected on thin-film $Li_{6.4}La_3Zr_{1.6}Ta_{0.4}O_{12}$ solid–electrolyte.[217] The pristine thin-film solid–electrolyte (top image in Figure 13b) showed a rather homogeneous composition in the depth direction except near the interface with the FeCrAlY substrate due to interdiffusion. After storing in an atmosphere with low oxygen and water content for 10 months, an extra layer was found at the surface (sputter time ≈ 0), as shown in the bottom part of Figure 13b. Positively charged secondary ion depth profiles only showed the presence of Li^+. Complementary depth profiles of the negatively charged secondary ions (Figure 13c) showed that this layer also contained OH^- species, which indicated a LiOH layer formed due to the aging process.

In contrast to XPS depth profiling that only detects depth-dependent information, ToF-SIMS can visualize a 3D interface with laterally resolved information. Figure 13d shows the SEM image and 3D ToF-SIMS elemental maps of the $LiCoO_2$/$Al–Li_7La_3Zr_2O_{12}$ interface.[218] While a sharp interface was observed in the SEM image, ToF-SIMS mapping revealed strong interdiffusion, especially for the Al-ions. The diffusion of Al was not limited to the interfacial area but was also found in the $LiCoO_2$ layer. The migration of Al from Al-substituted $Li_7La_3Zr_2O_{12}$ to the $LiCoO_2$ led to the transformation of $Al–Li_7La_3Zr_2O_{12}$ from cubic phase to the tetragonal phase, which in turn destabilized the cubic lattice structure of the solid–electrolyte.

As one of the few techniques capable of detecting lithium, ToF-SIMS was widely used to investigate the interfacial stability and dendrite formation at the Li-metal/SE interface. The left image in Figure 13e shows the electrochemical performance of a Li-symmetric cell with $Li_{1.15}Y_{0.15}Zr_{1.85}(PO_4)_3$ as the SE, cycled at constant current density. The gradual voltage polarization suggested that an interlayer was formed at the interface.[95] The mixing of Li and Zr observed in the 3D ToF-SIMS compositional map (Figure 13e, right panel) confirms that conclusion. The formation of this interlayer effectively consumed the Li-dendrites, which in turn mitigated their growth and reduced their sharpness.

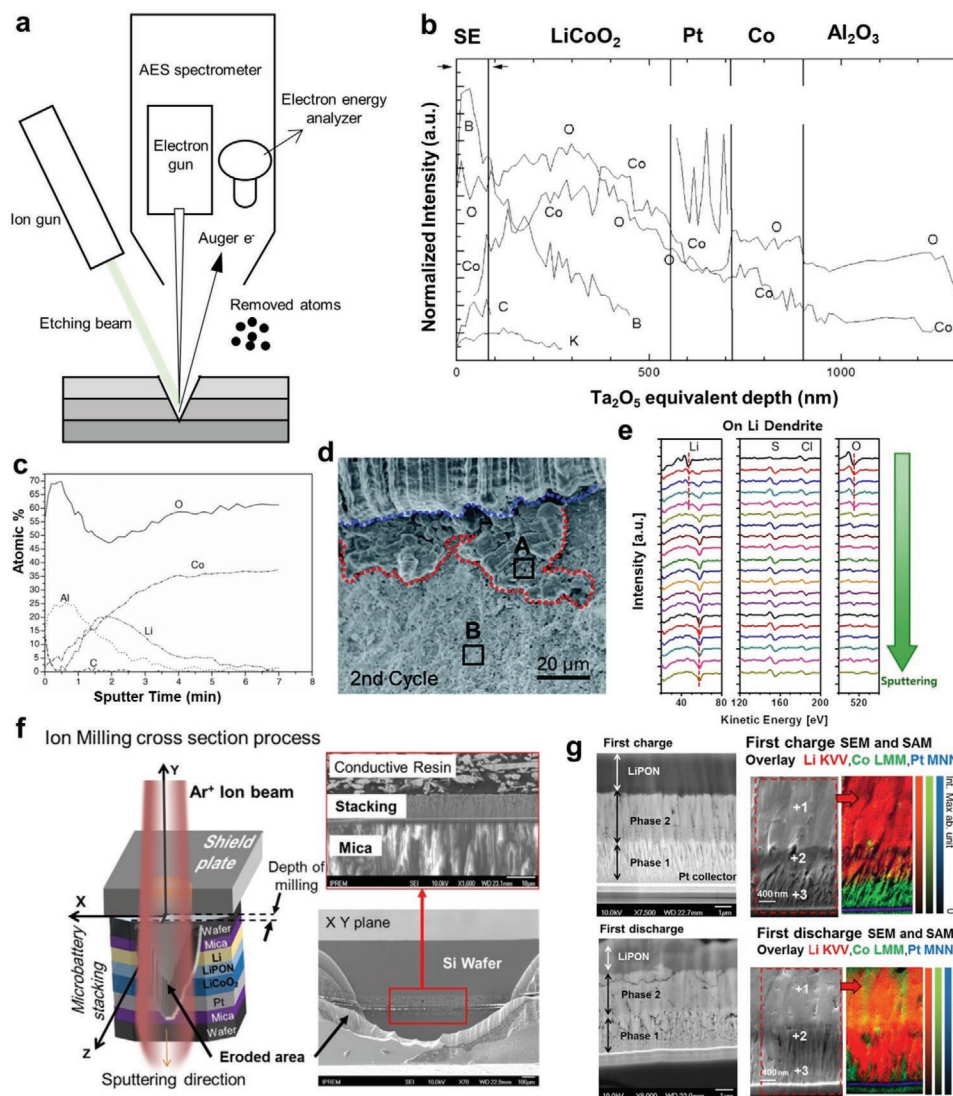### 4.1.3. Auger Electron Spectroscopy and Scanning Auger Microscopy

AES is a surface-sensitive analytical technique. High energy and finely focused electron beam is directed at the sample surface during an AES measurement, ejecting a core electron and leaving behind an unstable hole. Another electron of higher energy may drop down to fill the hole. During this process, a release of energy occurs equal to the difference between the binding energy of the two electrons. This energy can be released in the form of a photon, known as X-ray fluorescence (XRF).[219] It can also be released in the form of a tertiary electron, called auger electron, in which case the released energy is equal to the sum of its binding energy and kinetic energy. Elemental identification is possible by measuring the energy of

the XRF or the kinetic energy of the AES. While it is possible to analyze elements from Li to uranium (U) with AES, it is difficult to detect elements lighter than beryllium (Be) with XRF due to the low fluorescence yield and long characteristic radiation wavelength.[219] The sensitivity to Li is the primary reason why AES is better suited for studying ASSB than XRF. Depth profiling with AES can be achieved with an etching source. **Figure 14**a shows the scheme of an AES setup for depth profiling analysis. Compared to XPS, AES offers a better depth resolution (≈2 nm) due to its surface sensitivity and a better lateral resolution (≈10 nm) for its smaller focal spot size. These enable AES to probe individual particles, micro and nanostructures at or underneath the surface.[220,221]

Figure 14b shows the AES depth profiles of a thin-film bilayered ASSB with $LiCoO_2$ as the cathode and glass $Li_2O–B_2O_3$ as the solid–electrolyte.[222] Ar^+ ion beam was used to etch the surface layers with a sputtering rate of 10 nm min^{-1}. Co element was observed in both the Pt layer and the solid–electrolyte layer, which is a sign of strong intermixing by diffusion. Jeong et al. deposited Al_2O_3 as an interlayer and studied its effect on the interfacial resistance between $LiCoO_2$ and LiPON.[223] Figure 14c shows the elemental depth profiles obtained by etching-assisted AES with a sputtering rate of 3.5 nm min^{-1}.[223] A small amount of Al was found diffusing into the $LiCoO_2$ to form a solid solution of $LiCo_{1-y}Al_yO_2$, which may decrease the interfacial resistance and improve the cycling stability. Choi and co-workers employed AES depth profiling to study the morphology and chemistry of the Li/solid–electrolyte interface in an ASSB (NMC/Li_6PS_5Cl/Li) during cycling.[224] The cross-sectional SEM image in Figure 14d shows protrusion (red dotted lines) at the Li/Li_6PS_5Cl interface (blue dotted lines) after the second charge and discharge cycle. This protrusion is attributed to Li expansion during the Li plating process. AES depth profiles in Figure 14e on the protrusion area (region A) confirmed that the protruded structure was made of Li. Metallic Li (≈58 eV) was detected inside the protruded area, while oxidized Li (≈47 eV) was observed at the surface of the protruded structure.

SAM is an advanced analytical technique based on AES. SAM generates spatially resolved (SR) elemental maps by collecting the auger spectra while scanning the focused electron beam across the sample surface. SAM is often attached to an SEM setup because of their technical similarity. When coupled with an ion-etching source, SAM can also be used to investigate buried interfaces in ASSB. Uhart and coworkers studied the interactions between the $LiCoO_2$ cathode and the LiPON electrolyte by SAM.[225] Figure 14f shows a schematic view and corresponding SEM images of the cross-sectional ion milling process for coupled SEM/SAM analysis of a $LiCoO_2$/LiPON/Li microbattery. The $LiCoO_2$ layer was separated into two phases after the deposition of the LiPON solid–electrolyte. At the end of the first charge (Figure 14g), a uniform Li distribution was observed in the phase close to the solid–electrolyte (phase 2). In contrast, no Li was observed at all in the phase close to the Pt CC (phase 1). Stoichiometry analysis shows that phase 2 at this stage consisted of reduced Co and Li_2O while phase 1 was composed entirely of Co_2O_3. Not much change was observed in phase 2 after the first discharge. Li appeared in phase 1 with a Li/Co ratio of close to 1. The Li-amount and the cobalt oxidation state in phase 1 after discharging were close to those in the pristine sample.
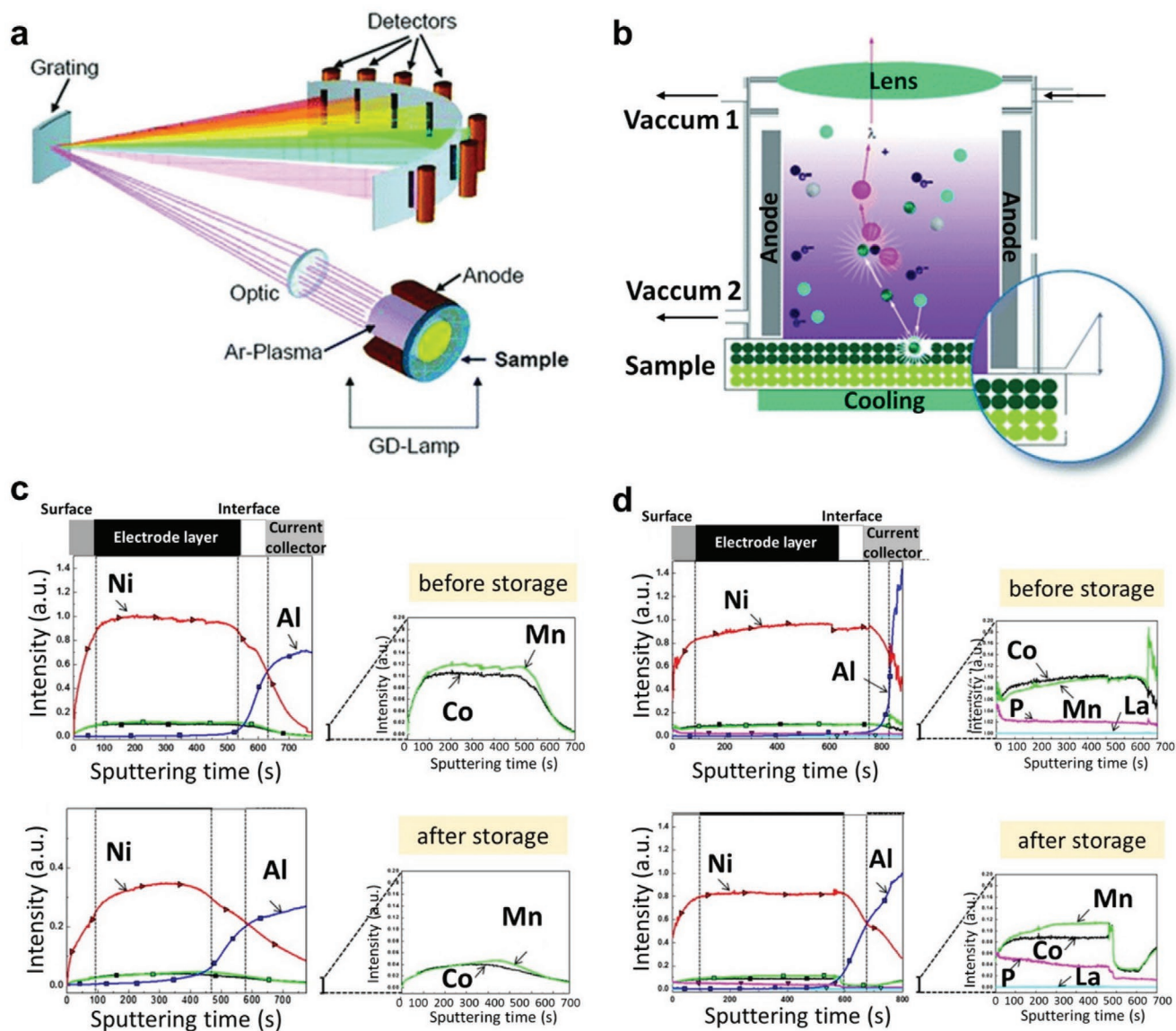
**ADVANCED
SCIENCE NEWS**

www.advancedsciencenews.com

**ADVANCED
ENERGY
MATERIALS**

www.advenergymat.de

Figure 14. Schematic of an AES instrument a). AES depth profile of the solid–electrolyte/$LiCoO_2$ interface b). AES depth profile of the $LiCoO_2$/Al_2O_3 interface c). Cross-sectional SEM image of the Li/LPS interface after discharging d). The AES depth profiles acquired on the Li protrusion in region *A* is shown in (e). Schematic view of the cross-sectional ion milling process and SEM image of microbattery f). SEM images of the sample cross-section after first charging and first discharging. Magnified SEM image on the $LiCoO_2$ layer and SAM overlay of the Li KVV, Co LMM, and Pt MNN signals g). b) Reproduced with permission.[222] Copyright 2003, Springer-Nature. c) Reproduced with permission.[223] Copyright 2016, Elsevier. d,e) Reproduced with permission.[224] Copyright 2019, The Royal Society of Chemistry. f,g) Reproduced with permission.[225] Copyright 2017, American Chemical Society.

4.1.4. Glow Discharge Optical Emission Spectrometry

GD-OES is a spectrochemical technique capable of obtaining a quantitative and depth-resolved chemical profile of a solid.[226] The principle of GD-OES is schematically shown in **Figure 15**a,b.[227] The samples are positioned on top of or directly as the cathode. The high voltage between the anode and the cathode generates an electrical discharge plasma from the injected gas (typically Ar). The plasma bombards the sample surface, removing atoms through sputtering and subsequently exciting them through collisions with high energy electrons. The de-excitation of the atoms is accompanied by the emission of photons, which are characteristic of their corresponding elements. The subsequent recording of the emission spectra given the known sputtering rate generates a depth-resolved elemental profile. Typically, GD-OES instruments are equipped with two sputtering sources: direct current plasma for the analysis of conductive materials and radiofrequency plasma to analyze semiconductors and isolators. GD-OES has become increasingly popular in the past few years, thanks to its wide range of resolvable depth (1 nm–150 μm), quantitative analysis of all elements (including light elements such as H and Li), fast sputtering rate, and low running cost.

A growing number of studies have shown successful applications of GD-OES on lithium-based battery materials. Song and colleagues studied the effect of $LaPO_4$ coating on the performance of $LiNi_{0.5}Co_{0.2}Mn_{0.3}O_2$ cathode when cycled in a liquid

**ADVANCED
SCIENCE NEWS**
www.advancedsciencenews.com
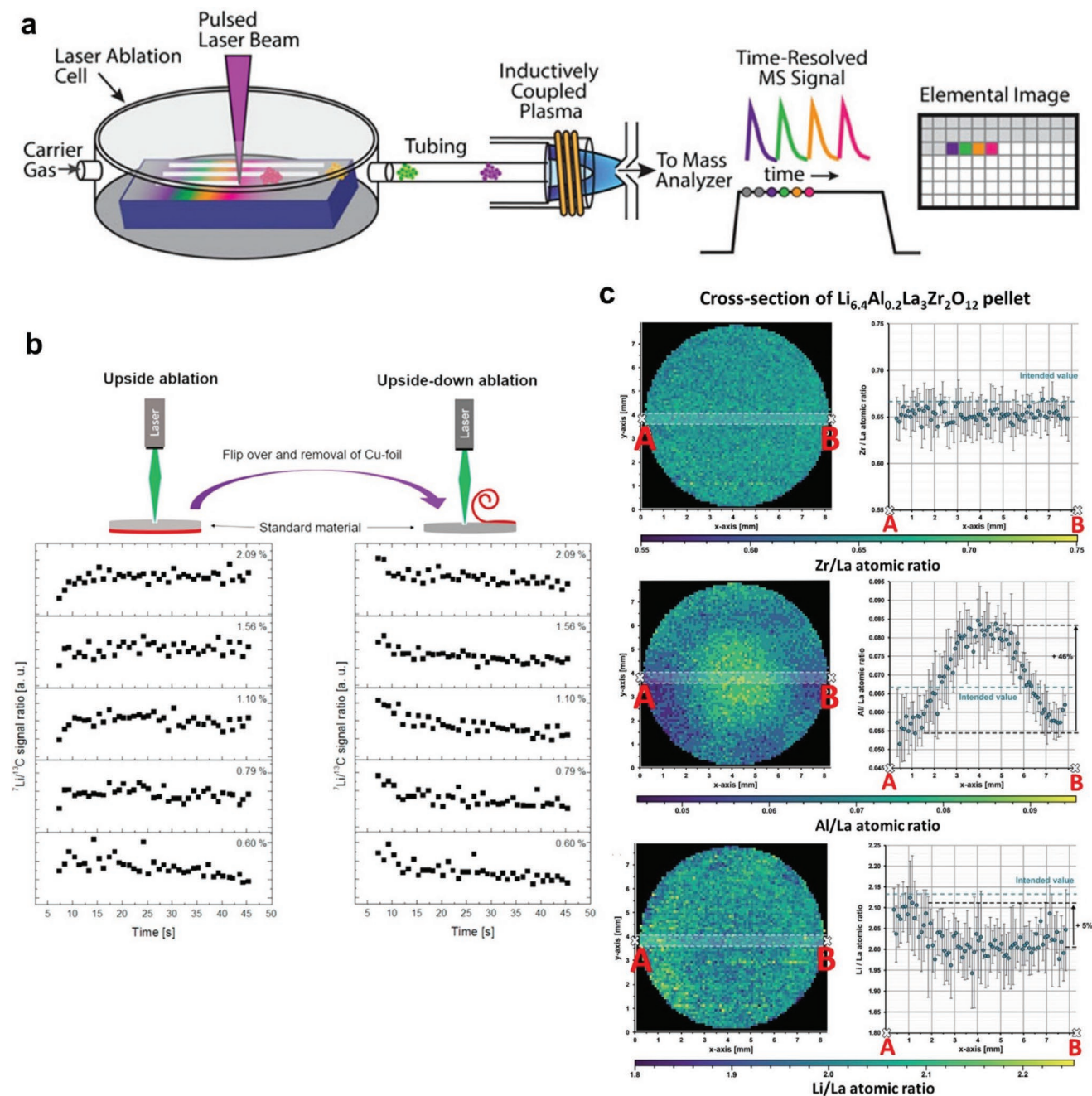
**ADVANCED
ENERGY
MATERIALS**
www.advenergymat.de

Figure 15. Principle of the simultaneous optical spectrometer in GD-OES a) and schematic of the plasma generation and excitation in a GD-lamp b). GD-OES depth profiles of a pristine LiNi$_{0.5}$Co$_{0.2}$Mn$_{0.3}$O$_2$ cathode charged at 4.6 V before and after storage c). Same measurement repeated on a LaPO$_4$-coated cathode sample d). a,b) Reproduced with permission.[227] Copyright 2018, Springer-Nature. c,d) Reproduced with permission.[228] Copyright 2011, Elsevier.

electrolyte.[228] GD-OES depth profiles showed a significant decrease in transition metal emission intensity for the uncoated electrode after 7 days of storage, particularly in regions near the surface and the interface (**Figure 15**c). That suggested a severe dissolution of cathode transition metal atoms into the electrolyte. In sharp contrast, negligible loss of transition metal was observed on the LaPO$_4$ coated electrode after being stored for the same duration (Figure 15d), which explains the improved rate capability and cycling stability. It is worth noting that samples with smooth surfaces and interfaces are desired to maximize the depth resolution of GD-OES. For that reason, we expect to see more applications of GD-OES in the interfacial studies of ASSB, despite current research focusing on commercial cylindrical cells or pouch cells with liquid electrolyte.[229–232]

4.1.5. Laser Ablation Inductively Coupled Plasma Mass Spectrometry

LA–ICP–MS is another powerful depth profiling technique with widespread applicability in both industries and research labs. **Figure 16**a shows the schematic of a typical LA–ICP–MS setup.[233] During the measurement, a pulsed laser beam is focused on the sample surface in a process known as laser ablation. The ablated particles are ionized in an inductively coupled plasma instrument and subsequently analyzed with a mass spectrometer. Depth profiling is enabled by repeatedly ablating the same spot with the pulsed laser beam. Each pulse removes a certain amount of sample thickness. For a given material, the average ablation rate (AAR) is determined

**ADVANCED
SCIENCE NEWS**

www.advancedsciencenews.com

**ADVANCED
ENERGY
MATERIALS**

www.advenergymat.de

Figure 16. Schematic of a LA–ICP–MS imaging setup a). $^7Li/^{13}C$ depth profiles of an aged graphite anode b). LA–ICP–MS elemental imaging of a $Li_7La_3Zr_2O_{12}$ pellet c). The Zr/La, Al/La, and Li/La atomic ratio maps and corresponding line profiles (from point A to B) are shown in (c). a) Reproduced with permission.[233] Copyright 2016, Springer-Nature. b) Reproduced with permission.[234] Copyright 2017, Elsevier. c) Reproduced with permission.[236] Copyright 2020, The Royal Society of Chemistry.

by the laser energy, pulse duration, and frequency. Compared to other ion-beam-based depth profiling techniques, LA–ICP–MS offers some unique advantages such as fast measurement time, simple sample preparation, and sensitivity to all elements except H and He. These capabilities are extremely appealing to the interface characterizations in lithium-based batteries. Like GD-OES, LA–ICP–MS is also a cost-effective tool for the depth-resolved chemical analysis of Li-ion batteries, particularly for the studies of electrode materials.[234,235]

However, the low spatial resolution (lateral resolution of 10 μm and depth resolution of 50 nm) limits its application in more delicate and sensitive analysis.

Schwieters et al. used LA–ICP–MS to determine the lithium content in aged graphite anodes quantitatively.[234] Depth profiling was performed, and the result revealed a loss of lithium in the SEI layer (Figure 16b). Although it is not an ASSB related example, this study demonstrated the potential of LA–ICP–MS in the application of interfacial studies under all-solid-state
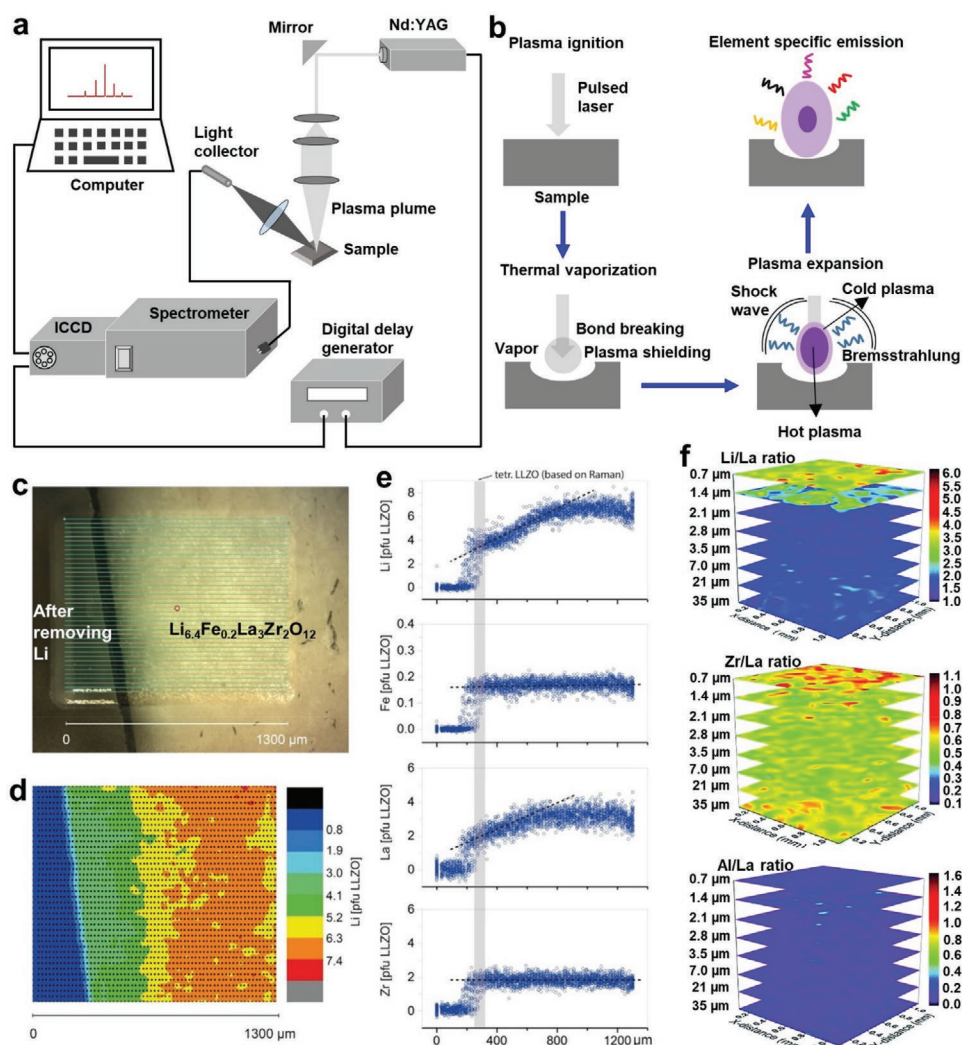
Figure 17. Schematic illustration of a LIBS analytical instrument a) and its working principles b). LIBS investigation of a $Li_{6.4}Fe_{0.2}La_3Zr_2O_{12}$ pellet after removing the Li-metal foil c), Li signal mapping d), and multielemental line scan of Li, Fe, La, and Zr e). 3D atomic ratio analysis of a $Li_7La_3Zr_2O_{12}$ pellet at different depths by LIBS f). c–e) Reproduced with permission.[243] Copyright 2018, American Chemical Society. f) Reproduced with permission.[244] Copyright 2015, The Royal Society of Chemistry.

configurations. More recently, Smetaczek et al. used LA–ICP–MS to study the cubic $Li_7La_3Zr_2O_{12}$ SE.[236] Figure 16c shows the quantitative elemental map of the cross-section of a $Li_7La_3Zr_2O_{12}$ pellet. While the Zr/La atomic ratio was constant throughout the sample, dramatic variations of the Al and Li content were observed. The inner (core) region appeared to be richer in Al, indicating an inhomogeneous substitution of Al in the solid–electrolyte lattice. The outer (surface) region showed a lower Li content due to Li loss during the sintering process. The result highlighted the relationship between the compositional changes and the sintering temperature and is directly associated with the electrochemical performance of the SE.

4.1.6. Laser-Induced Breakdown Spectroscopy

LIBS is laser-based atomic emission spectroscopy for the qualitative and quantitative multielemental analysis of materials and devices.[237,238] Although laser is also used for surface ablations in LA–ICP–MS, the underlying mechanism is very different in the case of LIBS. **Figure 17**a,b shows the schematic design of a LIBS setup and its working principle. During a LIBS experiment, a highly energetic pulsed laser is focused on a small area at the sample surface where it generates a short-lived plasma plume containing free electrons, excited atoms, and ions. As they return to their ground state, the excited species emit element-specific light with unique wavelengths recorded by a charge-coupled device. LIBS is capable of detecting all elements, including H and Li.[239–242]

Like LA–ICP–MS, depth profiling with LIBS is enabled by recording the AAR and the ablation time during the pulsed laser etching. Depth-resolved LIBS has proven useful for the interfacial characterization in ASSB. Rettenwander et al. investigated the interfacial stability of the $Li_{6.4}Fe_{0.2}La_3Zr_2O_{12}$ SE versus Li metal.[243] The solid–electrolyte pellets, assembled in a $Li/Li_{6.4}Fe_{0.2}La_3Zr_2O_{12}/Li$ symmetrical cell, were

**ADVANCED
SCIENCE NEWS**

www.advancedsciencenews.com

**ADVANCED
ENERGY
MATERIALS**

www.advenergymat.de

found to have a high interfacial resistance. An interlayer was observed in the LIBS elemental map (green area in Figure 17d) between the Li-metal anode and the $Li_{6.4}Fe_{0.2}La_3Zr_2O_{12}$ SE. The interlayer showed a lower Li content as compared to bulk $Li_{6.4}Fe_{0.2}La_3Zr_2O_{12}$. Multielemental LIBS line scans (Figure 17e) suggested that while Fe and Zr remain almost constant across the interface, La and Li are slightly depleted near the interlayer. The lower Li content in the interlayer was explained by the transition of $Li_{6.4}Fe_{0.2}La_3Zr_2O_{12}$ from cubic to tetragonal crystal structure. Figure 17f shows the depth-resolved elemental analysis of a $Li_7La_3Zr_2O_{12}$ pellet by LIBS.[244] Each 2D image $(1.11 \times 1.11 \ \mu m^2)$ was obtained by sampling over a 15×15 grid. The sample surface was ablated by 50 laser pulses, with an AAR of 700 nm per pulse, to produce the stack of 50 depth-resolved maps. The results suggested a nonuniform chemical distribution in both the lateral and the depth direction. A higher Li concentration was observed at the $Li_7La_3Zr_2O_{12}$ pellet surface and was attributed to the formation of Li_2CO_3 in the air. That, in turn, explains the observed high interfacial resistance.[245,246] The study exemplified the capability of LIBS for the 3D elemental imaging of impurity distribution at the interface.

4.2. Ion Beam Analysis

IBA refers to a cluster of analytical techniques that use MeV ion beams to achieve depth-resolved elemental profiling of solid materials up to a few micrometers beneath their surface.[247,248] **Figure 18**a illustrates the working principle of several IBA techniques. During the measurement, an ion beam is directed at the sample, resulting in interactions between the incident ions and atoms in the target material. The most common IBA technique is RBS. RBS determines the composition in the sample by measuring the energy and the number of ions backscattered by the target nucleus. For elastic scattering, the conservation of energy and momentum dictates a direct relationship between the energy of the backscattered ions and the target mass and depth. The forward-recoiled ions can also be measured. The related IBA technique is known as ERDA.

ERDA is unique in its high sensitivity to hydrogen and deuterium, with a detection limit on the order of 0.01 at%. The incident ions can excite and remove a core electron from the atom. A characteristic X-ray is emitted when an outer shell electron fills the inner shell vacancy. The IBA technique that analyzes the element-specific X-ray fluorescence emission is PIXE. PIXE is generally more efficient in identifying heavy elements, which is difficult for RBS due to their similar masses. The incident ions may also interact with the target nucleus by a nuclear reaction, often under resonance conditions, promoting the emission of secondary particles (NRA) or gamma-rays (PIGE). NRA is the IBA technique that measures this ionizing radiation. Compared to PIXE and RBS, NRA is particularly useful for identifying light elements, from hydrogen to fluorine. The secondary particles in NRA, backscattered ions in RBS, and forward-recoiled atoms in ERDA all have well-defined relationships connecting their energy to the depth of the interacted atoms. Moreover, the amount of the detected particles is proportional to the concentration of the target element, allowing for quantitative analysis of depth-resolved composition in solid materials.

We recall that only atoms lighter than the incident ion can be recoiled in ERDA. Only atoms heavier than the incident ions can backscatter them in RBS. Therefore, the detectable elements by ERDA are usually lighter than those by RBS. Figure 18b illustrates these phenomena showing the collected RBS and ERDA spectra at different interfaces of a pristine Pt(16 nm)/Li–Al–Ge–Ti–P–O(150 μm)/LiCoO$_2$ (65 nm)/Au(24 nm) battery, measured using an O^{4+} beam.[249] RBS is extremely sensitive to heavier elements such as Au and Pt while ERDA is capable of detecting H. Because of the thick solid–electrolyte, backscattered particles are fully stopped beyond a certain depth. Consequently, the battery was flipped during the RBS and ERDA experiments in order to resolve both the anode/solid–electrolyte and solid–electrolyte/cathode interfaces. The backscattered ions (RBS) and forward-recoiled atoms (ERDA) that originated near the surface show up on channels with higher channel numbers. Film thickness can be deduced from the FWHM of the peaks, and with that, the thickness of the Pt CC was determined to be 16 nm. Figure 18c,d shows respectively the raw ERDA spectra at the Li–Al–Ge–Ti–P–O/LiCoO$_2$/Au and Pt/Li–Al–Ge–Ti–P–O interfaces, under different charging voltage bias.[249] With increasing bias, the Li$^+$ signal in the LiCoO$_2$ layer decreases (Figure 18c) due to the delithiation of the cathode. In the meantime, the Li$^+$ signal near the Pt surface increases (Figure 18d), which is reflective of Li plating on the anode. These outcomes established ERDA as a useful tool for studying Li$^+$ transportation in situ in ASSB. RBS and ERDA are extremely powerful for studying thin films. Figure 18e,f shows the RBS and ERDA spectra of a thin film battery stack of Au/Si/LiPON/LiCoO$_2$/Au/Al(substrate), with a total thickness of less than 4 μm.[250] A 5.4 MeV He^{2+} ion beam was used during the analysis, probing from the side of the Al substrate. All of the thin-film battery layers were clearly resolved from both the RBS and ERDA spectra. In situ RBS and ERDA investigations were also performed. The result revealed Li leakage from the LiPON into the Al substrate.

Li$^+$ can also be used as the incident ions in IBA. In the so-called co-incidence approach, depth profiling of thick ASSB can be achieved by measuring both the forward-recoiled and forward-scattered Li particles. Figure 18g shows the scheme of such an experiment on a full battery (Ti/NbO/LiPON/LiMn$_2$O$_4$/Ti-substrate) using a 5 MeV ^{7}Li$^+$ ion beam.[251] Two detectors were placed downstream of the battery at 45° angles to collect respectively the scattered and recoiled Li particles. Because the energy of the incident Li-ion is shared by the forward-scattered and recoiled Li particles, averaging the results on the two detectors helped increase the depth resolution. Figure 18h shows the experimentally averaged and simulated Li depth profiles at different SoC. The result at 0 V showed that some Li had already diffused into the NbO and Ti layers during sample preparation. After applying 3 V for 25 min, the Li signal decreased in LiMn$_2$O$_4$ and increased in NbO, indicating a Li transfer from the cathode to the anode. By over biasing at 5 V for 45 min, an uneven Li distribution within the LiPON was observed. Moreover, Li-ions were agglomerating at the LiPON/NbO interface and diffused strongly into the Ti layer.
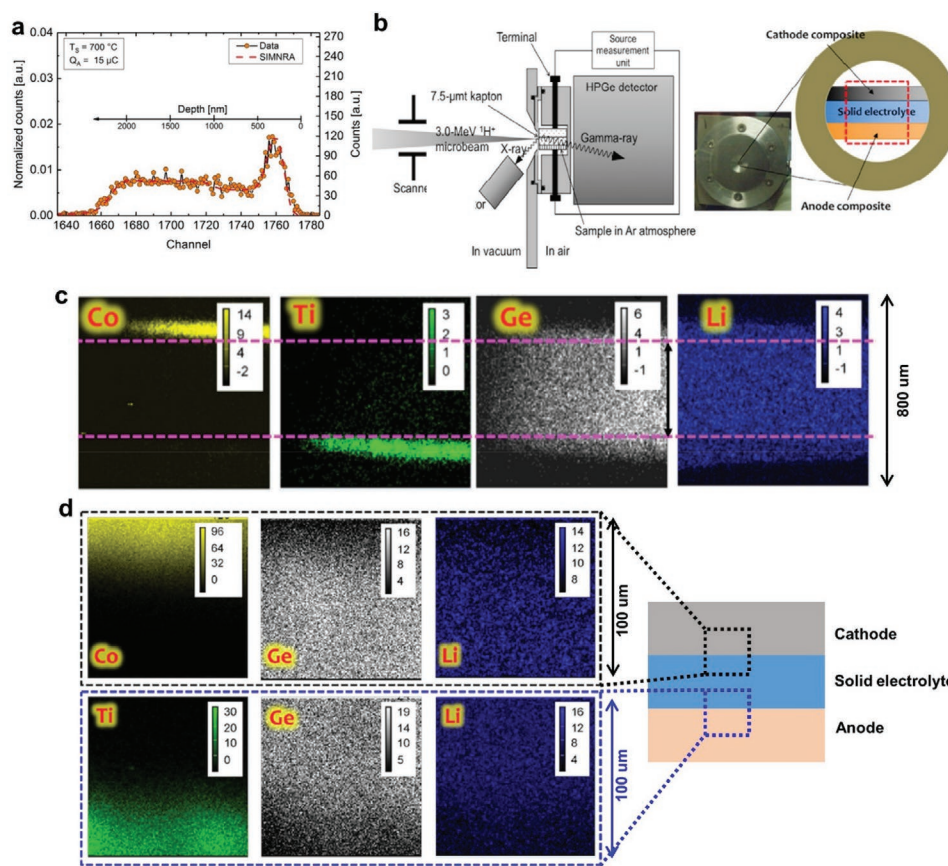
As mentioned earlier, the NRA is particularly powerful for the depth profiling of light elements in the heavy matrix. Depending on the target element, specific ion beams are
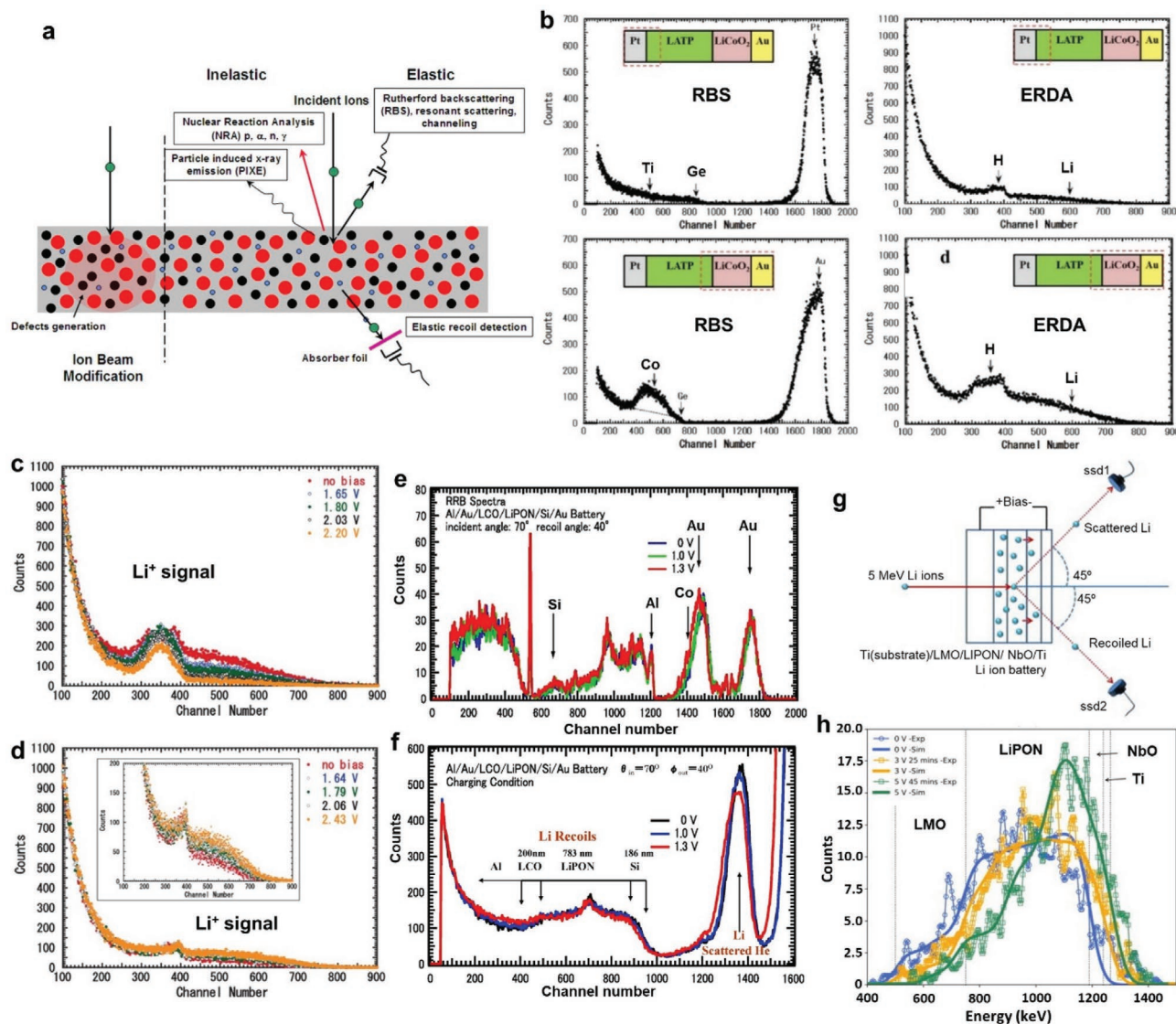
Figure 18. Schematic illustration of the IBA techniques a). RBS and ERDA depth profiles of an as-prepared Pt/Li–Al–Ge–Ti–P–O/LiCoO$_2$/Au battery b). The battery was flipped during the measurement to gain access from both sides. In situ ERDA spectra collected from the Li–Al–Ge–Ti–P–O/LiCoO$_2$/Au side c) and from the Pt/Li–Al–Ge–Ti–P–O side d). RBS e), and ERDA f) spectra of a thin film Al/Au/LiCoO$_2$/LiPON/Si/Au battery at different SoC measured by 5.4 MeV He^{2+}. Schematics of the co-incidence ERDA experiment using 5 MeV ^{7}Li-ions on a thin-film battery g). Simulated and experimental ERDA spectra of the Ti/NbO/LiPON/LiMn$_2$O$_4$/Ti ASSB at different SoC h). a) Reproduced with permission.[247] Copyright 2008, Kin Man Yu. b–d) Reproduced with permission.[249] Copyright 2019, Wiley-VCH. e,f) Reproduced with permission.[250] Copyright 2018, Elsevier. g,h) Reproduced with permission.[251] Copyright 2020, AIP Publishing.

selected to promote the desired nuclear reactions. In the case of detecting Li in ASSB, the most commonly used ion beam is a proton. The related nuclear reaction is written as ^{7}Li$(p,\alpha)^4H$, where the resulted α particles are used for determining depth-resolved Li distribution. **Figure 19**a shows the NRA Li depth profile of a Li$_{6.4}$La$_3$Zr$_{1.6}$Ta$_{0.4}$O$_{12}$ solid–electrolyte using ^{7}Li$(p,\alpha)^4H$.[217] The channel number here is indicative of the particle energy. A higher channel number implies a higher particle energy, which indicates that the particle was generated near the surface. The result showed a higher Li content close to a depth of 400 nm, which was attributed to the presence of LiOH at the surface. The Li distribution was otherwise homogeneous for the majority of the Li$_{6.4}$La$_3$Zr$_{1.6}$Ta$_{0.4}$O$_{12}$ electrolyte.

The subtechnique of NRA that specifically measures the generated gamma radiation is known as PIGE.[252] The nuclear reaction that probes Li with PIGE is ^{7}Li$(p, p'\gamma)^7$Li. In practice, PIGE is often performed together with PIXE to obtain complementary profiles on other elements. Figure 19b illustrates an IBA setup for the simultaneous PIXE and PIGE measurements of an ASSB.[253] A 3 MeV proton microbeam was directed at the surface of a full bulk-type ASSB (LiCoO$_2$/Li$_{10}$GeP$_2$S$_{12}$/TiS$_2$). The characteristic X-ray was detected by a Si(Li) detector in front of the test ASSB, while the 478 keV gamma radiation was detected by a high purity germanium (HPGe) detector placed behind it. Figure 19c shows the elemental profile of the ASSB cross-section obtained from the PIXE (Co, Ge, Ti) and PIGE

**ADVANCED
SCIENCE NEWS**

www.advancedsciencenews.com

**ADVANCED
ENERGY
MATERIALS**

www.advenergymat.de

Figure 19. The energy-selective count rate of α particles corresponding to the ^{7}Li(p,α)^{4}He nuclear reaction of the aged Li$_{6.4}$La$_3$Zr$_{1.6}$Ta$_{0.4}$O$_{12}$ sample a). Schematic drawing of the experimental layout for the PIXE and PIGE measurement b). Results of elemental mapping with PIXE (Co, Ti, and Ge) and PIGE (Li) at the cross-section of a LiCoO$_2$/Li$_{10}$GeP$_2$S$_{12}$/TiS$_2$ solid battery c). High-resolution maps on selected areas in (c) are shown in (d). a) Reproduced with permission.[217] Copyright 2020, Elsevier. b–d) Reproduced with permission.[253] Copyright 2017, World Scientific.

(Li) measurements. Ge from the solid–electrolyte was also found in the cathode and in the anode. Figure 19d shows the enlarged view of the cathode/SE and SE/anode interfaces. Both the cathode and anode showed a Li-ion concentration gradient across the interface. The difference in the number of Li-ions at the anode/solid–electrolyte interface of merely 0.26×10^{-4} mol was clearly detected. Thus, the study showcased microbeam PIGE as a promising technique for the quantitative analysis of Li distribution in ASSB.

4.3. Transmission Electron Microscopy-Based Techniques

4.3.1. Electron Energy Loss Spectroscopy

EELS measures the kinetic energy loss of incident electrons as they undergo inelastic scattering by the sample specimen. There are many sources that contribute to the inelastic scattering, such as phonon and plasmon excitations, inter and intraband transitions, inner-shell ionizations, etc. Among them, inner-shell ionization is particularly useful for finger-printing the elements in the sample. Compared to energy-dispersive X-ray spectroscopy (EDX or EDS), inner-shell ionization EELS shows higher sensitivity to light elements.

Thus, it is ideal for studying the Li distribution in LBB. Information on the chemical bonding and covalence state is also possible with EELS, by analyzing the fine structures in the energy loss spectrum.[254,255] EELS is available with both TEM and scanning TEM (STEM).[256] The main advantage of STEM–EELS is its capability to perform spatially resolved spectrum imaging. **Figure 20**a shows the schematic of a novel in situ STEM–EELS setup for a LiCoO$_2$/LiPON/Si solid battery.[85] The nanobattery was electrochemically controlled via a scanning tunneling microscopy (STM) tip in contact with the anode current collector. Spatially resolved EELS mapping of the ASSB revealed the formation of a Li-accumulating interlayer between the cathode and the solid–electrolyte upon cycling. The main limitation of STEM–EELS is the potential beam damage by the convergent beam, and for that reason, TEM–EELS is recommended for beam-sensitive samples. Ex situ TEM–EELS has been applied in the interfacial studies of ASSB,[257,258] but does not typically offer good spatial information. SR–TEM–EELS is demonstrated by a special setup, the schematic of which is shown in Figure 20b.[259] By adjusting the lens system, 1D (x-direction) of the 2D charge-coupled device camera captures the EELS spectra while the other dimension offers spatially resolved information on the sample y-direction. Thanks to the reduced beam damage, operando observations on
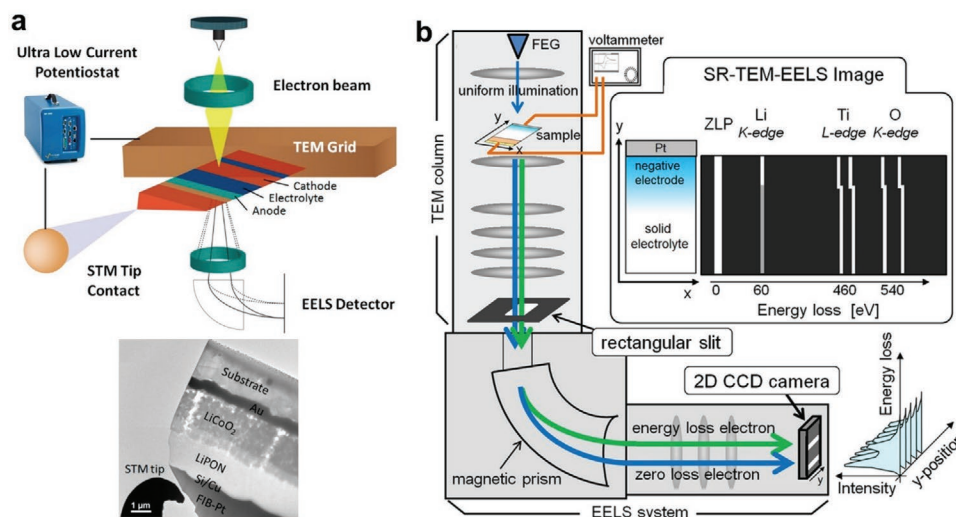
Figure 20. Schematic and TEM bright-field image of the in situ STEM–EELS nanobattery setup a). Schematic illustration of the experimental setup for SR–TEM–EELS b). a) Reproduced with permission.[85] Copyright 2016, American Chemical Society. b) Reproduced with permission.[259] Copyright 2016, Oxford University Press.

Li transportation were performed across the electrode/SE interface. TEM- and STEM–EELS are both limited by their restrictions on sample thickness. The samples are typically prepared with a focused ion beam (FIB) to a thickness no greater than 100 nm. Sample preparation is more relaxed in a scanning electron microscope (SEM). The associated technique is known as reflection EELS (REELS).[260]
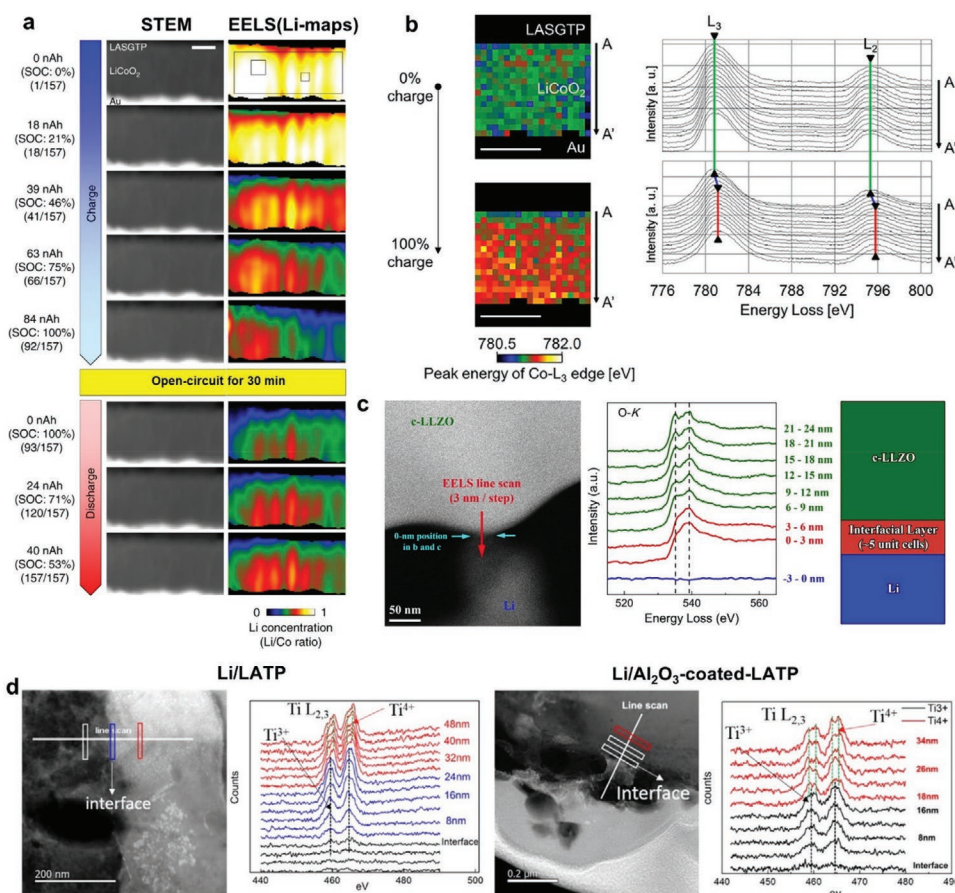
The high interfacial resistance between the cathode and the solid–electrolyte is one of the main factors limiting the rate performance of an ASSB. Understanding the dynamic evolution at the interface is thus crucial to unraveling the underlying mechanism. Nomura et al. applied in situ STEM–EELS to monitor the Li distributions at the $LiCoO_2/Li_{1+x+y}Al_x(Ti,Ge)_{2-x}Si_yP_{3-y}O_{12}$ interface in an ASSB.[261] **Figure 21**a shows the STEM images and the corresponding Li/Co ratio EELS maps across the cathode/solid–electrolyte interface at different SoC. Li release and uptake were clearly observed during charging and discharging at the cathode. More interestingly, the remaining Li was spontaneously redistributed in the lateral direction between the $LiCoO_2$ domains during the resting period. Figure 21b shows the 1D spatially resolved $Co-L_{2,3}$ EELS spectra measured near the $LiCoO_2/Li_{1+x+y}Al_x(Ti,Ge)_{2-x}Si_yP_{3-y}O_{12}$ interface at pristine and fully charged state.[262] After charging, the peak position of the $Co-L_{2,3}$ edge in the bulk $LiCoO_2$ was shifted to higher energy loss, corresponding to the oxidation of Co from Co^{3+} to Co^{4+}. In contrast, the peak position of the Co within 10–20 nm from the interface remained unchanged, indicating the presence of an inactive $LiCoO_2$ layer. This interlayer is responsible for the high interfacial resistance in the investigated ASSB. More recently, the same authors studied the lithium transfer resistance in $LiNi_{0.8}Co_{0.15}Al_{0.05}O_2$ secondary particle cathodes in bulk type ASSB.[263] Their in situ STEM–EELS results revealed abrupt changes in Li concentration at grain boundaries, which was explained by the crystal orientation mismatch between adjacent secondary particles. The result offered invaluable insight into the effect of nanocrystal orientations on the rate capability of ASSB. Kato et al. studied the effect of sintering temperature on the interfacial resistance between NCM and $Li_2O–Al_2O_3–SiO_2–P_2O_5–TiO_2–GeO_2$ SE.[264] Their TEM–EELS analysis detected an accumulation of reduced-valence Co at the interface when sintered at 900 °C. Together with the formation of Li-free impurities, this phenomenon contributed to the drastic 1000 fold increase in interfacial resistance compared to those sintered at 700 °C.

Issues at the anode/solid–electrolyte interface are equally important to an ASSB, especially when Li-metal is used as the anode material. Many SE suffer from chemical reduction upon direct contact with the Li-metal anode. Understanding the interaction between Li-metal and the SE is essential for developing high-performance ASSB. Ma et al. used STEM–EELS to study the chemical and structural evolution at the $Li/Li_{7-3x}Al_xLa_3Zr_2O_{12}$ interface.[265] The HAADF–STEM image, shown in Figure 21c, suggested a sharp boundary at the $Li/Li_{7-3x}Al_xLa_3Zr_2O_{12}$ interface. However, O–K edge EELS line scan across the interface (Figure 21c) revealed the presence of a 6 nm thick interlayer in the solid–electrolyte, which was formed upon contact with the Li-metal. This interlayer was found to have a tetragonal-like crystal structure with similar ionic conductivity as the used solid–electrolyte. Further analysis revealed that this interlayer functioned as the type 4 interlayer discussed in Figure 7 and effectively prevented further chemical reaction and structural transformation at the Li/solid–electrolyte interface.

Adding an artificial buffer layer between the Li-metal and the SE is a promising approach to stabilize the interface in ASSB. Despite their apparent advantage, the working mechanism of the artificial buffer layers is not well understood. Typically, the buffer layer has a thickness of tens of nanometers, making the characterization a challenge to many techniques. (S)TEM–EELS is the ideal tool for this purpose. Liu et al. deposited an Al_2O_3 layer on $Li_{1.3}Al_{0.3}Ti_{1.7}(PO_4)_3$ solid–electrolyte to stabilize the Li/$Li_{1.3}Al_{0.3}Ti_{1.7}(PO_4)_3$ interface and unveiled its working mechanism by TEM–EELS.[153] Figure 21d shows the high-resolution TEM (HRTEM) images as well as EELS line scans of bare and Al_2O_3-coated solid–electrolyte after being cycled in Li-symmetric

ADVANCED
SCIENCE NEWS
www.advancedsciencenews.com

ADVANCED
ENERGY
MATERIALS
www.advenergymat.de

Figure 21. In situ STEM and EELS measurement of the $LiCoO_2/Li_{1+x+y}Al_x(Ti,Ge)_{2-x}Si_yP_{3-y}O_{12}$ interface at different SoC a). Peak position maps of the Co-L_3 edge and the corresponding EELS spectra of Co-$L_{2,3}$ from position A to A' across the $LiCoO_2/Li_{1+x+y}Al_x(Ti,Ge)_{2-x}Si_yP_{3-y}O_{12}$ interface at pristine and fully charged state b). HAADF–STEM image of the $Li/Li_{7-3x}Al_xLa_3Zr_2O_{12}$ interface and corresponding O–K edge EELS line scan results c). HRTEM image of the $Li/Li_{1.3}Al_{0.3}Ti_{1.7}(PO_4)_3$ interface and corresponding Ti $L_{3,2}$-edge EELS line scan for bare and Al_2O_3-coated samples d). a) Reproduced with permission.[261] Copyright 2020, Springer-Nature. b) Reproduced with permission.[262] Copyright 2018, American Chemical Society. c) Reproduced with permission.[265] Copyright 2016, American Chemical Society. d) Reproduced with permission.[153] Copyright 2018, American Chemical Society.
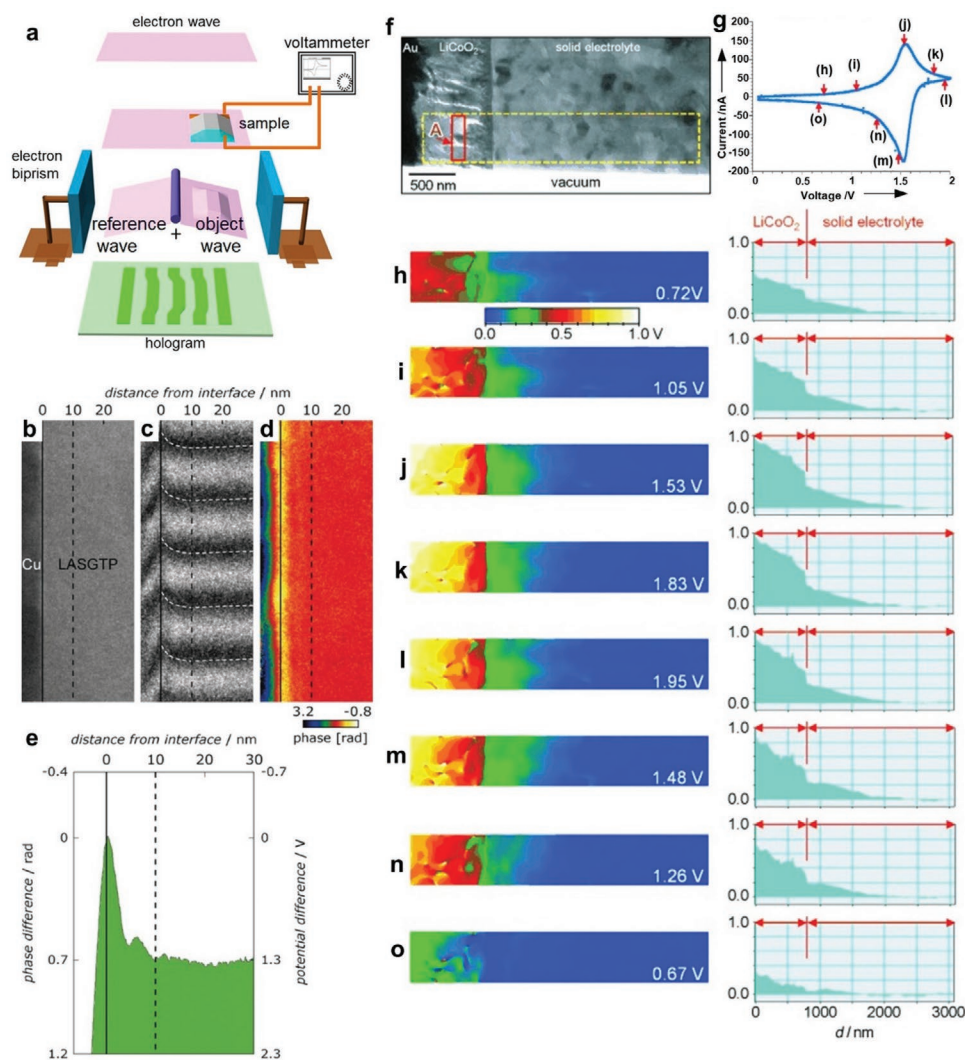
cells for 100 cycles. The EELS line scan revealed the formation of a Ti^{3+} dominant interlayer of 24 nm between the Li and bare $Li_{1.3}Al_{0.3}Ti_{1.7}(PO_4)_3$ because of the unstable interface. However, after coating the solid–electrolyte with an Al_2O_3 buffer layer, the thickness of the Ti^{3+} dominant interlayer was reduced to 16 nm. Based on these observations, the authors concluded that the Al_2O_3 layer could mitigate the reduction of the electrolyte by the Li-metal. Despite the strict requirement on sample thickness, it can be expected that (S)TEM–EELS analysis will continue to play an essential role in understanding interfacial issues in ASSB, particularly in situ and operando.

4.3.2. Electron Holography

EH is an advanced microscopic technique used for the quantitative measurement of electrostatic potential[266,267] and magnetic field distribution[268,269] in materials or devices. EH is designed initially as a method to improve the resolution of electron microscopy in the 1940s.[270] To date, more than twenty variants of EH methods have been developed.[271] Among them,

the off-axis EH mode is the most popular technique for investigating electric potential distribution inside ASSB. Because off-axis EH can be performed with a TEM, high spatial resolution (<1 nm) is routinely achieved.

The principle of off-axis EH is schematically shown in **Figure 22**a.[259] The incident wave is split into two parts by a positively charged wire. The part that encodes information about the sample is known as the object wave. The part that passes through the vacuum is known as the reference wave. The two waves then interfered with each other to form a hologram on the camera. The phase image can be reconstructed with the phase-shifting method from a series of holograms taken after tilting the incident electron wave.[272–274] The electrostatic potential inside the sample is then directly proportional to the phase difference extracted from the reconstructed phase image. In an ASSB, the electrostatic potential is reflective of the distribution of the Li-ions, which itself is strongly affected by the presence and properties of the interfaces. Off-axis EH has been used to study the interfacial phenomena in ASSB. Figure 22b–d shows the cross-sectional TEM image, as-recorded hologram, and reconstructed phase image of a pristine $Cu/Li_{1+x+y}Al_x(Ti,Ge)_{2-x}Si_yP_{3-y}O_{12}/Cu$ sample.[274] Figure 22e shows

**ADVANCED
SCIENCE NEWS**

www.advancedsciencenews.com

**ADVANCED
ENERGY
MATERIALS**

www.advenergymat.de

Figure 22. Schematic illustration of the EH working principle a). Cross-sectional TEM image b), corresponding hologram image c) and reconstructed phase map d) at the $Cu/Li_{1+x+y}Al_x(Ti,Ge)_{2-x}Si_yP_{3-y}O_{12}$ interface. The phase-potential profile in (e) was generated by integrating along the vertical direction of (d). Bright-field TEM image at the $LiCoO_2/Li_{1+x+y}Al_xTi_{2-x}Si_yP_{3-y}O_{12}$ interface f). CV curve for the in situ EH measurement g). 2D potential images (left) and corresponding line profiles (right) during the charging–discharging process h–o). a) Reproduced with permission.[259] Copyright 2016, Oxford University Press. b–e) Reproduced with permission.[274] Copyright 2019, Wiley-VCH. f–o) Reproduced with permission.[277] Copyright 2010, Wiley-VCH.

the 1D phase-potential profile generated by integrating along the vertical direction of the phase image. The peak in the phase-potential profile corresponds to a 10 nm wide Li-rich space charge layer. The results indicate that the space charge layer is formed intrinsically in the solid–electrolyte upon contact with the Cu.

Li-ions, and, as a result, the electric potential in the ASSB, may change during postmortem analysis. Therefore in situ characterizations are required to study the functioning battery in the nonequilibrium states. Conducting in situ or operando off-axis EH on ASSB is particularly challenging because of issues such as electric field leakage, damage by FIB milling, and sample reaction with air. Electric field leakage refers to the external electric field formed around the sample when an electric bias is applied. Both the external and internal electric fields contribute to the phase shift in the reconstructed images.[275] Thus, removing the electric field leakage effect is essential for quantifying the electrostatic potential in the ASSB.[275,276]

With in situ EH, Yamamoto et al. investigated the potential evolution at the $LiCoO_2/Li_{1+x+y}Al_xTi_{2-x}Si_yP_{3-y}O_{12}$ interface (yellow dotted box region of Figure 22f) during (de)lithiation. Based on potential images shown in Figure 22h–o, they found that the resistance was mainly attributed to 1 µm thick layer at the cathode/solid–electrolyte interface.[277] Indeed, the potential was almost constant inside the solid–electrolyte far away from the interface but rapidly changes when approaching the interface. The gradual slope on the solid–electrolyte side of the potential profile is due to the formation of a Li-deficient region with a net negative charge.

4.3.3. Cryogenic Electron Microscopy (Cryo-EM)

Cryo-EM is a branch of electron microscopy techniques that studies samples at cryogenic temperatures. Conceived in the

1970s as a countermeasure for electron beam damage, cryo-EM has gained huge momentum in recent years following the invention of direct electron detection detectors and the award of Nobel Prize in Chemistry. Although primarily applied on vitrified biological samples, cryo-EM has also found success in material science. Cryo-EM experiments on battery materials are often performed in conventional electron microscopy with a cryogenic transfer or cooling holder rather than in specialized instruments designed for structural biology. This is because while the latter is made to ensure minimum contamination, the former offers some crucial advantages such as the flexibility to perform EDS/EELS and simple data processing. The main motivation of using cryo-EM is its ability to preserve Li metal and other battery components in their native state for quantitative analyses.[278,279] The mitigated beam damage allows higher dose and thus higher resolution images to be taken. It has been shown that the Li atoms in dendrites can sustain 30 s of exposure at 1000 e $Å^{-2}$ s^{-1} without any changes on atomic resolution images.[280] New cryo-FIB techniques are adopted to conserve fully intact interfaces during milling while other innovative ways of sample preparation (e.g., using redeposited Li[279] as the connection material instead of Pt) have been developed to further protect the reactive materials in their pristine state.

Despite being an emergent technique, cryo-EM has already made significant breakthroughs in reshaping our understanding of structural evolutions at the liquid–electrolyte–electrode interface. Cryo-EM research involving ASSB has become increasingly popular in the past 2 years. A new type of Argyrodite SE $Li_{6.5}P0_5Ge_{0.5}S_5I$ for ASSB was developed by Song et al. and captured for the first time on cryo-TEM, after failed attempts by conventional EM that resulted in the immediate destruction of the materials.[281] The local structure of the 700 nm particle was identified as (111) oriented Argyrodite cubic, while its chemical composition was confirmed by cryo-STEM–EELS measurement. Compared to inorganic SE, solid polymer electrolytes are even more vulnerable under the electron beam. Sheng e al. investigated the interface between Li and PEO at the atomic level with cryo-TEM.[282] They showed that the interface was originally an amorphous compound with randomly distributed Li, LiOH, Li_2O, and Li_2CO_3 nanocrystals. The use of Li_2S additives promotes the formation of LiF nanocrystals, which has the effect of stabilizing the interface against parasitic reaction between Li and PEO. The same authors also studied the positive impact of $Mg(TFSI)_2$ additives[283] and Pt nano-interlayer[284] on the same material system. More recently, the Li/LiPON interface was preserved by cryo-FIB and characterized by cryo-EM techniques.[279] An interlayer of <80 nm thick was observed by cryo-high-resolution TEM which consists of a variety of crystalline decomposition products embedded in an amorphous matrix. The nature of these nanocrystals was further revealed by Cryo-STEM–EELS to be Li_2O, Li_3N, and Li_3PO_4.

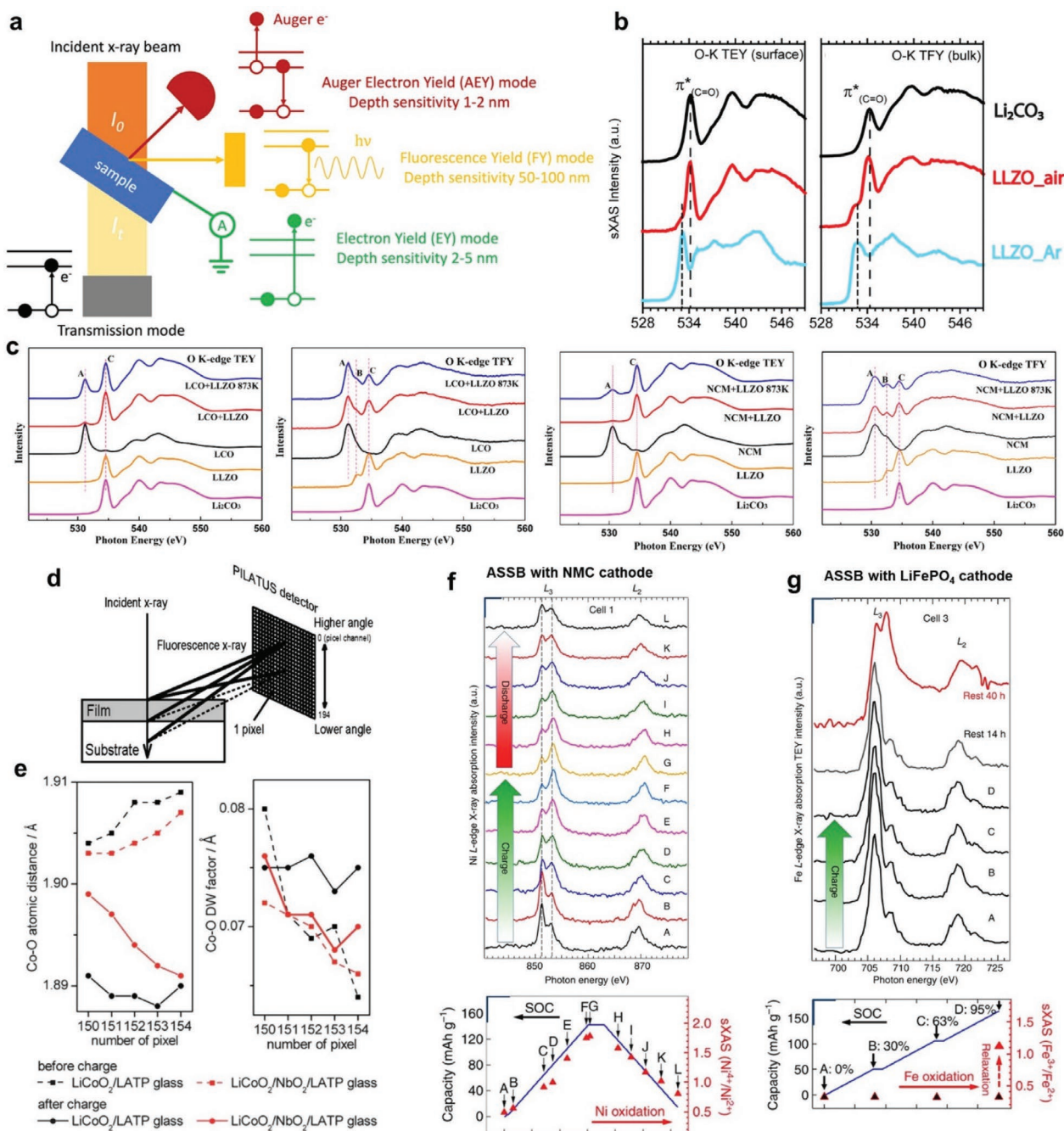## 4.4. Synchrotron X-Ray Techniques

A synchrotron uses the deflection of relativistic electrons to generate extremely bright light, typically in the X-ray regime. When measured in terms of brilliance, a third-generation synchrotron offers a quality of light that is more than a billion times superior to a laboratory source. Synchrotron light is produced in the storage ring and harnessed by beamlines. Each beamline consists of optical devices to reshape (e.g., monochromatize, collimate, focus, etc.) the X-ray beam and experimental end stations to carry out the measurements. While the technique employed by each beamline differs, they all make use of one or more forms of X-ray interaction with matter, such as scattering, absorption, and refraction. The rest of this section reviews the latest results on ASSB research using synchrotron X-ray techniques.

4.4.1. X-Ray Absorption Spectroscopy

XAS is a collective term for two analytical techniques that measure modulations in the X-ray absorption cross-section near the core-level binding energies of a selected element. X-ray absorption near-edge spectroscopy (XANES), as its name suggests, covers the part of the spectrum immediately after the absorption edge and contains information about the bonding and oxidation state of the selected element. Extended X-ray absorption fine-structure spectroscopy (EXAFS), on the other hand, covers the extended part of the spectrum up to 1000 eV above the absorption edge and is sensitive to the local environment of the selected element. XAS experiments are typically performed at synchrotron facilities for their tunable energy and high intensity. The absorption spectrum is acquired by measuring either the transmitted intensity or the electron/fluorescence yield while varying the incident photon energy.

Accessing the K-edges of light elements (Li, C, O, F) typically requires XAS to operate in the soft X-ray regime (<1 keV). Depth profiling is possible by choosing between auger electron yield, total electron yield (TEY), and total fluorescence yield (TFY) mode, as indicated in **Figure 23**a. Such depth-dependency was used to study the interface chemistry of Al-substituted $Li_7La_3Zr_2O_{12}$ in contact with metal lithium electrode. When exposed to air, a layer of Li_2CO_3 is formed at the surface of the $Li_7La_3Zr_2O_{12}$ pellets as indicated by the O–K absorption signature at 534.1 eV, increasing the interfacial impedance. The strong Al-substituted $Li_7La_3Zr_2O_{12}$ signature peak at 533.0 eV observed in the TFY spectra sets the upper bound of the Li_2CO_3 layer thickness to be 100 nm. In contrast, the weak Al-substituted $Li_7La_3Zr_2O_{12}$ peak in the TEY spectra implies that the actual layer thickness is close to 10 nm (Figure 23b).[245] In a follow-up study, the authors demonstrated that, with the same air exposure, $Li_7La_3Zr_2O_{12}$ sample with smaller grain size (10–20 µm) is less prone to Li_2CO_3 formation (weaker Li_2CO_3 signature in TEY spectra) than that with larger grain size (150–200 µm).[285] That, in turn, explains the more dramatic rise in interface impedance after exposure to air observed for large-grained samples than for small-grained ones. The Li_2CO_3 layer can be removed with mechanical treatment such as surface polishing[245] or by annealing under an inert atmosphere.[286] For thin SE films, an alternative method was suggested by soaking the $Li_7La_3Zr_2O_{12}$ pellets in organic solvents containing $LiBF_4$. The Li_2CO_3 signature peaks (534.1 eV in O–K edge spectra and 290.5 eV in C–K edge spectra), built up during 3 days of air exposure, were strongly suppressed after 16 h of soaking, while the previously buried La M-edge TEY signal increased significantly.[287] The efficacy of the treatment was further confirmed

ADVANCED
SCIENCE NEWS
www.advancedsciencenews.com

ADVANCED
ENERGY
MATERIALS
www.advenergymat.de

Figure 23. Schematic of the different modes in an XAS experiment and their respective depth sensitivities a). O–K edge XAS spectra collected in TEY and TFY modes of $Li_7La_3Zr_2O_{12}$ after polished in air and in Ar glove box against the Li_2CO_3 reference b). O–K edge XAS spectra of $LiCoO_2+Li_{6.75}La_3Zr_{1.75}Ta_{0.25}O_{12}$ and $NCM+Li_{6.75}La_3Zr_{1.75}Ta_{0.25}O_{12}$ at different stages by TEY and TFY mode with reference spectra of Li_2CO_3 c). Scheme of the depth-resolved XAS concept d). Co–O interatomic distance and Debye–Waller factor for $LiCoO_2/Li_2O–Al_2O_3–P_2O_5–TiO_2$ and $LiCoO_2/NbO_2/Li_2O–Al_2O_3–P_2O_5–TiO_2$ interface observed at various PILATUS channel e). Ni L-edge XAS TFY spectra (upper image) and Ni oxidation state plots (bottom image) of NMC cathode collected at different SoC levels f). Fe L-edge XAS TEY spectra (upper image) and Fe oxidation state plots (bottom image) of the LiFePO$_4$ cathode at different electrochemical cycling and resting stages g). b) Reproduced with permission.[245] Copyright 2014, The Royal Society of Chemistry. c) Reproduced with permission.[289] Copyright 2018, American Chemical Society. d,e) Reproduced with permission.[291] Copyright 2011, The Royal Society of Chemistry. f,g) Reproduced with permission.[302] Copyright 2013, Springer-Nature.

by electrochemical impedance spectroscopy experiments, which showed an improvement of interface impedance by a factor of 8.5. An extraordinarily low interfacial resistance of $14\,\Omega\,cm^2$ was reported with the coating of MoS_2 layers on $Li_{6.5}La_3Zr_{1.5}Ta_{0.5}O_{12}$ pellet.[288] S–K edge XAS spectra connect the improvement of interfacial impedance to the formation and growth of an interlayer consisting of sulfate and sulfite, which has the additional advantage of suppressing the growth of Li-dendrite.

**ADVANCED
SCIENCE NEWS**

www.advancedsciencenews.com

**ADVANCED
ENERGY
MATERIALS**

www.advenergymat.de

The soft X-ray also probes the 2p to 3d excitations of transition metals, which are the main components for some of the most popular cathode materials. Zhang et al. studied the interfacial stability of $Li_{6.75}La_3Zr_{1.75}Ta_{0.25}O_{12}$ against commercial cathodes.[289] They found Co and Mn to be chemically stable in respectively $LiCoO_2+Li_{6.75}La_3Zr_{1.75}Ta_{0.25}O_{12}$ and $NCM+Li_{6.75}La_3Zr_{1.75}Ta_{0.25}O_{12}$ samples, as confirmed by similar TFY spectra before and after the ball-milling process (Figure 23c). Further comparison with the TEY spectra indicates that $Li_{6.75}La_3Zr_{1.75}Ta_{0.25}O_{12}$ initially covers the surface of NCM after ball-milling with a thickness between 10 and 100 nm. The thickness of the $Li_{6.75}La_3Zr_{1.75}Ta_{0.25}O_{12}$ layer is later reduced to about 10 nm after co-sintering, potentially exposing the NCM core to the formation of $LaNiO_3$ (partial oxidation of Ni from +2 to +3 state as measured from Ni L-edge TEY and TFY spectra), which is detrimental to cycle performance. Liang et al. studied the stabilizing effect of the lithium niobium oxide interlayer on ASSB with PEO-based solid polymer electrolyte and NMC cathodes.[290] The valence state of the Ni can be evaluated by the intensity ratio B/A of the double peak near the Ni L-edge. The TEY spectra without the interlayer showed a significant increase in the intensity ratio after cycling, indicating that the Ni redox was not fully reversible at the surface of the NMC particles. The TEY spectra with the interlayer coating showed a less increase in the intensity ratio and thus depicted a more reversible redox behavior. The same difference was also observed in the comparison of the TFY spectra, which led to the conclusion that the poor reversibility upon cycling occurs not only at the surface but also in the bulk of the NMC electrode.

The depth resolution can be further enhanced by analyzing the fluorescence signal as a function of the escape angle. Using the so-called depth-resolved XAS, Okumura et al. achieved an unprecedented depth resolution of 7 nm on the measurement of chemical state and local structure at the $LiCoO_2$/interlayer/$Li_2O–Al_2O_3–P_2O_5–TiO_2$ interface (Figure 23d).[291] Their findings showed that introducing the NbO_2 interlayer results in the formation of the mixture phase of $LiNbO_3$ and $LiCoO_2$, which relieved the interfacial stress caused by the volume change of $LiCoO_2$ during delithiation. A later study using the same technique claimed to have achieved a depth resolution of 3 nm.[292] It showed the stabilizing effect of the Li_3PO_4 interlayer on the electronic and local structures at the $LiCoO_2$/$80Li_2S–20P_2S_5$ interface.

By matching the experimentally observed shift of the P XAS peak with that from ab initio multiple scattering simulations, Ye et al. were able to highlight the 10% compressive stain inside $Li_{10}GeP_2S_{12}$ after holding at high voltages, as induced by mechanical constrictions.[293] This, in turn, leads to expansion of the electrochemical window of the SE from 2.1 to nearly 10 V. Other recent results include studies on the influence of Ga-[294] and Ca-substituted[295] concentration in $Li_7La_3Zr_2O_{12}$, on the surface stability of Al-substituted $Li_7La_3Zr_2O_{12}$,[296] on the chemical stability of Li_3InCl_6 electrolyte,[297] on the protective effect of Li_3PO_4 interlayer on NMC electrode against the severe side reactions with $Li_{10}GeP_2S_{12}$,[298] and on the compositional depolymerization of interconnected PS_4 tetrahedra in lithium thiophosphate solid-state electrolytes.[299]

Soft XAS typically requires an ultrahigh vacuum environment, which is why the majority of these experiments were performed ex situ. In situ electrochemistry is possible through the design of sophisticated cells.[300–303] Operando soft XAS on ASSB was first demonstrated with polymer SE against cathodes made of NMC and $LiFePO_4$ (Figure 23e,f).[302] The results provided strong evidence for the existence of a metastable phase that deviates from the commonly accepted two-phase process in the $LiFePO_4$ system. More recently, a proof-of-concept study was performed on a model ASSB system consisting of $LiCoO_2$ and $Li_{10}GeP_2S_{12}$ with $LiNbO_3$ as the interlayer.[304] XAS operating in the hard X-ray regime is more flexible in terms of sample environment but does not probe low-Z elements. Surface sensitivity and depth-profiling with hard XAS are achieved by varying the incident angle. The penetration of 18 keV X-ray is reduced from 2.4 μm to 35 nm by changing the incident angle from 3° to 0.15°. Such depth profiling was essential in demonstrating the effectiveness of annealing under the inert atmosphere on removing the Li_2CO_3 layer at the surface of $Li_7La_3Zr_2O_{12}$.[286]

4.4.2. Synchrotron X-Ray Photoelectron Spectroscopy

The tunable photon energy at the synchrotron offers depth-dependent information at buried interfaces unachievable with conventional XPS.[305–307] Hard XPS (known as HAXPES or HXPS) experiments operate at energy a few times higher than lab XPS. The high incident energy allows access to deeper core levels with additionally a larger penetration depth for bulk sensitivity (up to 50 nm). **Figure 24**a shows the scheme of HAXPES measurement principles.[307] Soft XPS (SXPS or SX-PES), on the other hand, operates at energy as low as 100 eV. Compared to lab XPS, the kinetic energy of SXPS is tunable for a given core peak, allowing for depth analysis and extreme surface sensitivity. Many of the XAS studies mentioned earlier were carried out in conjunction with synchrotron[245,286,287,296,304] and lab[285,288,290,293,297–299] XPS measurements. SXPS was used to determine the valence band structure of LiPON solid-state electrolyte commonly used in thin-film batteries.[305] It was concluded that N 2p states are responsible for the top of the valence band. As a result, the N content in LiPON layers may affect the energy band alignment with cathode materials. Liang et al. measured the Ti 1s HAXPES spectra of the $Li_{1.4}Al_{0.4}Ti_{1.6}(PO_4)_3$ electrolyte and demonstrated the effectiveness of ALD coating of Al_2O_3 against the reduction of Ti at the $Li_{1.4}Al_{0.4}Ti_{1.6}(PO_4)_3$/polysulfide interface.[306] The same group then studied the protective behavior of the Li_xSiS_y surface layer formed in situ on the surface of Li-metal (Figure 24b).[307] The composition of the layer was found to be a mixture of Li_2SiS_3, Li_4SiS_4, SiS_2 together with a small amount of Li_2S. The relative intensity ratio of Li_2S increases progressively with photon energy indicating that it is buried deeper and thus in direct contact with the Li electrode. This phenomenon, in turn, could limit the side reactions between Li and Li_3PS_4, thus preventing Li-dendrite formation and short-circuiting. In terms of operando experiments, a dedicated HAXPES setup was recently demonstrated on ASSB with $Li_{1+x+y}Al_x(Ti, Ge)_{2-x}Si_yP_{3-y}O_{12}$ SE (Figure 24c).[308] By using a model cell consisting of an $Al/LiCoO_2/Li_{1+x+y}Al_x(Ti, Ge)_{2-x}Si_yP_{3-y}O_{12}/Li_3PO_4/Li$ sandwich structure, it was shown that both Co cations and O anions from the $LiCoO_2$ electrode participated in the redox mechanism.
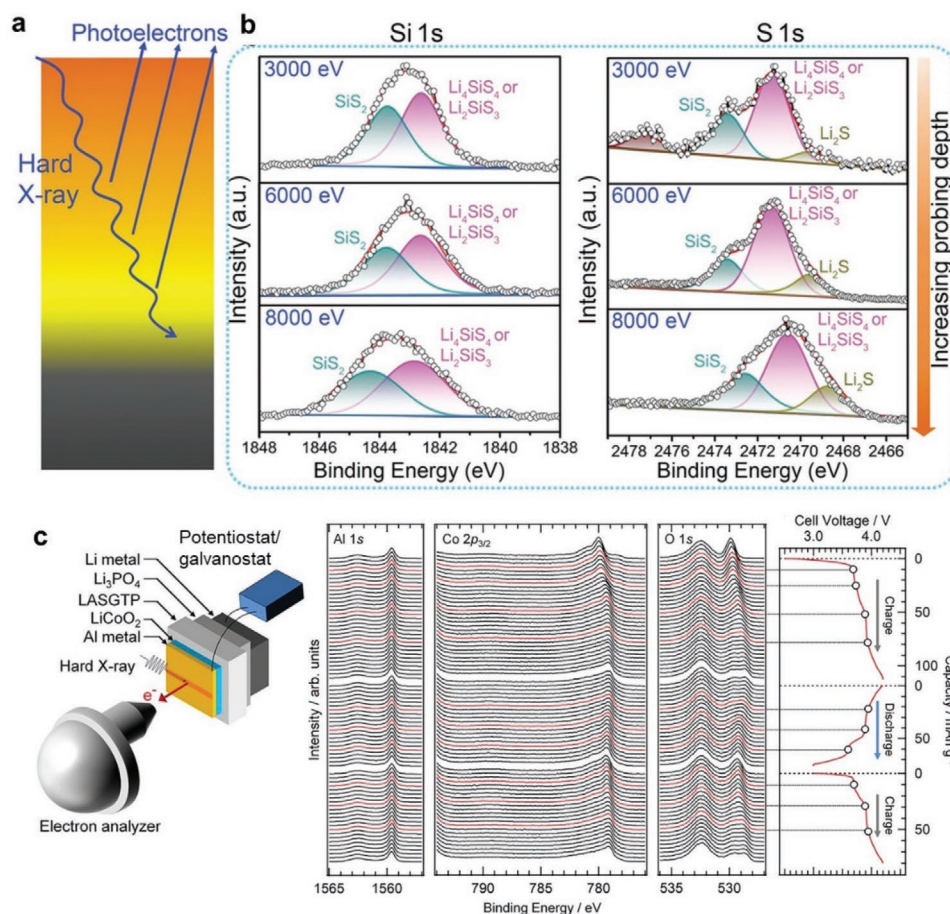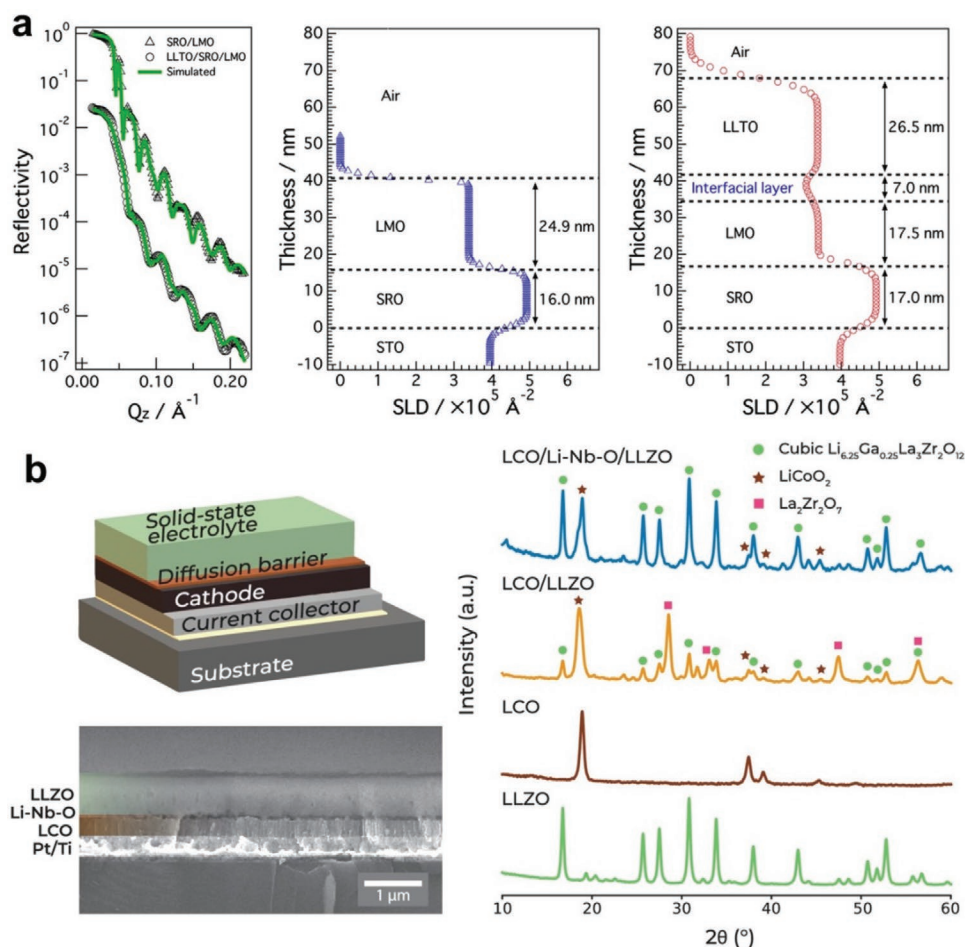
Figure 24. Schematic illustration of the evolution of the HAXPES analysis depth as a function of the photon energy a). HAXPES curves of the Li-Li$_x$SiS$_y$ electrodes at 3, 6, and 8 keV b). Schematic of the operando HAXPES setup and operando spectra of Al 1s, Co 2p3/2, and O 1s during the first charge, first discharge and second charge of the thin-film battery c). a,b) Reproduced with permission.[307] Copyright 2019, Wiley-VCH. c) Reproduced with permission.[308] Copyright 2020, Elsevier.

4.4.3. Surface and Interface X-Ray Scattering Techniques

X-ray reflectivity (XRR) is a standard technique used for the characterization of thickness, density, and roughness of surface as well as interfacial layers. It typically requires a relatively flat surface (roughness ≈1 nm). Thus, it is well suited for studies of model systems where the solid–electrolyte is epitaxially grown with thin-film deposition techniques. In a typical XRR experiment, the reflected intensity is measured as a function of the incident angle. The curve-fitting is made by calculations using Parratt's recursive formalism. XRR can be performed in the lab or at the synchrotron. The latter offers a wider dynamical range at high incident angles. Lab XRR was used to study the Li$_7$La$_3$Zr$_2$O$_{12}$ epitaxial thin films grown on (001) and (111) oriented Gd$_3$Ga$_5$O$_{12}$ substrate. The scattering length densities (SLD) extracted from the curve fitting were higher than those for polycrystalline Li$_7$La$_3$Zr$_2$O$_{12}$, indicating that a large amount of Li-ions were substituted by Al^{3+}, which results in lower Li-ion conductivities.[309] In the case of epitaxial Li$_{0.17}$La$_{0.61}$TiO$_3$/LiMn$_2$O$_4$ thin films on (111) oriented SrRuO$_3$/SrTiO$_3$ substrates, the authors were able to confirm, with lab XRR, the excellent contact between the Li$_{0.17}$La$_{0.61}$TiO$_3$ and LiMn$_2$O$_4$ films with an interfacial roughness of less than 1 nm,[310] as shown in **Figure 25**a. The SLD for the Li$_{0.17}$La$_{0.61}$TiO$_3$ and LiMn$_2$O$_4$ films were smaller than their standalone counterpart, which was attributed to a small number of oxygen defects and the diffusion of Ti ions from the Li$_{0.17}$La$_{0.61}$TiO$_3$ into the LiMn$_2$O$_4$ layer.

Another technique commonly used in surface and interface research is grazing incidence X-ray diffraction (GIXRD). The high surface sensitivity of this method is achieved with the use of a shallow incident angle. Like XRR, GIXRD also requires a rather flat surface or interface and is mostly applicable to thin-film ASSB model systems. Such a system was created for the investigation of the Li$_7$La$_3$Zr$_2$O$_{12}$/LiCoO$_2$ interface.[311,312] Figure 25b shows the schematic and cross-sectional SEM image of the multilayer thin film sample, as well as the GIXRD patterns.[311] The Li$_7$La$_3$Zr$_2$O$_{12}$/LiCoO$_2$ sample shows the presence of the La$_2$Zr$_2$O$_7$ phase, a product commonly associated with the decomposition of Li$_7$La$_3$Zr$_2$O$_{12}$ with the loss of lithium. In comparison, no extra phase was observed on the GIXRD pattern on the sample with a Nb$_2$O$_5$ interlayer, which is proof of effectiveness for this in situ lithiated diffusion barrier. Originally a synchrotron technique, GIXRD has become increasingly available thanks to the advent of a new generation of lab diffractometers. Lab GIXRD

**ADVANCED
SCIENCE NEWS**

www.advancedsciencenews.com

**ADVANCED
ENERGY
MATERIALS**

www.advenergymat.de

Figure 25. Experimental and simulated XRR spectra for LiMn$_2$O$_4$/SrRuO$_3$(111) and Li$_{0.17}$La$_{0.61}$TiO$_3$/LiMn$_2$O$_4$/SrRuO$_3$(111) films together with calculated SLD profiles of both cases a). Schematic and cross-sectional SEM image of thin-film SE/cathode stack, and the GIXRD patterns of different thin-film samples b). a) Reproduced with permission.[310] Copyright 2013, Elsevier. b) Reproduced with permission.[311] Copyright 2020, American Chemical Society.

was employed routinely to study the crystal structure of LiPON thin film separating Li$_{1.5}$Al$_{0.5}$Ge$_{1.5}$(PO$_4$)$_3$ and the Li anode,[313] of Li$_3$PO$_4$,[314] amorphous lithium lanthanum titanate,[315] Li$_{3.25}$Ge$_{0.25}$P$_{0.75}$S$_4$,[316] Li$_{1.5}$Al$_{0.5}$Ti$_{1.5}$(PO$_4$)$_3$,[317] and of a new lithium aluminate SE.[318] The high flux at the synchrotron, on the other hand, allows GIXRD to be performed well below the critical angle for total external reflection. That allows for extreme surface sensitivity (X-ray penetration depth is 5 nm at 0.25° incidence) and depth profiling by varying the grazing incident angle.[319] For example, the 2θ of the (211) and (321) Li$_7$La$_3$Zr$_2$O$_{12}$ Bragg reflections is shifted to lower values with a steeper incident angle, indicating a smaller lattice parameter at the surface than in the bulk.[286] The compressive strain at the surface is due to exposure to moisture, where the formation of Li$_2$CO$_3$ removes surface lithium in the Li$_7$La$_3$Zr$_2$O$_{12}$ lattice and replaces them with protons.

4.4.4. X-Ray Imaging Techniques

X-ray imaging encompasses many groups of techniques aiming to provide spatially resolved information of the specimen. The imaging contrast mechanism depends on the nature of the

interaction and is divided in general into two main categories, absorption and scattering, the latter of which includes refraction and diffraction. The earliest form of X-ray imaging is radiography, which makes use of the steep Z^4 variation of the absorption contrast against the atomic number. The main limitation of radiography is that it measures the projected image of the 3D object and that information along the propagation direction of the beam is convoluted. This limitation is overcome in X-ray tomography, which digitally recreates the 3D object using multiple images taken at different projection angles. Although tomography has become available with lab equipment, synchrotron offers higher energy photons necessary for penetrating thick samples. For instance, due to the heavy elements present in Li$_7$La$_3$Zr$_2$O$_{12}$, the attenuation length is less than 200 μm for a 30 keV X-ray beam. With a white beam containing >40 keV photons, Shen et al. were able to map out the porosity and texture of millimeter-thick SE pellets with a voxel size of 650 nm.[320] Their findings showed that increasing the sintering temperature from 1000 to 1150 °C increases the average grain size from 1 to 150 μm, and the relative density from 75% to 92% with no further increase observed at even higher temperatures (**Figure 26**a). The larger grain boundary of the sample
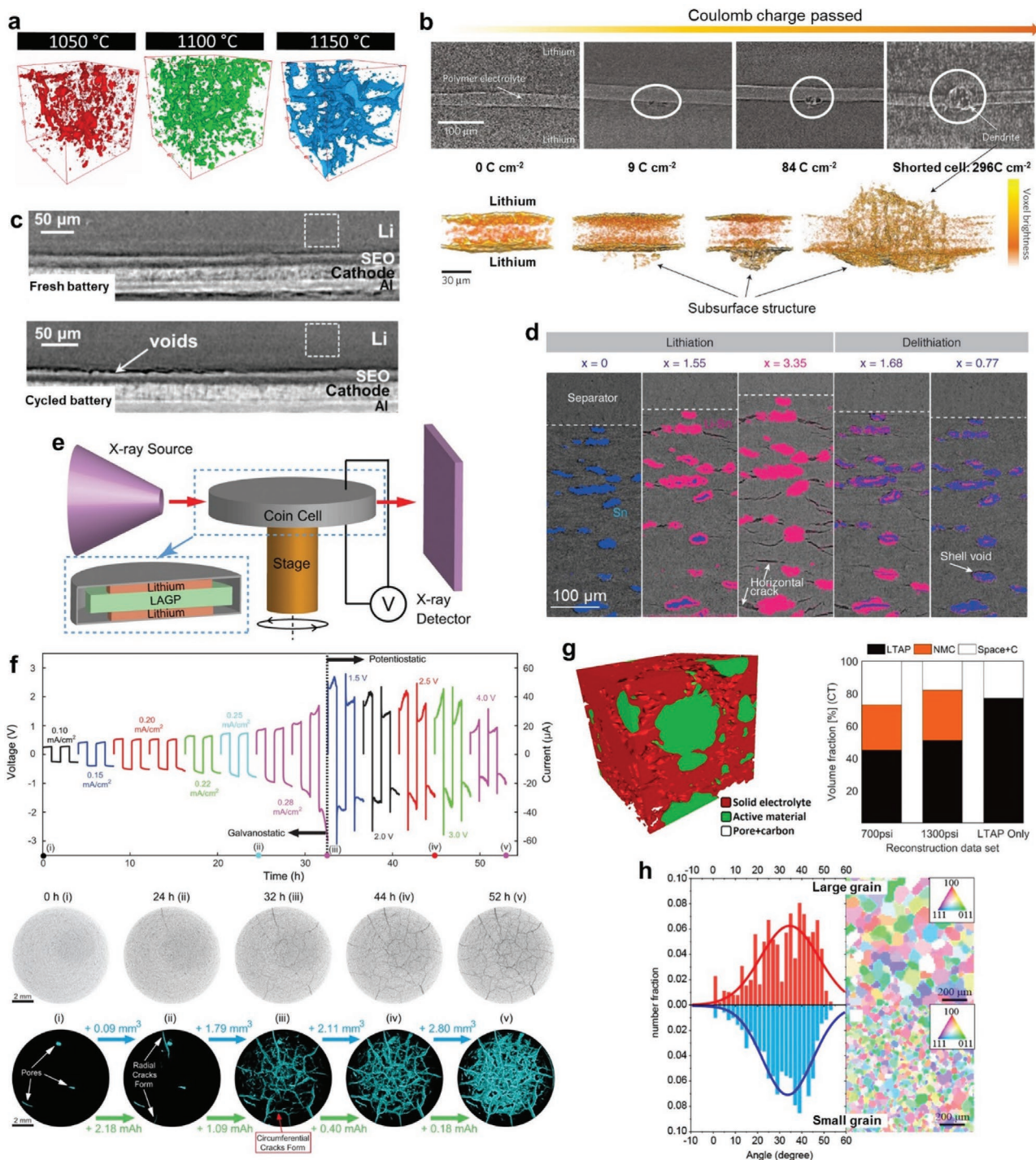
Figure 26. X-ray tomographic reconstructions of void phase in the interior of LLZO electrolytes sintered at different temperatures a). X-ray tomography slices and 3D reconstructed volumes showing the Li-symmetric cells cycled at various stages b). X-ray tomography slices showing the cross-section of Li/SEO/LiFePO$_4$ battery at fresh and cycled state c). Cross-sectional tomographic image of the Sn/Li$_2$S–P$_2$S$_5$ interface at various SoC d). In situ lab-based X-ray tomography setup for imaging SE within a symmetric Li/Li$_{1+x}$Al$_x$Ge$_{2-x}$(PO$_4$)$_3$/Li battery e). Electrochemical data, 2D tomography slices from the center of the SE pellet as well as 3D tomographs showing crack at different SoC f). 3D tomography reconstruction of a composite electrode as well as calculated volume fractions of electrode components g). Histograms of angles between grain orientation (100) direction and sample plane normal for large-grained (top) and small-grained Li$_7$La$_3$Zr$_2$O$_{12}$ (bottom) as well as their grain orientation mapping h). a) Reproduced with permission.[320] Copyright 2018, American Chemical Society. b) Reproduced with permission.[322] Copyright 2014, Springer-Nature. c) Reproduced with permission.[323] Copyright 2014, Springer-Nature. d) Reproduced with permission.[326] Copyright 2019, Wiley-VCH. e,f) Reproduced with permission.[327] Copyright 2019, American Chemical Society. g) Reproduced with permission.[328] Copyright 2018, American Chemical Society. h) Reproduced with permission.[246] Copyright 2015, American Chemical Society.

sintered at 1150 °C promotes greater pore connectivity, which facilitates lithium transport and dendrite growth. Similarly, by comparing the 3D tomography reconstruction of an ASSB made of $In/Li_{10}GeP_2S_{12}/LiCoO_2$ before and after the first charge, Zhang et al. showed that the volume expansion during the charging process helped reduce the porosity in pressurized ASSB.[321] X-ray tomography on solid polymer electrolytes does not require very high photon energies. Harry et al. studied the dendrite formation in a Li-symmetric battery with polystyrene-block-poly(ethylene oxide) copolymer (SEO) as the electrolyte. Their result revealed buried structures under the surface of Li electrodes to be the origin of the dendritic protrusions (Figure 26b), thus pointing researches on dendrite prevention to a new direction.[322] Devaux et al. studied the failure mode of ASSB with lithium-salt-doped SEO SE.[323] Dendrite formation was observed in the cycled Li-symmetric cell and deemed responsible for cell failure. Contrarily, no dendrite was detected in all eight batteries with $LiFePO_4$ cathode, cycled under the same condition. Instead, X-ray tomography in Figure 26c revealed consistently partial delamination at the Li-metal/SEO interface after cycling, which is then quantitatively correlated to the observed capacity fade.

The high photon flux at synchrotrons also enables in situ and operando experiments. In this pioneering work on an ASSB assembled with a commercially available $Li_{10}SnP_2S_{12}$ solid–electrolyte, an InLi alloy anode, and a Li_2S based composite cathode, the authors demonstrated compelling evidence of interface degradation under practical cycling conditions, despite the initial intimate contact by pressings.[324] Each tomography map took 90 s to complete, and the achieved voxel size was 2.5 μm. Seitzman et al. demonstrated an in situ synchrotron tomography measurement at relatively low X-ray energies.[325] A more recent work by Wu et al. focused on the mechanical degradation in an ASSB stack consisting of an Sn microparticle electrode pressed against amorphous $Li_2S–P_2S_5$ solid–electrolyte.[326] The degree of lithiation, calculated by analyzing the 3D reconstructed volume ratio of Sn and lithiated Sn, was higher for particles closer to the separator layer, as indicated in Figure 26d. This feature was understood as due to kinematically limited ionic transport in the solid–electrolyte across the electrode. Cracking was detected at mere 12% of SOC in $Li_2S–P_2S_5$, due to lithiation-induced volume expansion in adjacent Sn particles. The cracking propagated during further lithiation but was seemingly healed upon delithiation; the latter was attributed to the elastic behavior of $Li_2S–P_2S_5$.

In situ X-ray tomography experiment with lab instrument was first demonstrated by Tippens et al. on a symmetric $Li/Li_{1+x}Al_xGe_{2-x}(PO_4)_3/Li$ cell.[327] Figure 26e shows the in situ measurement setup and battery design. The tomographic maps (Figure 26f), taken after every 4 h of cycling, showed the formation of more and more radial cracks (one that extends from the center of the pellet to the outer edge) as the cycling progressed. The authors were able to then correlate the crack formation directly to the increase of electrochemical impedance. The battery impedance jumped from 2.81 to 6.80 $k\Omega\ cm^2$ as soon as the first fracture was detected and continued to increase as the crack network grew. Doux et al. studied the effect of stack pressure on the Li-metal anode on the dendrite formation in ASSB with Li_6PS_5Cl as the electrolyte.[90] With a carefully designed

cell capable of in situ loading, a voxel size of 1.2 μm was achieved with a commercially available X-ray microscope. An optimal pressure of 5 MPa was found, which allows for long-term cycling. Higher pressure, initially thought to be necessary for the intimate contact between the solid–electrolyte and the electrode, quickly resulted in the shorting of the cell due to dendrite growth by Li creeping. Although each tomographic map in the last two studies took a significantly longer time (30 min) to complete, commercial lab instruments are bound to become the driving force in the understanding of interfacial phenomena in the in situ cycling of ASSB thanks to their wide availability.

High-resolution imaging can be achieved by placing an X-ray objective lens downstream of the sample in what is known as a Transmission X-ray microscope (TXM). The field of view is reduced to a few hundred microns, while the spatial resolution of 25 nm is routinely achieved. The concept of TXM can also be combined with tomographic scanning to yield 3D imaging with impeccable details. This was demonstrated on a three-phase electrode designed for ASSB,[328] composed of NCM active material, $Li_{1.3}Ti_{1.7}Al_{0.3}(PO_4)_3$ as the electrolyte, and Super-P carbon as the electron conductor. The tortuosity and interface contact between the NCM and $Li_{1.3}Ti_{1.7}Al_{0.3}(PO_4)_3$ can be quantitatively analyzed in the 3D reconstructed image thanks to the spatial resolution of 58 nm (Figure 26g). It was shown that $Li_{1.3}Ti_{1.7}Al_{0.3}(PO_4)_3$ covers only 55% of the NCM particles even when pressed at 700 psi. Not much improvement was observed when the pressure was increased to 1300 psi, indicating that a much higher pressure or smaller $Li_{1.3}Ti_{1.7}Al_{0.3}(PO_4)_3$ particles are required to improve the interfacial contact. The concept of TXM-tomography can be further combined with XANES to yield spatially resolved chemical information of the specimen. The main limitation of this combined technique is the long measurement time required for performing photon energy scans at each tomographic projection. In this operando study on sulfide ASSB combining FeS_2 cathode, $Li_7P_3S_{11}$ solid–electrolyte, and Li-metal anode, Sun et al. were able to follow the propagation of the reaction front by tuning to the Fe–K edge.[329] Notably, a very heterogeneous FeS_2-core Fe-shell structure was found for the final discharged state, which is considered as one of the many factors causing the observed capacity decay. Besli et al. performed an ex situ study near the Ni–K edge on composite $LiNi_{0.8}Co_{0.15}Al_{0.05}O_2/PEO$ electrodes.[330] The 3D tomographic reconstruction with a voxel size of 32 nm showed crack network originating from the core of the $LiNi_{0.8}Co_{0.15}Al_{0.05}O_2$ cathode particles after 21 cycles while the 3D Ni oxidation state map showed an electrochemically less active core in its final charged state. A 3D SoC map was also computed using the linear relationship between Ni–K edge energy and SoC. The SoC is about 20% lower in the core compared to the maximum value found just beneath the particle surface. More recently, Kimura et al. combined X-ray tomography with XANES to achieve a low-resolution version (voxel size 3.1 μm) of the operando 3D chemical mapping on an ASSB with $LiCoO_2$ as the cathode and $Li_{2.2}C_{0.8}B_{0.2}O_3$ as the solid–electrolyte.[331] By comparing the 3D lithiated state map of two cells with different active material content, it was concluded that a highly active material loading amount (80%) results in aggravated regions of active material that are not in contact with the SE. It is worth mentioning that

**ADVANCED
SCIENCE NEWS**
www.advancedsciencenews.com

**ADVANCED
ENERGY
MATERIALS**
www.advenergymat.de

the addition of spectroscopic information in these works is key to imaging the reaction front. Conventional transmission X-ray imaging relies on the Z contrast and is thus less sensitive to the difference between materials and their lithiated counterparts.

A scanning diffraction X-ray microscope (SDXM) harnesses the diffraction contrast to achieve dark-field imaging of the specimen. Spatially resolved information, in this case, is gathered by raster scanning a focused beam across the sample surface. A SDXM typically employs a monochromatic beam and is well suited for the study of single-crystal materials. For poly-crystalline samples, Laue microdiffraction is highly recommended. In a Laue microdiffraction experiment, the detector is placed at a fixed position while the sample diffracts a focused polychromatic X-ray beam. 2D sample space is resolved by raster scanning like in an SDXM while depth profiling is possible with differential aperture techniques.[332] Laue microdiffraction was used to understand the dependence of cycling performance on surface microstructures in Al-substituted $Li_7La_3Zr_2O_{12}$ SE.[246] Figure 26h showed the X-ray Laue microdiffraction results of the Al-substituted $Li_7La_3Zr_2O_{12}$ pellets with different grain sizes. No visible difference was observed in terms of grain orientation or grain boundary misorientation between the sample with small grains and larger ones. It was thus concluded that the better cycling performance of the smaller grained sample is due to the larger surface area of the grain boundaries.

4.5. Neutron-Based Techniques

Neutron methods offer some unique opportunities in studies of ASSB, particularly for in situ and operando experiments. Neutrons interact mainly with the nuclei of the material and not with the atomic electrons. This fact leads to the following advantages: high penetration depth, nondestructive probing, sensitivity to light elements such as lithium, and isotopic contrast (e.g., ^6Li and ^7Li).[333,334] Various neutron scattering and analytical (utilizing neutron absorption) methods have been applied recently to the studies of different types of LBB.[335–337] As our review is focused on the interface phenomena in ASSB, two techniques are of particular interest, namely NR and NDP.

4.5.1. Neutron Reflectometry

NR is a powerful technique that probes near-surface structures and buried interfaces on the nanometer scale. It measures the SLD of a neutron (analog of optical density in light optics) as a function of depth perpendicular to the sample surface. For the sake of compactness, only monochromatic specular reflectometry will be considered. During specular reflectometry measurement on a monochromatic instrument, a thin well-collimated neutron beam impinges at a small grazing angle onto the sample and gets reflected. A detector records the intensity of the reflected beam as a function of the scattering angle. Above the critical angle of total external reflection, the intensity of the signal reflected from different interfaces within a sample creates an oscillating reflectivity curve with periods inversely proportional to the film thicknesses. The slope of the curve

contains information on the interface roughness. For multilayer structures, some other peculiarities, like pronounced Bragg peaks, can occur. We assume that the above-critical-angle scattering is weak. Therefore, the reflectivity can be calculated within the first Born approximation.[338]

The following is conventionally done for data analysis: with some preliminary knowledge about the sample structure, a corresponding SLD profile is taken as a guess, and a theoretical reflectivity curve is generated. The generated curve is then compared with the measured one. By appropriate curve-fitting procedure, the best match is found. Already from the SLD profile, one obtains precise determination of the thin-film or interface structure, i.e., its thickness and composition, averaged over the sample surface. Resolution of some Angstroms depending on the sample quality usually is achieved.

As a nondestructive method, NR is well suited for the in situ and ex situ characterization of surfaces and interfaces in lithium-based batteries, preferably at high flux neutron reflectometers.[339] **Figure 27**a,b shows a case study by NR toward the solid–solid interface of ASSB.[340] In the experimental design, a multilayer sample consisting of repetitive $^6LiNbO_3$(15 nm)/ Si(10 nm)/$^{nat}LiNbO_3$(15 nm)/Si(10 nm) layers were deposited to study the ^6Li and ^7Li exchange behavior during annealing at 225 °C. No change was observed concerning the position or the height of the NR Bragg peaks (both $Si/LiNbO_3$ and ^6Li/^{nat}Li interface contrasts) when the annealing time was less than 10 min (Figure 27a). As shown in Figure 27b, the height of the ^6Li/^{nat}Li isotope contrast peak decreased dramatically during prolonged annealing. Analyzed with the simulation program Parratt32,[341] this change was attributed to the mutual ^6Li and ^7Li isotope exchange. The isotope fractions are completely balanced after an annealing time of 12 h.

Up to now, NR-related techniques have not been extensively applied in investigating interfaces in ASSB. That is mainly limited by its strict sample requirements, such as the maximum thickness and surface quality. Moreover, NR measurement requires a proper sample cell, which puts additional restrictions on a practical sample design. The most broadly represented application of NR to LBB concerns the formation of SEI under liquid electrolyte. Although these studies are slightly out of the scope of our review, they are perfect for demonstrating the capabilities of NR. One of the recent examples in Figure 27c describes an operando cell design and the reflectivity profiles of a $LiMn_{1.5}Ni_{0.5}O_4$ cathode in different conditions.[342] An initial SEI layer was already formed at the cathode surface when the electrode was assembled in the full-cell, measured under the open-circuit-voltage condition. The low SLD suggested that this surficial layer is Li-enriched, as Li has a negative SLD effect. Forming the initial layer involved a direct chemical reaction with the LE. After charging (delithiation) this electrode to 4.75V, the SLD of the SEI layer showed a 1.5-fold increase. This SLD increase indicated a significant drop in lithium concentration, to a level much lower than what was found in the initial SEI. These results illustrate NR as a versatile technique for the interfacial study in batteries during (de)lithiation. In particular, NR is very sensitive to the thickness and density changes in situ. With well-prepared samples, we believe more interface-related investigations by NR will be performed in the future.
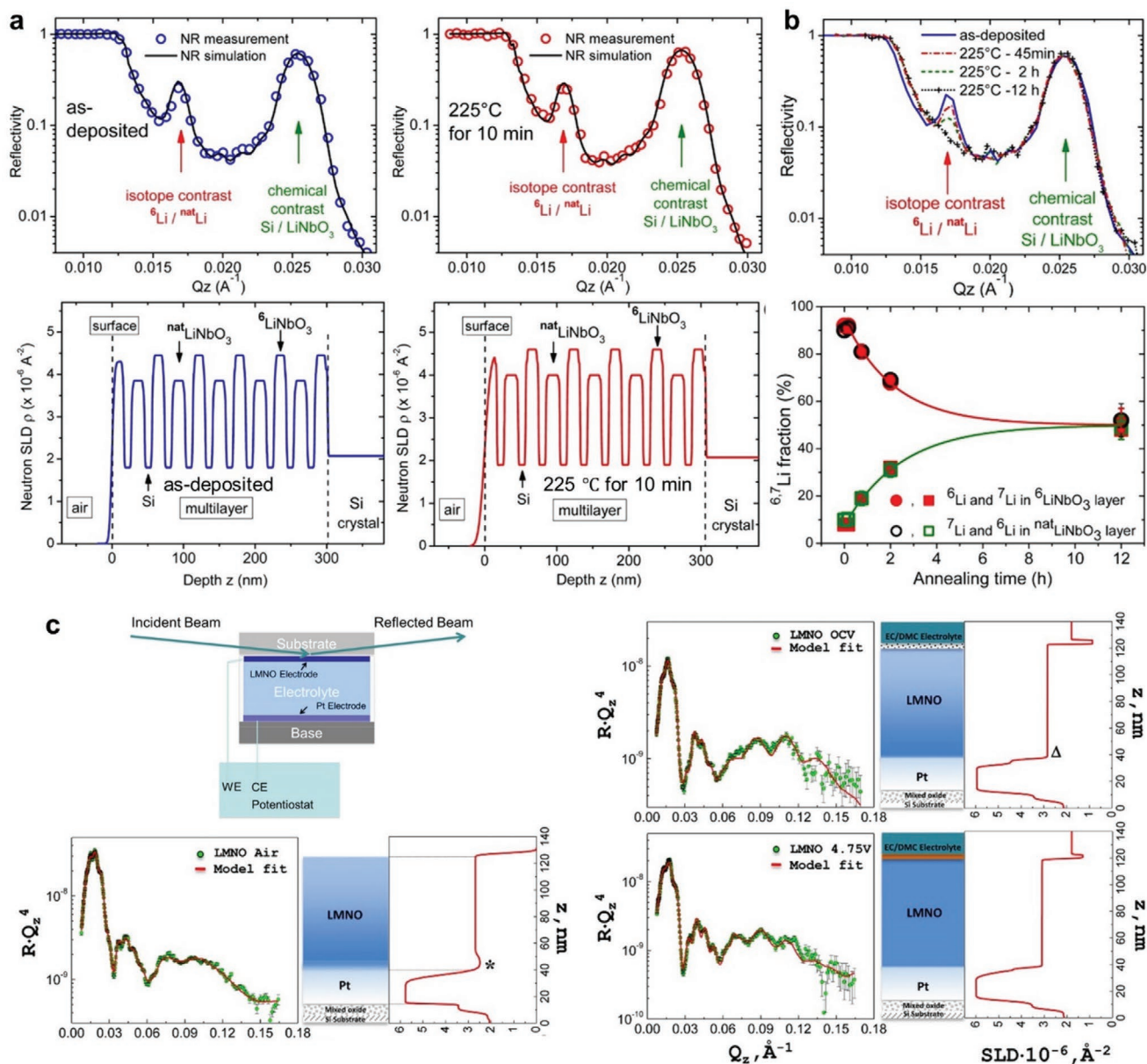
Figure 27. NR patterns and the extracted SLD curves for the multilayer sample after deposition and postannealing at 225 °C for 10 min a). Measured NR patterns for the pristine and annealed samples as well as relative ^{6}Li and ^{7}Li fractions in the ^{6}LiNbO$_3$ and ^{nat}LiNbO$_3$ layers as a function of the annealing time b). The cell design scheme for in situ NR measurement and reflectometry profiles collected for the LiMn$_{1.5}$Ni$_{0.5}$O$_4$ cathode film in different measurement conditions together with schemes representing layer changes and extracted SLD plots c). a,b) Reproduced with permission.[340] Copyright 2013, American Chemical Society. c) Reproduced with permission.[342] Copyright 2014, American Chemical Society.

4.5.2. Neutron Depth Profiling

NDP is a powerful technique capable of obtaining depth-dependent information on light elements in the near-surface of practically any substrate. Li NDP in ASSB involves the $^6Li(n,\alpha)^3H$ nuclear reaction, which occurs when neutrons interact with ^{6}Li isotopes and produce secondary charged particles (^{3}H and ^{4}He).[343] The generated particles have well-tabulated initial energies (^{3}H: 2055 keV and ^{4}He: 2727 keV) and are emitted isotropically. While penetrating through the battery layers, the particles lose energy mainly due to interactions with

atomic electrons of the host material. The amount of energy loss determines at which depth a particle was created. The ^{4}He and ^{3}H signals collected by charged particle detector(s) are directly proportional to the lithium (^{6}Li-isotope) concentration at a certain depth or in a specific battery layer. The high sensitivity of the NDP method allows quantifying the changes involved in the battery cycling process with a subminute time resolution. Because the neutron flux is relatively low, the ^{6}Li consumption is negligible. Thus, NDP is commonly considered as nondestructive, capable of in situ and operando characterization of batteries. **Figure 28**a schematically shows the NDP instrument.[4] To avoid
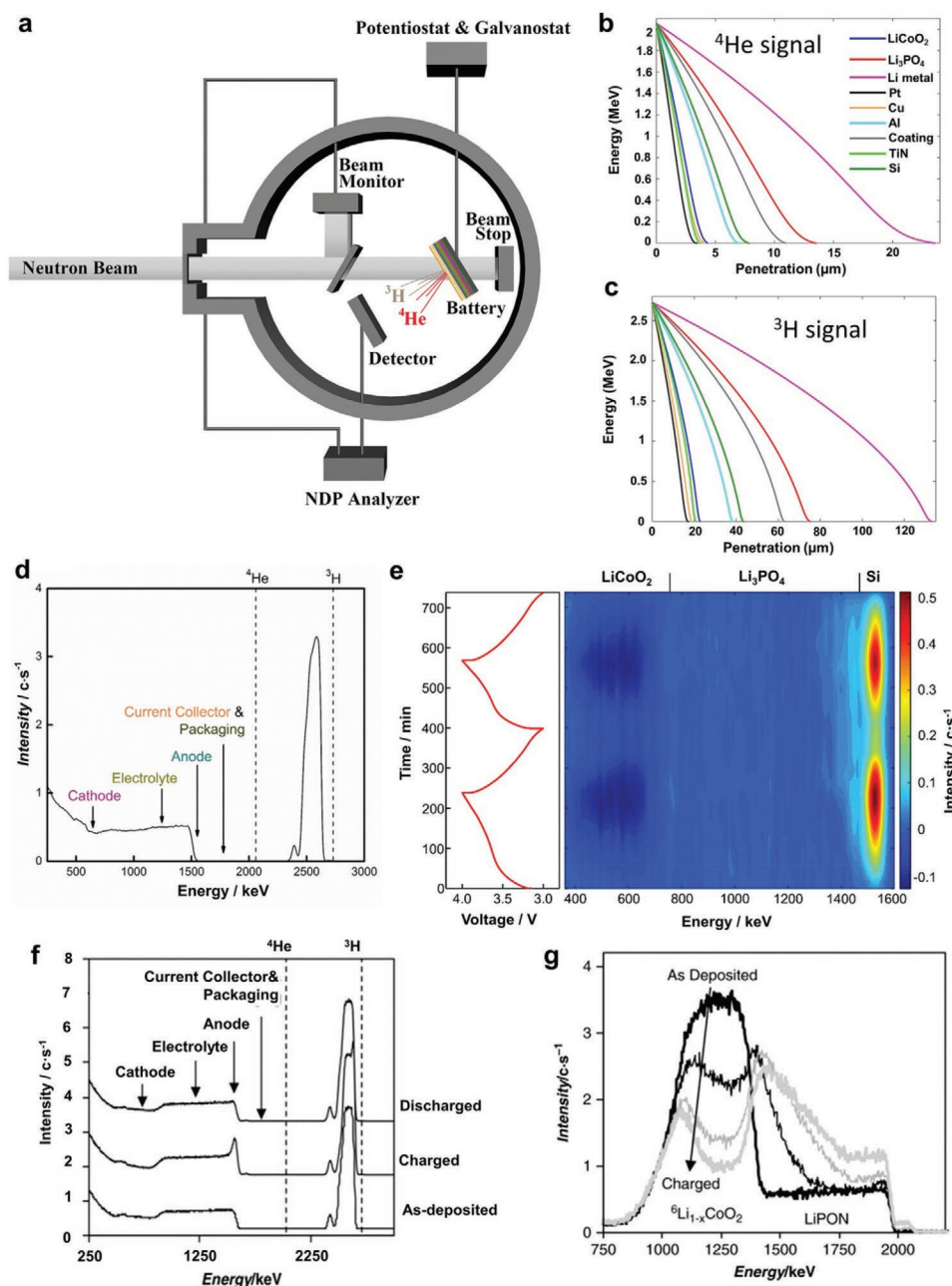
Figure 28. Schematic illustration of the NDP set-up a). Calculated relationship between the energy of alpha particles b) and tritons c) as a function of the penetration depth inside of various battery materials. NDP energy spectrum of an as-deposited, pristine, thin-film battery d). Operando differential energy spectra of the first two charging cycles of the thin-film battery e). The offset NDP energy spectra of an as-deposited Cu/LiPON/LiCoO2 battery, after first charging and discharging f). NDP spectra of a Cu/LiPON/6LiCoO2 battery at different state-of-charge g). a,d,e) Reproduced with permission.[4] Copyright 2019, Wiley-VCH. b,c) Reproduced with permission.[345] Copyright 2019, Informa UK. f,g) Reproduced with permission.[350] Copyright 2011, Wiley-VCH.

additional energy loss of charged particles in the air, the NDP measurements should be performed preferably in a vacuum atmosphere. Neutron beam goes through the thin aluminum entrance window of the sample vacuum chamber and reaches the sample. Emitted charged particles are collected within a certain solid acceptance angle by single or multiple charged particle detectors. Additionally, a standard sample with a well-defined concentration of neutron-absorbing isotope can be used for the calibration of every single measurement. A detailed description of the NDP method and a description of existing NDP facilities can be found elsewhere.[344]

The stopping power of the charged particles contains two components: the interaction with the electron clouds and the interaction with the nucleus of the target materials. Interaction with atomic electrons is the dominant source causing the energy loss in charged particles.[345] The stopping power

for heavy particles (^{4}He) is larger than that for light particles (^{3}H).[346–349] For the same particles, the heavier is the host material, the larger is the stopping power. Figure 28b,c shows the calculated relation of the energy of ^{4}He and ^{3}H as a function of the penetration depth inside various battery materials.[345] It can be seen that the ^{3}H particle has a larger penetration depth than ^{4}He. For example, the penetration depth of ^{4}He particles in Li-metal is 23.5 µm while for ^{3}H it is 133 µm. In this respect, the ^{3}H signal is more suitable for analyzing thicker samples. In contrast, the ^{4}He signal is more appropriate for higher depth resolution, e.g., for interfacial studies. Additionally, the background created during NDP measurements is proportional to the sample thickness. Therefore, the total sample thickness should always be chosen carefully for a particular case. We can estimate the battery optimal total thickness (s) as 4–5 µm for ^{4}He and 20–25 µm for ^{3}H studies. Within these thicknesses, the obtained results are quantitatively more reliable.

Thin-film ASSB is an ideal system to be investigated by NDP due to the low surface roughness and well-controlled layer thickness. Figure 28d shows the raw energy spectrum of an as-deposited battery with a configuration of Cu/Si/Li$_3$PO$_4$/LiCoO$_2$/Pt/packaging, where each individual layer and interface can be clearly identified.[4] The lithium-free Pt and packaging layers on the top also contribute to the energy losses of the emitted particles. That is why the maximal (a particle emitted from a surface) energy for both ^{4}He and ^{3}H were shifted to lower values on the energy spectrum. Depending on the available neutron flux, it usually takes minutes or even tens of seconds to collect one energy spectrum in NDP measurements, which allows for operando analysis. The lithium transport can be tracked from the differential plots by subtracting the pristine spectrum from operando spectra. Figure 28e shows the differential spectra of a Si-based thin-film battery during the first two recharging cycles.[4] It can be seen that, during charging, lithium moved out of the LiCoO$_2$ cathode and was stored in the Si anode. During discharging process, the lithium movement was reversed. The interface change was also observed, evident from the gradual formation of a lithium-enriched interlayer at the Si/Li$_3$PO$_4$ interface.

Since neutrons are absorbed by the ^{6}Li isotope (natural abundance of about 7.5%), it is advantageous to use ^{6}Li enriched materials. Figure 28f,g shows respectively the energy spectra for a Pt/LiCoO$_2$/LiPON/Cu and a Pt/^{6}LiCoO$_2$/LiPON/Cu battery with the same layer thickness and layout.[350] By comparing the energy profiles at the LiCoO$_2$ range of the two as-deposited batteries, one can see that the signal of the ^{6}Li-enriched cathode has an expected gain factor of approximately 13 times over the cathode with a natural abundance of ^{6}Li. This gain shortens the minimum time required to collect the desired spectrum, which is favorable for operando analysis. Another merit is the enhanced contrast between layers, which facilitates the observation of subtle interactions at the interface. For example, during the charging process of the Pt/^{6}LiCoO$_2$/LiPON/Cu battery, lithium will be released from the ^{6}LiCoO$_2$ cathode and be plated on the Cu (Figure 28g).[350] Interestingly, the signal decrease within the cathode, due to delithiation, is not homogeneous, with the part in contact with LiPON decreasing faster than that close to the Pt current-collector (Figure 28g). This suggests that the ionic conductivity of the cathode is the rate-limiting factor, rather than its electronic conductivity.

From the above discussion in Section 4, it can be concluded that depth-resolved techniques are highly appealing for analyzing the interfaces enclosed in ASSB. These depth-resolved techniques can efficiently determine the depth of the problematic interfaces. Moreover, it is noted that each discussed technique has its specific (dis)advantages. For the characteristics of the depth-resolved tools, the readers are kindly referred to **Table 3** for their capabilities, sample requirements, limitations, and investigated interfaces.

5. Conclusions and Outlook

ASSB, compared with conventional liquid-based LBB, are safer in operation because of the absence of flammable solvents. Due to this promising outlook, ASSB are receiving more and more attention. Intensive research efforts were devoted already to improve the ionic conductivity of SE. However, it appears that the primary hurdle for developing promising ASSB lies in the interfaces between the electrode and solid–electrolyte, rather than in the ionic conductivity of the electrolyte. Indeed, well-performing interfaces with low resistance, good (electro)chemical stability, and mechanical integrity are essential to maintain well-functioning ASSB.

The replacement of LE by SE will immensely change the behavior of LBB, and the most notable change is attributed to the interfacial properties. Interfacial differences between the two systems are found in physical and (electro)chemical aspects. From a physical point of view, LE in LBB ensure optimal contact (wetting) with all electrode particles due to the low viscosity LE that easily penetrate through micropores. Optimal physical contact between electrode and electrolyte in ASSB is a challenge because inorganic SE are rigid and inflexible. The volume change of electrodes during (de)lithiation may cause (micro)cracking, detachment, and voids in the materials or at the interface, which further aggravates physical contact problems.

Moreover, lattice-mismatch, which is present at almost all electrode/solid–electrolyte interfaces, is an additional physical factor causing high interfacial resistance. From an (electro)chemical point of view, side reactions occur at the electrode/electrolyte interface, leading to the interlayer formation. In the liquid-based LBB, the formed interlayer is called SEI, which grows onto the electrodes due to the reduction of solvents and/or Li-salts. SEI formation leads to the loss of active lithium, high internal resistance, and low coulombic efficiency. Although there is no SEI built in ASSB, various interlayers are present at the electrode/electrolyte interfaces. Based on their electronic and Li-ionic conductivity, interlayers can theoretically be grouped into four types, which behave differently during the battery operation. However, in reality, multiple types of these interlayers may be simultaneously present at a single interface in the form of, for example, lattice mismatch, elemental inter-diffusion, a space-charge layer, and a Li-immobilization interlayer. The Li-dendrites formation is a severe additional issue for ASSB, albeit it is often assumed that the majority of inorganic SE prevent Li-dendrites penetration. These interface problems cause severe performance declines, such as high internal resistance, capacity decay, or even battery failure.

**ADVANCED
SCIENCE NEWS**

www.advancedsciencenews.com

**ADVANCED
ENERGY
MATERIALS**

www.advenergymat.de

Table 3. Characteristics of depth-resolved techniques for interface analysis of ASSB.

Technique	Capability	Sample requirement	Limitation	Investigated interface
Etched-XPS	1) Element identification 2) Atomic ratio quantification 3) Chemical bonding detection	1) Thickness <5 mm 2) Size: 1×1 to 3×3 cm^2 3) Smooth surface 4) Insulator and conductor	Poor lateral resolution ($\approx 3 \, \mu m$)	Si/Li_3PO_4,[4] $Li/Li_{1.15}Y_{0.15}Zr_{1.85}(PO_4)_3$,[95] $Li/LiPON$,[205] $Li/Li_2S–P_2S_5$,[206] Li/Li_6PS_5Cl,[208] $LiCoO_2/Li_7La_3Zr_2O_{12}$[209]
ToF–SIMS	1) Elemental and molecular ion identification 2) Relatively high lateral resolution (≈ 50 nm) 3) Visualizing 3D structures	1) Thickness <10 cm. 2) Size: 1×1 to 1.2×1.2 cm^2 3) Smooth surface 4) Insulator and conductor	Low quantitative sensitivity	$LiCoO_2/Li_7La_3Zr_2O_{12}$[218]
AES	1) Element and ion identification 2) Atomic ratio quantification 3) Chemical bonding detection 4) Higher lateral resolution (≈ 10 nm)	1) Thickness below 12 cm 2) Size: 1×1 to 3×3 cm^2 3) Smooth surface 4) Only the conductor	1) Inert to chemical valence 2) The atomic detection limit of 1%	$Li_2O–B_2O_3/LiCoO_2$, [222] $LiCoO_2/Al_2O_3$,[223] Li/Li_6PS_5Cl,[224] $LiCoO_2/LiPON$,[225] $LiCoO_2/Li_6PS_5Cl$[351]
GD-OES	1) Element identification 2) Atomic ratio quantification 3) Fast sputtering rate 4) Low running cost	1) Diameter >4 mm 2) No maximum limitation in size 3) Thermally and mechanically stable 4) Insulator and conductor	1) Poor lateral resolution (≈ 1 mm) 2) Potential interelement interference	$LaPO_4/LiNi_{0.5}Co_{0.2}Mn_{0.3}O_2$[228]
LA–ICP–MS	1) Elemental identification 2) Quantitative analysis 3) Fast sputtering rate	1) Diameter <40 mm 2) Thickness <20 mm 3) Insulator and conductor	1) Poor lateral resolution ($\approx 10 \, \mu m$) 2) Possible Interelement interference	$Li_7La_3Zr_2O_{12}$ pellet[236]
LIBS	1) Element and ion identification 2) Free sample preparation 3) Sample can be solid, liquid, and gas 4) Fast analysis	1) Smooth surface 2) Insulator and conductor	1) Inert to chemical valence 2) The mass detection limit of 100 ppm	$Li/Li_{6.4}Fe_{0.2}La_3Zr_2O_{12}$[243]
ERDA	1) Element profiling	1) Smooth surface 2) Insulator and conductor	1) Expensive 2) Possible Interelement interference 3) Maximum detection depth of about 1 mm	$Pt/Li–Al–Ge–Ti–P–O$,[249] $LiCoO_2/Li–Al–Ge–Ti–P–O/Au$,[249] $Al/Au/LiCoO_2/LiPON/Si/Au$,[250] $Ti/NbO/LiPON/LiMn_2O_4/Ti$[251]
RBS	1) Impurity profiles 2) Displaced atom detection 3) Thin-film interaction or interdiffusion 4) Film density	1) Best for heavy elements on a light-element substrate 2) Smooth surface 3) Insulator and conductor	1) Expensive 2) Potential Interelement interference 3) Maximum detection depth of about 1 mm	$Pt/Li–Al–Ge–Ti–P–O$,[249] $LiCoO_2/Li–Al–Ge–Ti–P–O/Au$,[249] $Al/Au/LiCoO_2/LiPON/Si/Au$[250]
NRA	1) Element and isotope identification 2) Concentration quantification	1) Best for light elements in the heavy matrix 2) Smooth surface 3) Insulator and conductor	1) Expensive 2) Detection depth limitation of about 150 μm	$Li_{6.4}La_3Zr_{1.6}Ta_{0.4}O_{12}$ pellet[217]
PIGE	1) Light Element detection 2) Free sample preparation	1) Size: 0.5×0.5 to 50×50 mm^2 2) Thickness <5 mm 3) Insulator and conductor	Energy straggling and potential Interelement interference	$LiCoO_2/Li_{10}GeP_2S_{12}/TiS_2$[253]
PIXE	1) Element detection 2) Impurity analysis 3) Quantitative analysis 4) Free sample preparation	1) Size: 0.5×0.5 to 50×50 mm^2 2) Thickness bellow 5 mm 3) Insulator and conductor	1) Potential Interelement interference 2) Inert to Li	$LiCoO_2/Li_{10}GeP_2S_{12}/TiS_2$[253]
XAS	1) Element detection 2) Bonding environment 3) Oxidation state	Special cell design for operando measurements	Inert to Li	$Li_7La_3Zr_2O_{12}/Li$,[245,285–287] $Li_{6.5}La_3Zr_{1.5}Ta_{0.5}O_{12}/MoS_2/Li$,[288] $Li_{6.75}La_3Zr_{1.75}Ta_{0.25}O_{12}/LiCoO_2$ and $Li_{6.75}La_3Zr_{1.75}Ta_{0.25}O_{12}/NCM$,[289] $PEO–SE/NCM$,[240] $LiCoO_2/NbO_2/Li_2O–Al_2O_3–P_2O_5–TiO_2$,[291]

Table 3. Continued.

Technique	Capability	Sample requirement	Limitation	Investigated interface
				$LiCoO_2/Li_3PO_4/80Li_2S–20P_2S_5$,[292]
				$LiCoO_2/Li_3InCl_6$,[297] $Li_{10}GeP_2S_{12}/Li_3PO_4/NCM$,[298]
				$NMC/PEO–LiTFSI/Li$,[302]
				$LiFePO_4/PEO–LiTFSI/Li$,[302]
				$Li_{10}GeP_2S_{12}/LiNbO_3/LiCoO_2$[304]
Synchrotron XPS	1) Element detection 2) Chemical state	Special cell design for operando measurements	Inert to Li	$Li_7La_3Zr_2O_{12}/Li$,[245,286,287]
				$Li_{10}GeP_2S_{12}/LiNbO_3/LiCoO_2$,[304]
				$Li_{1.4}Al_{0.4}Ti_{1.6}(PO_4)_3/Al_2O_3/PEO$,[306]
				Li_3PS_4/Li,[307]
				$Al/LiCoO_2/Li_{1+x+y}Al_x(Ti,Ge)_{2−x}Si_yP_{3−y}O_{12}/Li_3PO_4/Li$[308]
XRR	Thickness, density, and roughness of the surface and interface layers	Smooth surface	No element sensitivity	$Li_7La_3Zr_2O_{12}/Gd_3Ga_5O_{12}$,[309]
				$Li_{0.17}La_{0.61}TiO_3/LiMn_2O_4/SrRuO_3/SrTiO_3$[310]
GIXRD	Crystal structure and strain in surface and interface layers	Smooth surface	No element sensitivity	$Li_7La_3Zr_2O_{12}/LiCoO_2$,[311,312]
				$Li_{1.5}Al_{0.5}Ge_{1.5}(PO_4)_3–PEO/LiPON/Li$[313]
X-ray imaging	1) Reconstruction of 3D volume 2) Elemental sensitivity (+XANES) 3) Oxidation state (+XANES) 4) Strain visualization	None	Inert to Li	$Li/Li_6PS_5Cl/Li$,[90]
				$In/Li_{10}GeP_2S_{12}/LiCoO_2$,[321] $Li/SEO/Li$,[322]
				$LiFePO_4/SEO/Li$,[323]
				$InLi/Li_{10}SnP_2S_{12}/Li_2S$,[324]
				$Li/Li_3PS_4/Li$,[325]
				$Sn/Li_2S–P_2S_5$,[326]
				$Li/Li_{1+x}Al_xGe_{2−x}(PO_4)_3/Li$,[327]
				$NCM/Li_{1.3}Ti_{1.7}Al_{0.3}(PO_4)_3/carbon$,[328]
				$Li_7P_3S_{11}/FeS_2$,[329]
				$LiNi_{0.8}Co_{0.15}Al_{0.05}O_2/PEO$,[330]
				$LiCoO_2/Li_{2.2}C_{0.8}B_{0.2}O_3$[331]
NR	Thickness, density, and roughness of the surface and interface layers	1) Thickness: 10–5000 Å 2) Area ≥100 mm^2 3) Smooth surface 4) Roughness <10Å	Need high neutron flux	$^6LiNbO_3/Si/^{nat}LiNbO_3/Si$[292]
NDP	1) Dynamic detection of Li-ions 2) Detecting Interlayer formation	1) Thin samples: 4–5 µm (^{4}He), 20–25 µm (^{3}H) 2) Well stoichiometric 3) Roughness <10 nm	1) Under vacuum 2) Detection depth <150 µm.	$Si/Li_3PO_4/LiCoO_2$,[4]
				$Cu/LiPON/LiCoO_2$,[350]
				$Cu/LiPON/^6LiCoO_2$,[350]
				$Li/Li_7La_3Zr_2O_{12}$,[352]
				$Ti/NbO/LiPON/LiMn_2O_4/Ti$[353]

Various strategies have been developed to mitigate interface problems for ASSB. For example, applying optimal stack pressure, applying solid–electrolyte mixed electrodes, or "zero-strain" electrodes can help to accomplish and maintain optimal contact between bulk-type electrodes and inorganic SE. Using electrode/electrolyte materials with similar lattice structure often alleviates the lattice-mismatch-induced interfacial resistance. Another way to solve this issue is by depositing epitaxial coatings or buffer layers. Adding a thin buffer layer between the electrode and solid electrolyte is also an advanced approach to suppress Li-dendrites, interdiffusion, and space-charge layers. A few materials, in a thickness-range from a few nanometers to micrometers, were reported to be suitable buffer layer candidates. This field is still not sufficiently explored. Further research is highly demanded, especially for the working principles, optimal thickness, and material selection of buffer layers. Compared to the conventional experimental methods, machine learning is greatly promising in searching for excellent buffer layer materials. Hopefully, further studies on machine learning methods, in combination with experiments, will facilitate interfacial tailoring for ASSB.

It should be noted that interlayers are not always detrimental to ASSB. Under certain circumstances, interlayer formation leads to more stable interfaces. For example, Li-metal is a highly reactive anode material, which reacts with most inorganic-SE upon direct contact, forming an interlayer. This interlayer formation can consume Li-dendrites during penetration through the solid–electrolyte layer, avoiding battery shorting. However, only interlayers with high Li-ionic conductivity and low electronic conductivity are desirable due to their relatively high cycling stability. Future work should focus on exploring appropriate inorganic SE materials that form an effective interlayer with Li-metal. Apart from dendrite consumption in the interlayer, other methods can also be used to obtain dendrite-free Li-metal ASSB. Applying an optimal stack pressure, depositing thin buffer layers, and exploring 3D Li-metal anodes is helpful for this purpose. Developing high-purity SE and using hybrid or composite SE with flexible components is a complementary approach.

In fact, most of the formed interlayers in ASSB are unfavorable. Understanding interlayer formation mechanisms is crucial to sort out solutions for interfacial tailoring. This assignment requires interface-sensitive or depth-resolved characterization tools. A variety of techniques capable of analyzing interfaces in ASSB has been reviewed in the present paper. Their capabilities, advantages, and limitations have been discussed in detail and are

	Physical contact	Dendrite issue	Lattice mismatch	Inter-diffusion	Space charge	Li-immobilization	Depth resolution	Element detection	Non-destructive
Etched-XPS							10nm	Li to U	
ToF-SIMS							2nm	H to U	
AES							2nm	Li to U	
SAM							Cross-section	Li to U	
GD-OES							20nm	H to U	
LA-ICP-MS							50nm	Li to U	
LIBS							20-100nm	H to U	
ERDA							10-20nm	H to U	
RBS							5-20nm	B to U	
PIGE							20-50nm	Li to Al	
PIXE							20-50µm	Al to U	
NRA							50-100nm	H to F	
TEM-EELS							Cross-section	Li to U	
EH							Cross-section	No	
Cryo-EM							Cross-section	No	
XAS							3-20nm	C to U	
Synchrotron XPS								C to U	
XRR & GIXRD							1nm	No	
X-ray imaging			µ-Laue				20-500nm	C to U	
NR							1nm	No	
NDP							10-50nm	^{6}Li	

Low ——————▶ High

Figure 29. Capability map of the interface sensitive techniques. The light-green color and the dark-green color in the figure indicate low and high capability, respectively.

summarized in a "capability map', which is shown in **Figure 29**. The capability map assists researchers in selecting appropriate measurement methods for their encountered interfacial issues. It should be kept in mind that no single technique is so universal that it can acquire all the desired information. For example, IBA, synchrotron X-ray, and neutron-related techniques offer nondestructive measurements for analyzing interfaces in ASSB, enabling operando or in situ characterizations. However, IBA, NR, and NDP are not sensitive to lattice information. Therefore, these techniques cannot be used to investigate any interface phenomena related to crystal structure changes. In this regard, synchrotron X-ray based techniques are more applicable.

Nevertheless, synchrotron X-ray is not sensitive to light-weight lithium. Therefore, it is not suitable for monitoring the locations of immobilized Li-ions. The etching-based depth profiling techniques, including XPS, ToF-SIMS, AES, GD-OES, LA–ICP–MS, and LIBS can detect lithium, as well as a wide range of other elements. Among these etching-based depth profiling techniques, interface analysis by GD-OES, LA–ICP–MS, and LIBS are relatively cheap, fast, and easy for sample preparation. However, all the etching-based measurements are destructive for the samples to be analyzed. Transmission electron microscopy electron energy loss spectroscopy (TEM–EELS) and EH can also be used in operando and in situ investigation of interfaces in ASSB, like IBA, NR, and NDP. However, special thin-film nanobatteries (thickness <100 nm) are required for these measurements. The methods summarized in Figure 29 should usually be combined to understand the complicated processes at the interface fully.

During the literature survey, it was quickly recognized that many interface-resolved techniques, e.g., GD-OES, LA–ICP–MS, and LIBS, are still not widely employed for interface investigations in ASSB. Moreover, some of the large measurement platforms, such as IBA, synchrotron X-ray, and neutron based techniques, are hosted by specific institutes or scientific centers. Therefore, the authors hope that the present review can inspire other researchers to collaborate and coherently use these techniques for interface studies in the future.

Acknowledgements

Conflict of Interest

The authors declare no conflict of interest.

Keywords

**ADVANCED
SCIENCE NEWS**

www.advancedsciencenews.com

**ADVANCED
ENERGY
MATERIALS**

www.advenergymat.de

[1] M. Armand, J.-M. Tarascon, *Nature* **2008**, *451*, 652.

[2] D. C. Lin, Y. Y. Liu, Y. Cui, *Nat. Nanotechnol.* **2017**, *12*, 194.

[3] J. B. Goodenough, K.-S. Park, *J. Am. Chem. Soc.* **2013**, *135*, 1167.

[4] C. Chen, J. F. M. Oudenhoven, D. L. Danilov, E. Vezhlev, L. Gao, N. Li, F. M. Mulder, R.-A. Eichel, P. H. L. Notten, *Adv. Energy Mater.* **2018**, *8*, 201801430.

[5] P. H. L. Notten, F. Roozeboom, R. A. H. Niessen, L. Baggetto, *Adv. Mater.* **2007**, *19*, 4564.

[6] J. F. M. Oudenhoven, L. Baggetto, P. H. L. Notten, *Adv. Energy Mater.* **2011**, *1*, 10.

[7] A. Pearse, T. Schmitt, E. Sahadeo, D. M. Stewart, A. Kozen, K. Gerasopoulos, A. A. Talin, S. B. Lee, G. W. Rubloff, K. E. Gregorczyk, *ACS Nano* **2018**, *12*, 4286.

[8] L. Yue, J. Ma, J. Zhang, J. Zhao, S. Dong, Z. Liu, G. Cui, L. Chen, *Energy Storage Mater.* **2016**, *5*, 139.

[9] H. Zhang, C. Li, M. Piszcz, E. Coya, T. Rojo, L. M. Rodriguez-Martinez, M. Armand, Z. Zhou, *Chem. Soc. Rev.* **2017**, *46*, 797.

[10] V. Thangadurai, S. Narayanan, D. Pinzaru, *Chem. Soc. Rev.* **2014**, *43*, 4714.

[11] C. Wang, K. Fu, S. P. Kammampata, D. W. McOwen, A. J. Samson, L. Zhang, G. T. Hitz, A. M. Nolan, E. D. Wachsman, Y. Mo, V. Thangadurai, L. Hu, *Chem. Rev.* **2020**, *120*, 4257.

[12] Z. Jian, Y.-S. Hu, X. Ji, W. Chen, *Adv. Mater.* **2017**, *29*, 1601925.

[13] M. Hou, F. Liang, K. Chen, Y. Dai, D. Xue, *Nanotechnology* **2020**, *31*, 132003.

[14] P.-J. Lian, B.-S. Zhao, L.-Q. Zhang, N. Xu, M.-T. Wu, X.-P. Gao, *J. Mater. Chem. A* **2019**, *7*, 20540.

[15] Q. Zhang, D. Cao, Y. Ma, A. Natan, P. Aurora, H. Zhu, *Adv. Mater.* **2019**, *31*, 1901131.

[16] S. Chen, D. Xie, G. Liu, J. P. Mwizerwa, Q. Zhang, Y. Zhao, X. Xu, X. Yao, *Energy Storage Mater.* **2018**, *14*, 58.

[17] E. Masdupuy, *Ann. Chim.* **1948**, *2*, 1527.

[18] C. C. Liang, J. Epstein, G. H. Boyle, *J. Electrochem. Soc.* **1969**, *116*, 1452.

[19] D. E. Fenton, J. M. Parker, P. V. Wright, *Polymer* **1973**, *14*, 589.

[20] C. C. Liang, *J. Electrochem. Soc.* **1973**, *120*, 1289.

[21] H. Y.-P. Hong, *Mater. Res. Bull.* **1978**, *13*, 117.

[22] M. Watanabe, M. Kanba, H. Matsuda, K. Tsunemi, K. Mizoguchi, E. Tsuchida, I. Shinohara, *Makromol. Chem., Rapid Commun.* **1981**, *2*, 741.

[23] R. Mercier, J.-P. Malugani, B. Fahys, G. Robert, *Solid State Ionics* **1981**, *5*, 663.

[24] J. E. Weston, B. C. H. Steele, *Solid State Ionics* **1981**, *2*, 347.

[25] J. E. Weston, B. C. H. Steele, *Solid State Ionics* **1982**, *7*, 75.

[26] T. Iijima, Y. Toyoguchi, N. Eda, *Denki Kagaku* **1985**, *53*, 619.

[27] J. H. Kennedy, Y. Yang, *J. Electrochem. Soc.* **1986**, *133*, 2437.

[28] H. Aono, E. Sugimoto, Y. Sadaoka, N. Imanaka, G. Adachi, *Solid State Ionics* **1990**, *40–41*, 38.

[29] J. B. Bates, N. J. Dudney, G. R. Gruzalski, R. A. Zuhr, A. Choudhury, C. F. Luck, J. D. Robertson, *Solid State Ionics* **1992**, *53–56*, 647.

[30] Y. Inaguma, L. Chen, M. Itoh, T. Nakamura, T. Uchida, H. Ikuta, M. Wakihara, *Solid State Ionics* **1993**, *86*, 689.

[31] R. Kanno, T. Hata, Y. Kawamoto, M. Irie, *Solid State Ionics* **2000**, *130*, 97.

[32] V. Thangadurai, H. Kaack, W. J. F. Weppner, *J. Am. Ceram. Soc.* **2003**, *86*, 437.

[33] R. Murugan, V. Thangadurai, W. Weppner, *Angew. Chem., Int. Ed.* **2007**, *46*, 7778.

[34] H.-J. Deiseroth, S.-T. Kong, H. Eckert, J. Vannahme, C. Reiner, T. Zaiβ, M. Schlosser, *Angew. Chem., Int. Ed.* **2008**, *47*, 755.

[35] N. Kamaya, K. Homma, Y. Yamakawa, M. Hirayama, R. Kanno, M. Yonemura, T. Kamiyama, Y. Kato, S. Hama, K. Kawamoto, A. Mitsui, *Nat. Mater.* **2011**, *10*, 682.

[36] Y. Zhao, L. L. Daemen, *J. Am. Chem. Soc.* **2012**, *134*, 15042.

[37] L. Xu, S. Tang, Y. Cheng, K. Wang, J. Liang, C. Liu, Y.-C. Cao, F. Wei, L. Mai, *Joule* **2018**, *2*, 1991.

[38] D. H. S. Tan, A. Banerjee, Z. Chen, Y. S. Meng, *Nat. Nanotechnol.* **2020**, *15*, 170.

[39] Z. Ding, J. Li, J. Li, C. An, *J. Electrochem. Soc.* **2020**, *167*, 070541.

[40] A. M. Tripathi, W.-N. Su, B. J. Hwang, *Chem. Soc. Rev.* **2018**, *47*, 736.

[41] A. Banerjee, X. Wang, C. Fang, E. A. Wu, Y. S. Meng, *Chem. Rev.* **2020**, *120*, 6878.

[42] P. P. R. M. L. Harks, F. M. Mulder, P. H. L. Notten, *J. Power Sources* **2015**, *288*, 92.

[43] J. C. Bachman, S. Muy, A. Grimaud, H.-H. Chang, N. Pour, S. F. Lux, O. Paschos, F. Maglia, S. Lupart, P. Lamp, L. Giordano, Y. Shao-Horn, *Chem. Rev.* **2016**, *116*, 140.

[44] D. L. WoodIII, J. Li, C. Daniel, *J. Power Sources* **2015**, *275*, 234.

[45] D. H. Jeon, *Energy Storage Mater.* **2019**, *18*, 139.

[46] X. Yao, B. Huang, J. Yin, G. Peng, Z. Huang, C. Gao, D. Liu, X. Xu, *Chin. Phys. B* **2016**, *25*, 018802.

[47] J. Janek, W. G. Zeier, *Nat. Energy* **2016**, *1*, 16141.

[48] E. Peled, S. Menkin, *J. Electrochem. Soc.* **2017**, *126*, A1703.

[49] N. Kotak, P. Barai, A. Verma, A. Mistry, P. P. Mukherjee, *J. Electrochem. Soc.* **2018**, *165*, A1064.

[50] C. Chen, T. Zhou, D. L. Danilov, L. Gao, S. Benning, N. Schön, S. Tardif, H. Simons, F. Hausen, T. U. Schülli, R.-A. Eichel, P. H. L. Notten, *Nat. Commun.* **2020**, *11*, 3283.

[51] E. Peled, *J. Electrochem. Soc.* **1979**, *126*, 2047.

[52] S. Benning, C. Chen, R.-A. Eichel, P. H. L. Notten, F. Hausen, *ACS Appl. Energy Mater.* **2019**, *2*, 6761.

[53] A. Wang, S. Kadam, H. Li, S. Shi, Y. Qi, *npj Comput. Mater.* **2018**, *4*, 15.

[54] S. Liu, D. Liu, S. Wang, X. Cai, F. Kang, B. Li, *J. Mater. Chem. A* **2019**, *7*, 12993.

[55] X. Shen, R. Zhang, X. Chen, X. Cheng, X. Li, Q. Zhang, *Adv. Energy Mater.* **2010**, *10*, 1903645.

[56] F. Shi, A. Pei, D. T. Boyle, J. Xie, X. Yun, X. Zhang, Y. Cui, *Proc. Natl. Acad. Sci. USA* **2018**, *115*, 8529.

[57] D. Li, D. Danilov, Z. Zhang, H. Chen, Y. Yang, P. H. L. Notten, *J. Electrochem. Soc.* **2015**, *162*, A858.

[58] C. Chen, D. Li, L. Gao, P. P. R. M. L. Harks, R.-A. Eichel, P. H. L. Notten, *J. Mater. Chem. A* **2017**, *5*, 1428.

[59] D. Li, D. Danilov, L. Gao, Y. Yang, P. H. L. Notten, *Electrochim. Acta* **2016**, *210*, 445.

[60] C. Zhan, T. Wu, J. Lu, K. Amine, *Energy Environ. Sci.* **2018**, *11*, 243.

[61] C. Xu, B. Sun, T. Gustafsson, K. Edström, D. Brandell, M. Hahlin, *J. Mater. Chem. A* **2014**, *2*, 7256.

[62] J. Xiao, *Science* **2019**, *366*, 426.

[63] K. N. Wood, E. Kazyak, A. F. Chadwick, K.-H. Chen, J.-G. Zhang, K. Thornton, N. P. Dasgupta, *ACS Cent. Sci.* **2016**, *2*, 790.

[64] P. Hundekar, R. Jain, A. S. Lakhnot, N. Koratkar, *J. Appl. Phys.* **2020**, *128*, 010903.

[65] C. Monroe, J. Newman, *J. Electrochem. Soc.* **2005**, *152*, A396.

[66] C.-L. Tsai, V. Roddatis, C. V. Chandran, Q. Ma, S. Uhlenbruck, M. Bram, P. Heitjans, O. Guillon, *ACS Appl. Mater. Interfaces* **2016**, *8*, 10617.

[67] J. Kasemchainan, S. Zekoll, D. S. Jolly, Z. Ning, G. O. Hartley, J. Marrow, P. G. Bruce, *Nat. Mater.* **2019**, *18*, 1105.

[68] J. Newman, *Trans. Faraday Soc.* **1965**, *61*, 2229.

[69] J. Marcicki, A. T. Conlisk, G. Rizzoni, *J. Power Sources* **2014**, *251*, 157.

[70] J. Lück, A. Latz, *Phys. Chem. Chem. Phys.* **2019**, *21*, 14753.

[71] X. Feng, M. Ouyang, X. Liu, L. Lu, Y. Xia, X. He, *Energy Storage Mater.* **2018**, *10*, 246.

[72] X. Feng, D. Ren, X. He, M. Ouyang, *Joule* **2020**, *4*, 743.

[73] Z. Liao, S. Zhang, K. Li, G. Zhang, T. G. Habetler, *J. Power Sources* **2019**, *436*, 226879.

[74] L. H. J. Raijmakers, R.-A. Eichel, P. H. L. Notten, *Appl. Energy* **2019**, *240*, 918.

ADVANCED
SCIENCE NEWS

www.advancedsciencenews.com

ADVANCED
ENERGY
MATERIALS

www.advenergymat.de

[75] R. Chen, A. M. Nolan, J. Lu, J. Wang, X. Yu, Y. Mo, L. Chen, X. Huang, H. Li, *Joule* **2020**, *4*, 812.

[76] T. Inoue, K. Mukai, *ACS Appl. Mater. Interfaces* **2017**, *9*, 1507.

[77] J. Sakamoto, *Nat. Energy* **2019**, *4*, 827.

[78] B. Wu, S. Wang, W. J. EvansIV, D. Z. Deng, J. Yang, J. Xiao, *J. Mater. Chem. A* **2016**, *4*, 15266.

[79] A. C. Luntz, J. Voss, K. Reuter, *J. Phys. Chem. Lett.* **2015**, *6*, 4599.

[80] R.-J. Chen, Y.-B. Zhang, T. Liu, B.-Q. Xu, Y.-H. Lin, C.-W. Nan, Y. Shen, *ACS Appl. Mater. Interfaces* **2017**, *9*, 9654.

[81] H.-G. Tian, Y. Qi, *J. Electrochem. Soc.* **2017**, *164*, E3512.

[82] D. Cao, X. Sun, Q. Li, A. Natan, P. Xiang, H. Zhu, *Matter* **2020**, *3*, 57.

[83] C. Ma, K. Chen, C. D. Liang, C.-W. Nan, R. Ishikawa, K. More, M. F. Miao, *Energy Environ. Sci.* **2014**, *7*, 1638.

[84] A. Sakuda, A. Hayashi, M. Tatsumisago, *Chem. Mater.* **2010**, *22*, 949.

[85] Z. Y. Wang, D. Santhanagopalan, W. Zhang, F. Wang, H. L. Xin, K. He, J. C. Li, N. Dudney, Y. S. Meng, *Nano Lett.* **2016**, *16*, 3760.

[86] D. Santhanagopalan, D. N. Qian, T. McGilvray, Z. Y. Wang, F. Wang, F. Camino, J. Graetz, N. Dudney, Y. S. Meng, *J. Phys. Chem. Lett.* **2014**, *5*, 298.

[87] K. Yamamoto, Y. Iriyama, T. Asaka, T. Hirayama, H. Fujita, C. A. Fisher, K. Nonaka, Y. Sugita, Z. Ogumi, *Angew. Chem., Int. Ed.* **2010**, *49*, 4414.

[88] J. Haruyama, K. Sodeyama, L. Y. Han, K. Takada, Y. Tateyama, *Chem. Mater.* **2014**, *26*, 4248.

[89] X. Zhang, Q. J. Wang, K. L. Harrison, S. A. Roberts, S. J. Harris, *Cell Rep. Phys. Sci.* **2020**, *1*, 100012.

[90] J.-M. Doux, H. Nguyen, D. H. S. Tan, A. Banerjee, X. Wang, E. A. Wu, C. Jo, H. Yang, Y. S. Meng, *Adv. Energy Mater.* **2020**, *10*, 1903253.

[91] X. Chen, W. He, L.-X. Ding, S. Wang, H. Wang, *Energy Environ. Sci.* **2019**, *12*, 938.

[92] J. Wang, H. Wang, J. Xie, A. Yang, A. Pei, C.-L. Wu, F. Shi, Y. Liu, D. Lin, Y. Gong, Y. Cui, *Energy Storage Mater.* **2018**, *14*, 345.

[93] X. Fu, D. Yu, J. Zhou, S. Li, X. Gao, Y. Han, P. Qi, X. Feng, B. Wang, *CrystEngComm* **2016**, *18*, 4236.

[94] R. Koerver, W. Zhang, L. de Biasi, S. Schweidler, A. O. Kondrakov, S. Kolling, T. Brezesinski, P. Hartmann, W. G. Zeier, J. Janek, *Energy Environ. Sci.* **2018**, *11*, 2142.

[95] S. Wang, H. Xu, W. Li, A. Dolocan, A. Manthiram, *J. Am. Chem. Soc.* **2018**, *140*, 250.

[96] F. Han, A. S. Westover, J. Yue, X. Fan, F. Wang, M. Chi, D. N. Leonard, N. J. Dudney, H. Wang, C. Wang, *Nat. Energy* **2019**, *4*, 187.

[97] Y. Ren, Y. Shen, Y. Lin, C.-W. Nan, *Electrochem. Commun.* **2015**, *57*, 27.

[98] M. J. Wang, R. Choudhury, J. Sakamoto, *Joule* **2019**, *3*, 2165.

[99] J. Duan, W. Wu, A. M. Nolan, T. Wang, J. Wen, C. Hu, Y. Mo, W. Luo, Y. Huang, *Adv. Mater.* **2019**, *31*, 1807243.

[100] J. Peng, L.-N. Wu, J.-X. Lin, C.-G. Shi, J.-J. Fan, L.-B. Chen, P. Dai, L. Huang, J.-T. Li, S.-G. Sun, *J. Mater. Chem. A* **2019**, *7*, 19565.

[101] Z. Zhang, L. Zhang, Y. Liu, T. Yang, Z. Wang, X. Yan, C. Yu, *J. Mater. Chem. A* **2019**, *7*, 23173.

[102] W. Zhou, S. Wang, Y. Li, S. Xin, A. Manthiram, J. B. Goodenough, *J. Am. Chem. Soc.* **2016**, *138*, 9385.

[103] D. Li, L. Chen, T. Wang, L.-Z. Fan, *ACS Appl. Mater. Interfaces* **2018**, *10*, 7069.

[104] J. Chai, B. Chen, F. Xian, P. Wang, H. Du, J. Zhang, Z. Liu, H. Zhang, S. Dong, X. Zhou, G. Cui, *Small* **2018**, *14*, 1802244.

[105] S. Zekoll, C. Marriner-Edwards, A. K. Ola Hekselman, J. Kasemchainan, C. Kuss, D. E. J. Armstrong, D. Cai, R. J. Wallace, F. H. Richter, J. H. J. Thijssen, P. G. Bruce, *Energy Environ. Sci.* **2018**, *11*, 185.

[106] L. Chen, W. Li, L.-Z. Fan, C.-W. Nan, Q. Zhang, *Adv. Funct. Mater.* **2019**, *29*, 1901047.

[107] H.-L. Guo, H. Sun, Z.-L. Jiang, J.-Y. Hu, C.-S. Luo, M.-Y. Gao, J.-Y. Cheng, W.-K. Shi, H.-J. Zhou, S.-G. Sun, *ACS Appl. Mater. Interfaces* **2019**, *11*, 46783.

[108] S. A. Pervez, P. Ganjeh-Anzabi, U. Farooq, M. Trifkovic, E. P. L. Roberts, V. Thangadurai, *Adv. Mater. Interfaces* **2019**, *6*, 1900186.

[109] Z. Zhao, Y. Zhang, S. Li, S. Wang, Y. Li, H. Mi, L. Sun, X. Ren, P. Zhang, *J. Mater. Chem. A* **2019**, *7*, 25818.

[110] L. Cong, Y. Li, W. Lu, J. Jie, Y. Liu, L. Sun, H. Xie, *J. Power Sources* **2020**, *446*, 227365.

[111] C. Yan, P. Zhu, H. Jia, Z. Du, J. Zhu, R. Orenstein, H. Cheng, N. Wu, M. Dirican, X. Zhang, *Energy Storage Mater.* **2020**, *26*, 448.

[112] M. Du, K. Liao, Q. Lu, Z. Shao, *Energy Environ. Sci.* **2019**, *12*, 1780.

[113] Z. Ahmad, T. Xie, C. Maheshwari, J. C. Grossman, V. Viswanathan, *ACS Cent. Sci.* **2018**, *4*, 996.

[114] X. Han, Y. Gong, K. Fu, X. He, G. T. Hitz, J. Dai, A. Pearse, B. Liu, H. Wang, G. Rubloff, Y. Mo, V. Thangadurai, E. D. Wachsman, L. Hu, *Nat. Mater.* **2017**, *16*, 572.

[115] K. K. Fu, Y. H. Gong, Z. Z. Fu, H. Xie, Y. G. Yao, B. Y. Liu, M. Carter, E. Wachsman, L. B. Hu, *Angew. Chem., Int. Ed.* **2017**, *56*, 14942.

[116] K. K. Fu, Y. H. Gong, B. Y. Liu, Y. Z. Zhu, S. M. Xu, Y. G. Yao, W. Luo, C. Wang, S. D. Lacey, J. Q. Dai, Y. N. Chen, Y. F. Mo, E. Wachsman, L. B. Hu, *Sci. Adv.* **2017**, *3*, e1601659.

[117] H. Zhong, L. Sang, F. Ding, J. X. Song, Y. H. Mai, *Electrochim. Acta* **2018**, *277*, 268.

[118] W. Luo, Y. Gong, Y. Zhu, K. K. Fu, J. Dai, S. D. Lacey, C. Wang, B. Liu, X. Han, Y. Mo, E. D. Wachsman, L. Hu, *J. Am. Chem. Soc.* **2016**, *138*, 12258.

[119] F. Hu, Y. Li, Y. Wei, J. Yang, P. Hu, Z. Rao, X. Chen, L. Yuan, Z. Li, *ACS Appl. Mater. Interfaces* **2020**, *12*, 12793.

[120] C. Wang, Y. Gong, B. Liu, K. Fu, Y. Yao, E. Hitz, Y. Li, J. Dai, S. Xu, W. Luo, E. D. Wachsman, L. Hu, *Nano Lett.* **2017**, *17*, 565.

[121] H. S. Jadhav, R. S. Kalubarme, A. H. Jadhav, J. G. Seo, *Electrochim. Acta* **2016**, *199*, 126.

[122] Y. Liu, D. Lin, Y. Jin, K. Liu, X. Tao, Q. Zhang, X. Zhang, Y. Cui, *Sci. Adv.* **2017**, *3*, eaao0713.

[123] C. Yang, L. Zhang, B. Liu, S. Xu, T. Hamann, D. McOwen, J. Dai, W. Luo, Y. Gong, E. D. Wachsman, L. Hu, *Proc. Natl. Acad. Sci. USA* **2018**, *115*, 3770.

[124] K. Kataoka, H. Nagata, J. Akimoto, *Sci. Rep.* **2018**, *8*, 9965.

[125] T. Swamy, R. Park, B. W. Sheldon, D. Rettenwander, L. Porz, S. Berendts, R. Uecker, W. C. Carter, Y.-M. Chiang, *J. Electrochem. Soc.* **2018**, *165*, A3648.

[126] J. Li, C. Ma, M. Chi, C. Liang, N. J. Dudney, *Adv. Energy Mater.* **2015**, *5*, 1401408.

[127] S. P. Jand, P. Kaghazchi, *MRS Commun.* **2018**, *8*, 591.

[128] B. Gao, R. Jalem, Y. Ma, Y. Tateyama, *Chem. Mater.* **2020**, *32*, 85.

[129] S. Yu, A. Mertens, H. Tempel, R. Schierholz, H. Kungl, R.-A. Eichel, *ACS Appl. Mater. Interfaces* **2018**, *10*, 22264.

[130] F. Li, J. Li, F. Zhu, T. Liu, B. Xu, T.-H. Kim, M. J. Kramer, C. Ma, L. Zhou, C.-W. Nan, *Matter* **2019**, *1*, 1001.

[131] A. N. Filippin, T.-Y. Lin, M. Rawlence, T. Zünd, K. Kravchyk, J. Sastre-Pellicer, S. G. Haass, A. Wäckerlin, M. V. Kovalenko, S. Buecheler, *RSC Adv.* **2018**, *8*, 20304.

[132] X. Judez, G. G. Eshetu, C. Li, L. M. Rodriguez-Martinez, H. Zhang, M. Armand, *Joule* **2018**, *2*, 2208.

[133] L. Miara, A. Windmüller, C.-L. Tsai, W. D. Richards, Q. Ma, S. Uhlenbruck, O. Guillon, G. Ceder, *ACS Appl. Mater. Interfaces* **2016**, *8*, 26842.

[134] P. Xu, W. Rheinheimer, S. N. Shuvo, Z. Qi, O. Levit, H. Wang, Y. Ein-Eli, L. A. Stanciu, *ChemElectroChem* **2019**, *6*, 4576.

[135] A. Brazier, L. Dupont, L. Dantras-Laffont, N. Kuwata, J. Kawamura, J.-M. Tarascon, *Chem. Mater.* **2008**, *20*, 2352.

[136] H. W. Kwak, Y. J. Park, *Sci. Rep.* **2019**, *9*, 8099.

[137] Y. Xiao, L. J. Miara, Y. Wang, G. Ceder, *Joule* **2019**, *3*, 1252.

[138] N. J. J. de Klerk, M. Wagemaker, *ACS Appl. Mater. Interfaces* **2018**, *1*, 5609.

[139] J. Maier, *Ber. Bunsenges. Phys. Chern.* **1984**, *88*, 1057.

[140] K. Takada, N. Ohta, L. Zhang, X. Xu, B. T. Hang, T. Ohnishi, M. Osada, T. Sasaki, *Solid State Ionics* **2012**, *225*, 594.

**ADVANCED
SCIENCE NEWS**

www.advancedsciencenews.com

**ADVANCED
ENERGY
MATERIALS**

www.advenergymat.de

[141] M. Haruta, S. Shiraki, T. Suzuki, A. Kumatani, T. Ohsawa, Y. Takagi, R. Shimizu, T. Hitosugi, *Nano Lett.* **2015**, *15*, 1498.

[142] M. Fingerle, R. Buchheit, S. Sicolo, K. Albe, R. Hausbrand, *Chem. Mater.* **2017**, *29*, 7675.

[143] K. Takada, N. Ohta, L. Zhang, K. Fukuda, I. Sakaguchi, R. Ma, M. Osada, T. Sasaki, *Solid State Ionics* **2008**, *179*, 1333.

[144] C. Yada, C. E. Lee, D. Laughman, L. Hannah, H. Iba, B. E. Hayden, *J. Electrochem. Soc.* **2015**, *162*, A722.

[145] W. Luo, Y. Gong, Y. Zhu, Y. Li, Y. Yao, Y. Zhang, K. K. Fu, G. Pastel, C.-F. Lin, Y. Mo, E. D. Wachsman, L. Hu, *Adv. Mater.* **2017**, *29*, 1606042.

[146] Y. Liu, C. Li, B. Li, H. Song, Z. Cheng, M. Chen, P. He, H. Zhou, *Adv. Energy Mater.* **2018**, *8*, 1702374.

[147] T. Kato, T. Hamanaka, K. Yamamoto, T. Hirayama, F. Sagane, M. Motoyama, Y. Iriyama, *J. Power Sources* **2014**, *260*, 292.

[148] M. He, Z. Cui, C. Chen, Y. Li, X. Guo, *J. Mater. Chem. A* **2018**, *6*, 11463.

[149] G. V. Alexander, S. Patra, S. V. S. Raj, M. K. Sugumar, M. M. U. Din, R. Murugan, *J. Power Sources* **2018**, *396*, 764.

[150] G. V. Alexander, M. S. Indu, S. Kamakshy, R. Murugan, *Electrochim. Acta* **2020**, *332*, 135511.

[151] H. Visbal, Y. Aihara, S. Ito, T. Watanabe, Y. Park, S. Doo, *J. Power Sources* **2016**, *314*, 85.

[152] J. H. Woo, J. E. Trevey, A. S. Cavanagh, Y. S. Choi, S. C. Kim, S. M. George, K. H. Oh, S.-H. Lee, *J. Electrochem. Soc.* **2012**, *159*, A1120.

[153] Y. Liu, Q. Sun, Y. Zhao, B. Wang, R. Y. Li, P. Kaghazchi, K. R. Adair, R. Li, C. Zhang, J. Liu, L.-Y. Kuo, Y. Hu, T.-K. Sham, L. Zhang, R. Yang, S. Lu, X. Song, X. Sun, *ACS Appl. Mater. Interfaces* **2018**, *10*, 31240.

[154] N. Machida, J. Kashiwagi, M. Naito, T. Shigematsu, *Solid State Ionics* **2012**, *225*, 354.

[155] H. Xu, Y. Li, A. Zhou, N. Wu, S. Xin, Z. Li, J. B. Goodenough, *Nano Lett.* **2018**, *18*, 7414.

[156] S. Yubuchi, Y. Ito, T. Matsuyama, A. Hayashi, M. Tatsumisago, *Solid State Ionics* **2016**, *285*, 79.

[157] G. V. Alexander, N. C. R. Navarro, A. Miura, K. Tadanaga, R. Murugan, *J. Mater. Chem. A* **2018**, *6*, 21018.

[158] Y. Sakurai, A. Sakuda, A. Hayashi, M. Tatsumisago, *Solid State Ionics* **2011**, *182*, 59.

[159] Y. Ito, Y. Sakurai, S. Yubuchi, A. Sakuda, A. Hayashi, M. Tatsumisago, *J. Electrochem. Soc.* **2015**, *162*, A1610.

[160] F. S. Gittleson, F. E. Gabaly, *Nano Lett.* **2017**, *17*, 6974.

[161] C. Vinado, S. Wang, Y. He, X. Xiao, Y. Li, C. Wang, J. Yang, *J. Power Sources* **2018**, *396*, 824.

[162] N. Ohta, K. Takada, L. Q. Zhang, R. Z. Ma, M. Osada, T. Sasaki, *Adv. Mater.* **2006**, *18*, 2226.

[163] Y. Seino, T. Ota, K. Takada, *J. Power Sources* **2011**, *196*, 6488.

[164] A. Sakuda, A. Hayashi, T. Ohtomo, S. Hama, M. Tatsumisago, *J. Power Sources* **2011**, *196*, 6735.

[165] Y. A. Du, N. A. W. Holzwarth, *J. Electrochem. Soc.* **2007**, *154*, A999.

[166] Y. A. Du, N. A. W. Holzwarth, *ECS Trans.* **2008**, *13*, 75.

[167] J.-W. Choi, J.-W. Lee, *Solid State Ionics* **2016**, *289*, 173.

[168] J. B. Bates, D. J. Dudney, G. R. Gruzalski, R. A. Zuhr, A. Choudhury, J. D. Robertson, *Solid State Ionics* **1992**, *53–56*, 647.

[169] T. M. Bandhauer, S. Garimella, T. F. Fuller, *J. Electrochem. Soc.* **2011**, *158*, R1.

[170] C. A. Karthik, P. Kalita, X. Cui, X. Peng, *Energy Storage* **2020**, *2*, e137.

[171] A. Perea, M. Dontigny, K. Zaghib, *J. Power Sources* **2017**, *359*, 182.

[172] H. Chung, B. Kang, *Chem. Mater.* **2017**, *29*, 8611.

[173] M. Gellert, E. Dashjav, D. Grüner, Q. Ma, F. Tietz, *Ionics* **2018**, *24*, 1001.

[174] R. Chen, Q. Li, X. Yu, L. Chen, H. Li, *Chem. Rev.* **2020**, *120*, 6820.

[175] V. Kumaravel, J. Bartlett, S. C. Pillai, *Adv. Energy Mater.* **2020**, *11*, 2002869.

[176] X. Lin, G. Zhou, J. Liu, J. Yu, M. B. Effat, J. Wu, F. Ciucci, *Adv. Energy Mater.* **2020**, *10*, 2001235.

[177] H. Nara, D. Mukoyama, R. Shimizu, T. Momma, T. Osada, *J. Power Sources* **2019**, *409*, 139.

[178] H.-C. Wu, H.-C. Wu, E. Lee, N.-L. Wu, *Electrochem. Commun.* **2010**, *12*, 488.

[179] H.-C. Wu, E. Lee, N.-L. Wu, T. R. Jow, *J. Power Sources* **2012**, *197*, 301.

[180] H. R. Kim, W. M. Choi, *Scr. Mater.* **2018**, *146*, 100.

[181] X. Ji, K. T. Lee, L. F. Nazar, *Nat. Mater.* **2009**, *8*, 500.

[182] L. Zhang, Y. Liu, Z. Zhao, P. Jiang, T. Zhang, M. Li, S. Pan, T. Tang, T. Wu, P. Li, Y. Hou, H. Lu, *ACS Nano* **2020**, *14*, 8495.

[183] Q. Zhang, N. Huang, Z. Huang, L. Cai, J. Wu, X. Yao, *J. Energy Chem.* **2020**, *40*, 151.

[184] X. Tao, Y. Liu, W. Liu, G. Zhou, J. Zhao, D. Lin, O. Sheng, W. Zhang, H.-W. Lee, Y. Cui, *Nano Lett.* **2017**, *17*, 2967.

[185] C. Yu, S. Ganapathy, E. R. H. van Eck, H. Wang, S. Basak, Z. Li, M. Wagemaker, *Nat. Commun.* **2017**, *8*, 1086.

[186] F. Han, J. Yu, X. Fan, T. Gao, C. Luo, Z. Ma, L. Suo, C. Wang, *Nano Lett.* **2016**, *16*, 4521.

[187] T. Matsuyama, A. Sakuda, A. Hayashi, Y. Togawa, S. Mori, M. Tatsumisago, *J. Solid State Electrochem.* **2013**, *17*, 2697.

[188] B.-C. Kim, K. Takada, N. Ohta, Y. Seino, L. Zhang, H. Wada, T. Sasaki, *Solid State Ionics* **2005**, *176*, 2383.

[189] X. Yao, D. Liu, C. Wang, P. Long, G. Peng, Y.-S. Hu, H. Li, L. Chen, X. Xu, *Nano Lett.* **2016**, *16*, 7148.

[190] P. Long, Q. Xu, G. Peng, X. Yao, X. Xu, *ChemElectroChem* **2016**, *3*, 764.

[191] S. M. Hosseini, A. Varzi, S. Ito, Y. Aihara, S. Passerini, *Energy Storage Mater.* **2020**, *27*, 61.

[192] M. Chen, X. Yin, M. V. Reddy, S. Adams, *J. Mater. Chem. A* **2015**, *3*, 10698.

[193] H. Wang, X. Cao, W. Liu, X. Sun, *Front. Energy Res.* **2019**, *7*, 112.

[194] A. Hayashi, T. Ohtomo, F. Mizuno, K. Tadanaga, M. Tatsumisago, *Electrochem. Commun.* **2003**, *5*, 701.

[195] H. Qiu, T. Tang, M. Asif, W. Li, T. Zhang, Y. Hou, *Nano Energy* **2019**, *65*, 103989.

[196] H. Zhong, L. Sang, F. Ding, J. Song, Y. Mai, *Electrochim. Acta* **2018**, *277*, 268.

[197] L.-L. Kong, L. Wang, Z.-C. Ni, S. Liu, G.-R. Li, X.-P. Gao, *Adv. Funct. Mater.* **2019**, *29*, 1808756.

[198] X. Xu, J. Cheng, Y. Li, X. Nie, L. Ci, *J. Solid State Electrochem.* **2019**, *23*, 3145.

[199] X. Judez, H. Zhang, C. Li, J. A. González-Marcos, Z. Zhou, M. Armand, L. M. Rodriguez-Martinez, *J. Phys. Chem. Lett.* **2017**, *8*, 1956.

[200] G. G. Eshetu, X. Judez, C. Li, M. Martinez-Ibañez, I. Gracia, O. Bondarchuk, J. Carrasco, L. M. Rodriguez-Martinez, H. Zhang, M. Armand, *J. Am. Chem. Soc.* **2018**, *140*, 9921.

[201] B. Ding, J. Wang, Z. Fan, S. Chen, Q. Lin, X. Lu, H. Du, A. K. Najundan, G. Yushin, X. Zhang, Y. Yamauchi, *Mater. Today* **2020**, *40*, 114.

[202] H. Zhang, U. Oteo, X. Judez, G. G. Eshetu, M. Martinez-Ibañez, J. Carrasco, C. Li, M. Armand, *Joule* **2019**, *3*, 1689.

[203] H. Zhang, X. Judez, A. Santiago, M. Martinez-Ibañez, M. Á. Muñoz-Márquez, J. Carrasco, C. Li, G. G. Eshetu, M. Armand, *Adv. Energy Mater.* **2019**, *9*, 1900763.

[204] V. Shutthanandan, M. Nandasiri, J. Zheng, M. H. Engelhard, W. Xu, S. Thevuthasan, V. Murugesan, *J. Electron Spectrosc. Relat. Phenom.* **2019**, *231*, 2.

[205] A. Schwöbel, R. Hausbrand, W. Jaegermann, *Solid State Ionics* **2015**, *273*, 51.

[206] K. N. Wood, K. X. Steirer, S. E. Hafner, C. Ban, S. Santhanagopalan, S. H. Lee, G. Teeter, *Nat. Commun.* **2018**, *9*, 2490.

[207] M. Hekmatfar, A. Kazzazi, G. G. Eshetu, I. Hasa, S. Passerini, *ACS Appl. Mater. Interfaces* **2019**, *11*, 43166.

ADVANCED
SCIENCE NEWS

www.advancedsciencenews.com

ADVANCED
ENERGY
MATERIALS

www.advenergymat.de

[208] F. Zhao, Q. Sun, C. Yu, S. Zhang, K. Adair, S. Wang, Y. Liu, Y. Zhao, J. Liang, C. Wang, X. Li, X. Li, W. Xia, R. Li, H. Huang, L. Zhang, S. Zhao, S. Lu, X. Sun, *ACS Energy Lett.* **2020**, *5*, 1035.

[209] M. Zarabian, M. Bartolini, P. Pereira-Almao, V. Thangadurai, *J. Electrochem. Soc.* **2017**, *164*, A1133.

[210] H. W. Werner, *Surf. Interface Anal.* **1980**, *2*, 56.

[211] Y. Liu, M. Lorenz, A. V. Ievlev, O. S. Ovchinnikova, *Adv. Funct. Mater.* **2020**, *30*, 2002201.

[212] J. Bailey, R. Havelund, A. G. Shard, I. S. Gilmore, M. R. Alexander, J. S. Sharp, D. J. Scurr, *ACS Appl. Mater. Interfaces* **2015**, *7*, 2654.

[213] W. Li, A. Dolocan, P. Oh, H. Celio, S. Park, J. Cho, A. Manthiram, *Nat. Commun.* **2017**, *8*, 14589.

[214] M. Saccoccio, J. Yu, Z. Lu, S. C. T. Kwok, J. Wang, K. K. Yeung, M. M. F. Yuen, F. Ciucci, *J. Power Sources* **2017**, *365*, 43.

[215] H.-H. Sun, A. Manthiram, *Chem. Mater.* **2017**, *29*, 8486.

[216] F. Walther, R. Koerver, T. Fuchs, S. Ohno, J. Sann, M. Rohnke, W. G. Zeier, J. Janek, *Chem. Mater.* **2019**, *31*, 3745.

[217] S. Uhlenbruck, C. Dellen, S. Möller, S. Lobe, C.-L. Tsai, M. Finsterbusch, M. Bram, O. Guillon, *Solid State Ionics* **2018**, *320*, 259.

[218] K. Park, B.-C. Yu, J.-W. Jung, Y. Li, W. Zhou, H. Gao, S. Son, J. B. Goodenough, *Chem. Mater.* **2016**, *28*, 8051.

[219] K. G. Carr-Brion, K. W. Payne, *Analyst* **1970**, *95*, 977.

[220] K. Kalaga, I. A. Shkrob, R. T. Haasch, C. Peebles, J. Bareño, D. P. Abraham, *J. Phys. Chem. C* **2017**, *121*, 23333.

[221] E. Radvanyi, E. D. Vito, W. Porcher, S. J. S. Larbi, *J. Anal. At. Spectrom.* **2014**, *29*, 1120.

[222] E. E. Horopanitis, G. Perentzis, I. Samaras, T. Dikonimos-Makris, N. Lisi, L. Papadimitriou, *J. Solid State Electrochem.* **2003**, *8*, 55.

[223] E. Jeong, C. Hong, Y. Tak, S. C. Nam, S. Cho, *J. Power Sources* **2006**, *159*, 223.

[224] S. H. Kim, K. Kim, H. Choi, D. Im, S. Heo, H. S. Choi, *J. Mater. Chem. A* **2019**, *7*, 13650.

[225] A. Uhart, J. B. Ledeuil, B. Pecquenard, F. Le Cras, M. Proust, H. Martinez, *ACS Appl. Mater. Interfaces* **2017**, *9*, 33238.

[226] L. Lobo, B. Fernández, R. Pereiro, *J. Anal. At. Spectrom.* **2017**, *32*, 920.

[227] The Surface Science Society of Japan, *Compendium of Surface and Interface Analysis*, Springer, Singapore **2018**.

[228] H. G. Song, K.-S. Park, Y. J. Park, *Solid State Ionics* **2012**, *225*, 532.

[229] V. Müller, R.-G. Scurtu, K. Richter, T. Waldmann, M. Memm, M. A. Danzer, M. Wohlfahrt-Mehrens, *J. Electrochem. Soc.* **2019**, *166*, A3796.

[230] N. Ghanbari, T. Waldmann, M. Kasper, P. Axmann, M. Wohlfahrt-Mehrens, *ECS Electrochem. Lett.* **2015**, *4*, A100.

[231] N. Ghanbari, T. Waldmann, M. Kasper, P. Axmann, M. Wohlfahrt-Mehrens, *J. Phys. Chem. C* **2016**, *120*, 22225.

[232] K. Richter, T. Waldmann, M. Kasper, C. Pfeifer, M. Memm, P. Axmann, M. Wohlfahrt-Mehrens, *J. Phys. Chem. C* **2019**, *123*, 18795.

[233] A. Gundlach-Graham, D. Gunther, *Anal. Bioanal. Chem.* **2016**, *408*, 2687.

[234] T. Schwieters, M. Evertz, M. Mense, M. Winter, S. Nowak, *J. Power Sources* **2017**, *356*, 47.

[235] T. Schwieters, M. Evertz, A. Fengler, M. Börner, T. Dagger, Y. Stenzel, P. Harte, M. Winter, S. Nowak, *J. Power Sources* **2018**, *380*, 194.

[236] S. Smetaczek, M. Bonta, A. Wachter-Welzl, S. Taibl, R. Wagner, D. Rettenwander, J. Fleig, A. Limbeck, *J. Anal. At. Spectrom.* **2020**, *35*, 972.

[237] H. A. Ardakani, S. H. Tavassoli, *J. Appl. Spectrosc.* **2013**, *80*, 153.

[238] F. J. Fortes, J. Moros, P. Lucena, L. M. Cabalín, J. J. Laserna, *Anal. Chem.* **2013**, *85*, 640.

[239] A. De Giacomo, M. Dell'Aaglio, R. Gaudiuso, G. Cristoforetti, S. Legnaioli, V. Palleschi, E. Tognoni, *Spectroschim. Acta B* **2008**, *63*, 980.

[240] A. D'Ulivo, M. Onor, E. Pitzalis, R. Spiniello, L. Lampugnani, G. Cristoforetti, S. Legnaioli, V. Palleschi, E. Tognoni, *Spectroschim. Acta B* **2006**, *61*, 797.

[241] C. Fabre, M.-C. Boiron, J. Dubessy, A. Chabiron, B. Charoy, T. M. Crespo, *Geochim. Cosmochim. Acta* **2002**, *66*, 1401.

[242] Y. Dwivedi, S. N. Thakur, S. B. Rai, *Appl. Opt.* **2010**, *49*, C42.

[243] D. Rettenwander, R. Wagner, A. Reyer, M. Bonta, L. Cheng, M. M. Doeff, A. Limbeck, M. Wilkening, G. Amthauer, *J. Phys. Chem. C* **2018**, *122*, 3780.

[244] H. Hou, L. Cheng, T. Richardson, G. Chen, M. Doeff, R. Zheng, R. Russo, V. Zorba, *J. Anal. At. Spectrom.* **2015**, *30*, 2295.

[245] L. Cheng, E. J. Crumlin, W. Chen, R. Qiao, H. Hou, S. F. Lux, V. Zorba, R. Russo, R. Kostecki, Z. Liu, K. Persson, W. Yang, J. Cabana, T. Richardson, G. Chen, M. Doeff, *Phys. Chem. Chem. Phys.* **2014**, *16*, 18294.

[246] L. Cheng, W. Chen, M. Kunz, K. Persson, N. Tamura, G. Chen, M. Doeff, *ACS Appl. Mater. Interfaces* **2015**, *7*, 2073.

[247] K. M. Yu, Ion Beam Analysis in Materials Science, https://sites.google.com/a/lbl.gov/rbs-lab/ion-beam-analysis (accessed: November 2008).

[248] K. Mima, R. Gonzalez-Arrabal, H. Azuma, A. Yamazaki, C. Okuda, Y. Ukyo, H. Sawada, K. Fujita, Y. Kato, J. M. Perlado, S. Nakai, *Nucl. Instrum. Methods Phys. Res., Sect B* **2012**, *290*, 79.

[249] B. Tsuchiya, J. Ohnishi, Y. Sasaki, T. Yamamoto, Y. Yamamoto, M. Motoyama, Y. Iriyama, K. Morita, *Adv. Mater. Interfaces* **2019**, *6*, 1900100.

[250] K. Morita, B. Tsuchiya, J. Ohnishi, T. Yamamoto, Y. Iriyama, H. Tsuchida, T. Majima, K. Suzuki, *Nucl. Instrum. Methods Phys. Res., Sect B* **2018**, *426*, 30.

[251] V. Mathayan, M. V. Moro, K. Morita, B. Tsuchiya, R. Ye, M. Baba, D. Primetzhofer, *Appl. Phys. Lett.* **2020**, *117*, 023902.

[252] S. Chhillar, R. Acharya, S. Sodaye, P. K. Pujari, *Anal. Chem.* **2014**, *86*, 11167.

[253] K. Yoshino, K. Suzuki, Y. Yamada, T. Satohy, M. Finsterbuschz, K. Fujitax, T. Kamiya, A. Yamazakik, K. Mimax, M. Hirayama, R. Kanno, *Int. J. PIXE* **2017**, *27*, 11.

[254] R. Senga, K. Suenaga, *Nat. Commun.* **2015**, *6*, 7943.

[255] M. Bosman, M. Watanabe, D. T. L. Alexander, V. J. Keast, *Ultramicroscopy* **2006**, *106*, 1024.

[256] R. F. Egerton, M. Malac, *J. Electron Spectrosc. Relat. Phenom.* **2005**, *143*, 43.

[257] X. Li, Z. Ren, M. Norouzi Banis, S. Deng, Y. Zhao, Q. Sun, C. Wang, X. Yang, W. Li, J. Liang, X. Li, Y. Sun, K. Adair, R. Li, Y. Hu, T.-K. Sham, H. Huang, L. Zhang, S. Lu, J. Luo, X. Sun, *ACS Energy Lett.* **2019**, *4*, 2480.

[258] S.-Y. Lee, K.-Y. Park, W.-S. Kim, S. Yoon, S.-H. Hong, K. Kang, M. Kim, *Nano Energy* **2016**, *19*, 234.

[259] K. Yamamoto, Y. Iriyama, T. Hirayama, *Microscopy* **2017**, *66*, i25.

[260] N. Taguchi, H. Sakaebe, S. Tanaka, *Surf. Interface Anal.* **2018**, *52*, 335.

[261] Y. Nomura, K. Yamamoto, M. Fujii, T. Hirayama, E. Igaki, K. Saitoh, *Nat. Commun.* **2020**, *11*, 2824.

[262] Y. Nomura, K. Yamamoto, T. Hirayama, M. Ohkawa, E. Igaki, N. Hojo, K. Saitoh, *Nano Lett.* **2018**, *18*, 5892.

[263] Y. Nomura, K. Yamamoto, T. Hirayama, E. Igaki, K. Saitoh, *ACS Energy Lett.* **2020**, *5*, 2098.

[264] T. Kato, R. Yoshida, K. Yamamoto, T. Hirayama, M. Motoyama, W. C. West, Y. Iriyama, *J. Power Sources* **2016**, *325*, 584.

[265] C. Ma, Y. Cheng, K. Yin, J. Luo, A. Sharafi, J. Sakamoto, J. Li, K. L. More, N. J. Dudney, M. Chi, *Nano Lett.* **2016**, *16*, 7030.

[266] S. Frabboni, G. Matteucci, G. Pozzi, *Phys. Rev. Lett.* **1985**, *11*, 2196.

[267] C. Ozsoy-Keskinbora, C. B. Boothroyd, R. E. Dunin-Borkowski, P. A. van Aken, C. T. Koch, *Ultramicroscopy* **2016**, *165*, 8.

[268] D. Shindo, Y. Murakami, *J. Phys. D: Appl. Phys.* **2008**, *41*, 183002.

[269] D. Wolf, L. A. Rodriguez, A. Béché, E. Javon, L. Serrano, C. Magen, C. Gatel, A. Lubk, H. Lichte, S. Bals, G. van Tendeloo, A. Fernández-Pacheco, J. M. De Teresa, E. Snoeck, *Chem. Mater.* **2015**, *27*, 6771.

[270] D. Gabor, *Nature* **1948**, *161*, 777.

[271] J. M. Cowley, *Ultramicroscopy* **1992**, *41*, 8.

[272] K. Yamamoto, Y. Iriyama, T. Asaka, T. Hirayama, *J. Electron Microsc.* **2000**, *49*, 31.

[273] S. Anada, K. Yamamoto, H. Sasaki, N. Shibata, M. Matsumoto, Y. Hori, K. Kinugawa, A. Imamura, T. Hirayama, *Microscopy* **2019**, *68*, 159.

[274] Y. Nomura, K. Yamamoto, T. Hirayama, S. Ouchi, E. Igaki, K. Saitoh, *Angew. Chem., Int. Ed.* **2019**, *131*, 5292.

[275] T. Hirayama, Y. Aizawa, K. Yamamoto, T. Sato, H. Murata, R. Yoshida, C. A. J. Fisher, T. Kato, *Ultramicroscopy* **2017**, *173*, 64.

[276] Y. Aizawa, K. Yamamoto, T. Sato, H. Murata, R. Yoshida, C. A. J. Fisher, T. Kato, Y. Iriyama, T. Hirayama, *Ultramicroscopy* **2017**, *178*, 20.

[277] K. Yamamoto, Y. Iriyama, T. Asaka, T. Hirayama, H. Fujita, C. A. J. Fisher, K. Nonaka, Y. Sugita, Z. Ogumi, *Angew. Chem., Int. Ed.* **2010**, *49*, 4414.

[278] X. Wang, Y. Li, Y. S. Meng, *Joule* **2018**, *2*, 2225.

[279] D. Cheng, T. A. Wynn, X. Wang, S. Wang, M. Zhang, R. Shimizu, S. Bai, H. Nguyen, C. Fang, M. Kim, W. Li, B. Lu, S. J. Kim, Y. S. Meng, *Joule* **2020**, *4*, 2484.

[280] Y. Li, Y. Li, A. Pei, K. Yan, Y. Sun, C.-L. Wu, L.-M. Joubert, R. Chin, A. L. Koh, Y. Yu, J. Perrino, B. Butz, S. Chu, Y. Cui, *Science* **2017**, *358*, 506.

[281] Y. B. Song, D. H. Kim, H. Kwak, D. Han, S. Kang, J. H. Lee, S.-M. Bak, K.-W. Nam, H.-W. Lee, Y. S. Jung, *Nano Lett.* **2020**, *20*, 4337.

[282] O. Sheng, J. Zheng, Z. Ju, C. Jin, Y. Wang, M. Chen, J. Nai, T. Liu, W. Zhang, Y. Liu, X. Tao, *Adv. Mater.* **2020**, *32*, 2000223.

[283] T. Liu, J. Zheng, H. Hu, O. Sheng, Z. Ju, G. Lu, Y. Liu, J. Nai, Y. Wang, W. Zhang, X. Tao, *J. Energy Chem.* **2021**, *55*, 272.

[284] O. Sheng, C. Jin, M. Chen, Z. Ju, Y. Liu, Y. Wang, J. Nai, T. Liu, W. Zhang, X. Tao, *J. Mater. Chem. A* **2020**, *8*, 13541.

[285] L. Cheng, C. H. Wu, A. Jarry, W. Chen, Y. Ye, J. Zhu, R. Kostecki, K. Persson, J. Guo, M. Salmeron, G. Chen, M. Doeff, *ACS Appl. Mater. Interfaces* **2015**, *7*, 17649.

[286] L. Cheng, M. Liu, A. Mehta, H. Xin, F. Lin, K. Persson, G. Chen, E. J. Crumlin, M. Doeff, *ACS Appl. Energy Mater.* **2018**, *1*, 7244.

[287] M. M. Besli, C. Usubelli, M. Metzger, V. Pande, K. Harry, D. Nordlund, S. Sainio, J. Christensen, M. M. Doeff, S. Kuppan, *ACS Appl. Mater. Interfaces* **2020**, *12*, 20605.

[288] J. Fu, P. Yu, N. Zhang, G. Ren, S. Zheng, W. Huang, X. Long, H. Li, X. Liu, *Energy Environ. Sci.* **2019**, *12*, 1404.

[289] N. Zhang, X. Long, Z. Wang, P. Yu, F. Han, J. Fu, G. Ren, Y. Wu, S. Zheng, W. Huang, C. Wang, H. Li, X. Liu, *ACS Appl. Energy Mater.* **2018**, *1*, 5968.

[290] J. Liang, S. Hwang, S. Li, J. Luo, Y. Sun, Y. Zhao, Q. Sun, W. Li, M. Li, M. N. Banis, X. Li, R. Li, L. Zhang, S. Zhao, S. Lu, H. Huang, D. Su, X. Sun, *Nano Energy* **2020**, *78*, 105107.

[291] T. Okumura, T. Nakatsutsumi, T. Ina, Y. Orikasa, H. Arai, T. Fukutsuka, Y. Iriyama, T. Uruga, H. Tanida, Y. Uchimoto, Z. Ogumi, *J. Mater. Chem.* **2011**, *21*, 10051.

[292] K. Chen, K. Yamamoto, Y. Orikasa, T. Uchiyama, Y. Ito, S. Yubuchi, A. Hayashi, M. Tatsumisago, K. Nitta, T. Uruga, Y. Uchimoto, *Solid State Ionics* **2018**, *327*, 150.

[293] L. Ye, W. Fitzhugh, E. Gil-González, Y. Wang, Y. Su, H. Su, T. Qiao, L. Ma, H. Zhou, E. Hu, X. Li, *Adv. Energy Mater.* **2020**, *10*, 2001569.

[294] S. Aktaş, O. M. Özkendir, Y. R. Eker, Ş. Ateş, Ü. Atav, G. Çelik, W. Klysubun, *J. Alloys Compd.* **2019**, *792*, 279.

[295] Ç. Kaya, F. Bondino, E. Magnano, H. Gündoğmuş, I. Ulfat, W. Klysubun, O. M. Ozkendir, *J. Electron Spectrosc. Relat. Phenom.* **2018**, *226*, 45.

[296] C. Im, D. Park, H. Kim, J. Lee, *J. Energy Chem.* **2018**, *27*, 1501.

[297] X. Li, J. Liang, J. Luo, M. Norouzi Banis, C. Wang, W. Li, S. Deng, C. Yu, F. Zhao, Y. Hu, T. K. Sham, L. Zhang, S. Zhao, S. Lu, H. Huang, R. Li, K. R. Adair, X. Sun, *Energy Environ. Sci.* **2019**, *12*, 2665.

[298] S. Deng, X. Li, Z. Ren, W. Li, J. Luo, J. Liang, J. Liang, M. N. Banis, M. Li, Y. Zhao, X. Li, C. Wang, Y. Sun, Q. Sun, R. Li, Y. Hu, H. Huang, L. Zhang, S. Lu, J. Luo, X. Sun, *Energy Storage Mater.* **2020**, *27*, 117.

[299] C. Dietrich, R. Koerver, M. W. Gaultois, G. Kieslich, G. Cibin, J. Janek, W. G. Zeier, *Phys. Chem. Chem. Phys.* **2018**, *20*, 20088.

[300] J. Guo, *J. Electron Spectrosc. Relat. Phenom.* **2013**, *188*, 71.

[301] K. Nakanishi, D. Kato, H. Arai, H. Tanida, T. Mori, Y. Orikasa, Y. Uchimoto, Z. Ohta, Z. Ogumi, *Rev. Sci. Instrum.* **2014**, *85*, 084103.

[302] X. Liu, D. Wang, G. Liu, V. Srinivasan, Z. Liu, Z. Hussain, W. Yang, *Nat. Commun.* **2013**, *4*, 1.

[303] J. J. Velasco-Velez, C. H. Wu, T. A. Pascal, L. F. Wan, J. Guo, D. Prendergast, M. Salmeron, *Science* **2014**, *346*, 831.

[304] C. Wang, X. Li, Y. Zhao, M. N. Banis, J. Liang, X. Li, Y. Sun, K. R. Adair, Q. Sun, Y. Liu, F. Zhao, S. Deng, X. Lin, R. Li, Y. Hu, T. Sham, H. Huang, L. Zhang, R. Yang, S. Lu, X. Sun, *Small Methods* **2019**, *3*, 1900261.

[305] A. Schwöbel, R. Precht, M. Motzko, M. A. Carrillo Solano, W. Calvet, R. Hausbrand, W. Jaegermann, *Appl. Surf. Sci.* **2014**, *321*, 55.

[306] J. Liang, Q. Sun, Y. Zhao, Y. Sun, C. Wang, W. Li, M. Li, D. Wang, X. Li, Y. Liu, K. Adair, R. Li, L. Zhang, R. Yang, S. Lu, H. Huang, X. Sun, *J. Mater. Chem. A* **2018**, *6*, 23712.

[307] J. Liang, X. Li, Y. Zhao, L. V. Goncharova, W. Li, K. R. Adair, M. N. Banis, Y. Hu, T. Sham, H. Huang, L. Zhang, S. Zhao, S. Lu, R. Li, X. Sun, *Adv. Energy Mater.* **2019**, *9*, 1902125.

[308] H. Kiuchi, K. Hikima, K. Shimizu, R. Kanno, F. Toshiharu, E. Matsubara, *Electrochem. Commun.* **2020**, *118*, 106790.

[309] S. Kim, M. Hirayama, S. Taminato, R. Kanno, *Dalton Trans.* **2013**, *42*, 13112.

[310] S. Kim, M. Hirayama, K. Suzuki, R. Kanno, *Solid State Ionics* **2014**, *262*, 578.

[311] J. Sastre, X. Chen, A. Aribia, A. N. Tiwari, Y. E. Romanyuk, *ACS Appl. Mater. Interfaces* **2020**, *12*, 36196.

[312] G. Vardar, W. J. Bowman, Q. Lu, J. Wang, R. J. Chater, A. Aguadero, R. Seibert, J. Terry, A. Hunt, I. Waluyo, D. D. Fong, A. Jarry, E. J. Crumlin, S. L. Hellstrom, Y. M. Chiang, B. Yildiz, *Chem. Mater.* **2018**, *30*, 6259.

[313] C. Wang, G. Bai, Y. Yang, X. Liu, H. Shao, *Nano Res.* **2019**, *12*, 217.

[314] T. V. Vu, C. Park, *Solid State Ionics* **2017**, *313*, 14.

[315] J. Z. Lee, Z. Wang, H. L. Xin, T. A. Wynn, Y. S. Meng, *J. Electrochem. Soc.* **2017**, *164*, A6268.

[316] Y. Wang, Z. Liu, X. Zhu, Y. Tang, F. Huang, *J. Power Sources* **2013**, *224*, 225.

[317] P. Hofmann, F. Walther, M. Rohnke, J. Sann, W. G. Zeier, J. Janek, *Solid State Ionics* **2019**, *342*, 115054.

[318] M. Xie, X. Lin, Z. Huang, Y. Li, Y. Zhong, Z. Cheng, L. Yuan, Y. Shen, X. Lu, T. Zhai, Y. Huang, *Adv. Funct. Mater.* **2020**, *30*, 1905949.

[319] J. S. Park, L. Cheng, V. Zorba, A. Mehta, J. Cabana, G. Chen, M. M. Doeff, T. J. Richardson, J. H. Park, J. W. Son, W. S. Hong, *Thin Solid Films* **2015**, *576*, 55.

[320] F. Shen, M. B. Dixit, X. Xiao, K. B. Hatzell, *ACS Energy Lett.* **2018**, *3*, 1056.

[321] W. Zhang, D. Schröder, T. Arlt, I. Manke, R. Koerver, R. Pinedo, D. A. Weber, J. Sann, W. G. Zeier, J. Janek, *J. Mater. Chem. A* **2017**, *5*, 9929.

[322] K. J. Harry, D. T. Hallinan, D. Y. Parkinson, A. A. MacDowell, N. P. Balsara, *Nat. Mater.* **2014**, *13*, 69.

[323] D. Devaux, K. J. Harry, D. Y. Parkinson, R. Yuan, D. T. Hallinan, A. A. MacDowell, N. P. Balsara, *J. Electrochem. Soc.* **2015**, *162*, A1301.

[324] F. Sun, K. Dong, M. Osenberg, A. Hilger, S. Risse, Y. Lu, P. H. Kamm, M. Klaus, H. Markötter, F. García-Moreno, T. Arlt, I. Manke, *J. Mater. Chem. A* **2018**, *6*, 22489.

[325] N. Seitzman, H. Guthrey, D. B. Sulas, H. A. S. Platt, M. Al-Jassim, S. Pylypenko, *J. Electrochem. Soc.* **2018**, *165*, A3732.

[326] X. Wu, J. Billaud, I. Jerjen, F. Marone, Y. Ishihara, M. Adachi, Y. Adachi, C. Villevieille, Y. Kato, *Adv. Energy Mater.* **2019**, *9*, 1901547.

[327] J. Tippens, J. C. Miers, A. Afshar, J. A. Lewis, F. J. Q. Cortes, H. Qiao, T. S. Marchese, C. V. Di Leo, C. Saldana, M. T. McDowell, *ACS Energy Lett.* **2019**, *4*, 1475.

[328] T. Li, H. Kang, X. Zhou, C. Lim, B. Yan, V. De Andrade, F. De Carlo, L. Zhu, *ACS Appl. Mater. Interfaces* **2018**, *10*, 16927.

[329] N. Sun, Q. Liu, Y. Cao, S. Lou, M. Ge, X. Xiao, W. Lee, Y. Gao, G. Yin, J. Wang, X. Sun, *Angew. Chem., Int. Ed.* **2019**, *58*, 18647.

[330] M. M. Besli, S. Xia, S. Kuppan, Y. Huang, M. Metzger, A. K. Shukla, G. Schneider, S. Hellstrom, J. Christensen, M. M. Doeff, Y. Liu, *Chem. Mater.* **2019**, *31*, 491.

[331] Y. Kimura, M. Fakkao, T. Nakamura, T. Okumura, N. Ishiguro, O. Sekizawa, K. Nitta, T. Uruga, M. Tada, Y. Uchimoto, K. Amezawa, *ACS Appl. Energy Mater.* **2020**, *3*, 7782.

[332] B. C. Larson, W. Yang, G. E. Ice, J. D. Budai, J. Z. Tischler, *Nature* **2002**, *415*, 887.

[333] J. F. Ankner, W. T. Heller, K. W. Herwig, F. Meilleur, D. A. A. Myles, *Curr. Protoc. Protein Sci.* **2013**, *72*, 17.16.1.

[334] M. J. Hollamby, *Phys. Chem. Chem. Phys.* **2013**, *15*, 10566.

[335] E. Zhao, Z.-G. Zhang, X. Li, L. He, X. Yu, H. Li, F. Wang, *Chin. Phys. B* **2020**, *29*, 018201.

[336] D. Liu, Z. Shadike, R. Lin, K. Qian, H. Li, S. Wang, Q. Yu, M. Liu, S. Ganapathy, X. Qin, Q.-H. Yang, M. Wagemaker, F. Kang, X.-Q. Yang, B. Li, *Adv. Mater.* **2019**, *31*, 1806620.

[337] M. V. Avdeev, I. A. Bobrikov, V. I. Petrenko, *Phys. Sci. Rev.* **2018**, *3*, 20170157.

[338] C. F. Majkrzak, N. F. Berk, U. A. Perez-Salas, *Langmuir* **2003**, *19*, 7796.

[339] S. Mattauch, A. Koutsioubas, U. Räcker, D. Korolkov, V. Fracassi, J. Daemen, R. Schmitz, K. Bussmann, F. Suxdorf, M. Wagener, P. Kämmerling, H. Kleines, L. Fleischhauer-Fuß, M. Bednareck, V. Ossoviy, A. Nebel, P. Stronciwilk, S. Staringer, M. Gödel, A. Richter, H. Kusche, T. Kohnke, A. Ioffe, E. Babcock, Z. Salhi, T. Bruckel, *J. Appl. Crystallogr.* **2018**, *51*, 646.

[340] E. Hüger, L. Dörrer, J. Rahn, T. Panzner, J. Stahn, G. Lilienkamp, H. Schmidt, *Nano Lett.* **2013**, *13*, 1237.

[341] C. Braun, Parratt32 or the reflectometry tool, http://www.helmholtz-berlin.de (accessed: December 2012).

[342] J. F. Browning, L. Baggetto, K. L. Jungjohann, Y. Wang, W. E. Tenhaeff, J. K. Keum, D. L. Wood, G. M. Veith, *ACS Appl. Mater. Interfaces* **2014**, *6*, 18569.

[343] R. G. Downing, G. P. Lamaze, J. K. Langland, S. T. Hwang, *J. Res. Natl. Inst. Stand. Tecnol.* **1993**, *98*, 109.

[344] E. Vezhlev, A. Ioffe, S. Mattauch, V. Ossovyi, Ch. Felder, E. Hüger, J. Vacik, I. Tomandl, V. Hnatowicz, C. Chen, P. H. L. Notten, Th. Brückel, *Radiat. Eff. Defects Solids* **2020**, *175*, 342.

[345] D. L. Danilov, C. Chen, M. Jiang, R.-A. Eichel, P. H. L. Notten, *Radiat. Eff. Defects Solids* **2020**, *175*, 367.

[346] H. Bethe, *Ann. Phys.* **1930**, *5*, 325.

[347] H. Bethe, *Z. Phys.* **1932**, *76*, 293.

[348] F. Bloch, *Ann. Phys.* **1933**, *16*, 285.

[349] F. Bloch, *Z. Phys.* **1933**, *81*, 363.

[350] J. F. M. Oudenhoven, F. Labohm, M. Mulder, R. A. H. Niessen, F. M. Mulder, P. H. L. Notten, *Adv. Mater.* **2011**, *23*, 4103.

[351] J. Auvergniot, A. Cassel, J.-B. Ledeuil, V. Viallet, V. Seznec, R. Dedryvère, *Chem. Mater.* **2017**, *29*, 3883.

[352] C. Wang, Y. Gong, Y. Dai, L. Zhang, H. Xie, G. Pastel, B. Liu, E. Wachsman, H. Wang, L. Hu, *J. Am. Chem. Soc.* **2017**, *139*, 14257.

[353] I. Tomandl, J. Vacik, T. Kobayashi, Y. M. Sierra, V. Hnatowicz, V. Lavreniev, P. Horak, G. Ceccio, A. Cannavo, M. Baba, R. Ye, *Radiat. Eff. Defects Solids* **2020**, *175*, 394.

Chunguang Chen received his Ph.D. in Electrical Engineering from Eindhoven University of Technology in 2019. Starting from 2017, he joined Fundamental Electrochemistry (IEK-9), Forschungszentrum Jülich (Germany) as a guest researcher. He is currently serving as a scientific assistant researcher at IEK-9, being involved in various national and international collaborations. His research has been focused on development of advanced thin-film microbatteries, interfacial tailoring of all-solid-state batteries, operando analyses, as well as mechanics of both bulk and thin-film electrode materials.

Yujie Wei is a professor at the Institute of Mechanics, Chinese Academy of Sciences (CAS). He also serves as the director of the State Key Laboratory of Nonlinear Mechanics and holds a joint professorship at the University of CAS. His major research interests are exploring the relationship between macroscopic mechanical properties and microscale structures of advanced materials, and advanced computational techniques and data-driven structural healthy analysis. Prior to joining CAS, he was an assistant professor at University of Alabama. He received his B.S. degree from Peking University in 1997 and his Ph.D. degree from Massachusetts Institute of Technology in 2016.

Peter H. L. Notten joined Philips Research Laboratories (Eindhoven, The Netherlands) from 1975 to 2010. He received his Ph.D. degree from Eindhoven University in1989. Since then he focused on energy storage research, including hydrogen and lithium storage materials, new battery technologies, modeling electrochemical systems, and design of battery-management algorithms. In 2000, he was appointed as professor at TU/e where he heads the group Energy Materials and Devices. In 2014 he has was appointed as International Adjunct Faculty at Amrita University, Coimbatore (India), as group leader at Forschungszentrum Jülich (Germany), and in 2018 as honorary professor at University of Technology Sydney.